



Raytheon

LAND SURFACE TEMPERATURE

VISIBLE/INFRARED IMAGER/RADIOMETER SUITE

ALGORITHM THEORETICAL BASIS DOCUMENT

Version 3: May 2000

Donglian Sun
Yimin Ji
Philip E. Ardanuy
Peter S. Kealy
Wenli Yang

*William Emery, Science Team Member
University of Colorado*

RAYTHEON SYSTEMS COMPANY
Information Technology and Scientific Services
4400 Forbes Boulevard
Lanham, MD 20706

SBRS Document #: Y2399

NPOESS COMPETITION SENSITIVE

EDR: LAND SURFACE TEMPERATURE

Doc No: Y2399

Version: 3

Revision: 0

	Function	Name	Signature	Date
Prepared by	EDR Developer	D. SUN		
Approved by	Relevant IPT Lead	Y. JI		
Approved by	Chief Scientist	P. ARDANUY		
Released by	Program Manager	H. BLOOM		

TABLE OF CONTENTS

	<u>Page</u>
LIST OF FIGURES	iii
LIST OF TABLES.....	viii
GLOSSARY OF ACRONYMS	ix
ABSTRACT	xi
1.0 INTRODUCTION	1
1.1 PURPOSE	1
1.2 SCOPE.....	1
1.3 VIIRS DOCUMENTS	1
1.4 REVISIONS	1
2.0 EXPERIMENT OVERVIEW.....	3
2.1 OBJECTIVES OF LAND SURFACE TEMPERATURE RETRIEVALS	3
2.2 INSTRUMENT CHARACTERISTICS	3
2.3 LAND SURFACE TEMPERATURE RETRIEVAL STRATEGY	6
3.0 ALGORITHM DESCRIPTION	7
3.1 PROCESSING OUTLINE.....	7
3.2 ALGORITHM INPUT.....	8
3.2.1 VIIRS Data	8
3.2.2 Non-VIIRS Data	8
3.3 THEORETICAL DESCRIPTION OF LAND SURFACE TEMPERATURE RETRIEVAL	8
3.3.1 Physics of the Problem	8
3.3.2 Mathematical Description of the Algorithm	18
3.3.3 Data Set Description.....	27
3.3.4 Archived Algorithm Output	27
3.3.5 Variance and Uncertainty Estimate	27
3.3.6 Land cover approach	34
3.3.7 Water vapor's effect	54
3.3.8 Cloud contamination studies	68
3.3.9 Validation problem.....	73

3.4	ALGORITHM SENSITIVITY STUDIES	78
3.4.1	Calibration Errors.....	78
3.4.2	Instrument Noise	81
3.4.3	Band-to-Band Registration	83
3.4.4	Geolocation error or mapping uncertainty	84
3.4.5	MTF effect	85
3.4.6	Emissivity	86
3.4.7	Land Cover.....	86
3.5	PRACTICAL CONSIDERATIONS	87
3.5.1	Numerical Computation Consideration	87
3.5.2	Programming and Procedural Considerations.....	87
3.5.3	Configuration of Retrievals.....	87
3.5.4	Quality Assessment and Diagnostics	87
3.5.5	Exception Handling	88
3.6	ALGORITHM VALIDATION	88
3.6.1	Pre-Launch Validation	88
3.6.2	Post-Launch Validation.....	88
4.0	ASSUMPTIONS AND LIMITATIONS	89
5.0	REFERENCES.....	91

LIST OF FIGURES

	<u>Page</u>
Figure 1a. IR radiance at the satellite for five atmospheres simulated by MODTRAN. The dashed lines are calculated from the Planck function.	4
Figure 1b. Atmospheric transmittances for five atmospheres. The dashed lines are calculated from the Planck function.	4
Figure 2a. LST flowchart 1: One equation for all land surface types.	7
Figure 2b. LST flowchart 2: One equation for each land surface type.	8
Figure 3a. Water vapor vs. surface skin temperature distribution.	10
Figure 3b. Upper Panel: Transmittance vs. total column water vapor over land. Bottom Panel: Transmittance vs. LST.	11
Figure 3c. Temperature deficits ($T_s - T_b$) vs. total column water vapor distribution.	12
Figure 4. Variation in emissivity for different surface types.	13
Figure 5. (Upper panel) Relationship between temperature deficits of 10.8 μm and 12 μm bands for forest only. (Bottom panel) Relationship between temperature deficits of 10.8 μm and 12 μm bands for all 23 land types.	15
Figure 6. Channel emissivities for 23 land types.	17
Figure 7. IPO Tercat scene at 50m resolution.	29
Figure 8. Truth land surface temperature for IPO 50 m Tercat scene (upper panel); retrieved LST distribution by using generalized split window algorithm (bottom panel).	30
Figure 9. LST retrieval bias distribution by using generalized split window algorithm.	31
Figure 10. Precision vs. temperature distribution for IPO 50 m Tercat scene.	31
Figure 11. Upper panel: Global LST. Middle panel: Retrieved LST. Lower panel: The difference between the LST values.	36
Figure 12. LST retrieval error vs. temperature distribution with SNR 3 for VIIRS-new band algorithm with different combination, compared with generalized split window. The upper panel: generalized split window. The second: 11,12 and 3.75 μm . The third: 11, 12 and 4.005 μm . The bottom: 11, 12 and 8.55 μm	37

Figure 13	LST precision (upper panel), accuracy (middle) and uncertainty (bottom) distribution vs. satellite view angle and LST for 3-band algorithm (emissivity approach) without temperature category.....	38
Figure 14.	Same as figure 13, but with two temperature category (below 285 K) and above 285 K.	39
Figure 15	LST precision (upper panel), accuracy (middle) and uncertainty (bottom) distribution vs. satellite view angle and LST for 5-band algorithm (emissivity approach) with two-temperature category below 285 K and above 285 K.....	40
Figure 16	Nighttime LST precision (upper panel), accuracy (middle) and uncertainty (bottom) distribution vs. satellite view angle and LST for 4-band algorithm (emissivity approach) with two temperature category below 285 K and above 285 K.....	41
Figure 17	Daytime LST precision (upper panel), accuracy (middle) and uncertainty (bottom) distribution vs. satellite view angle and LST for 4-band algorithm (emissivity approach) with solar zenith correction with two temperature category below 285 K and above 285 K.	42
Figure 18.	LST retrieval error vs. temperature distribution with SNR 3 some split window algorithms. The upper panel: generalized split window. The second: Becker and LI' 1997 split window algorithm with water vapor correction. The third: Coll and Caselles's (1997) split window algorithm with water vapor correction.	43
Figure 19.	LST precision (upper panel), accuracy (middle) and uncertainty (bottom) distribution vs. satellite view angle and LST for Becker and Li's(1995) split window algorithm (emissivity approach with water vapor correction) with two-temperature category below 285 K and above 285 K.....	44
Figure 20.	LST precision (upper panel), accuracy (middle) and uncertainty (bottom) distribution vs. satellite view angle and LST for Coll and Caselles's (1997) split window algorithm (emissivity approach with water vapor correction) with two-temperature category below 285 K and above 285 K.....	45
Figure 21.	Global land cover distribution in July 1993.....	46
Figure 22a.	Precision analysis for the two different retrieval methods.....	47
Figure 22b.	Global LST retrieval precision from the two retrieval methods.	47
Figure 23.	LST retrieval error distribution with sensor noise model 3 for different approaches. The upper panel is for generalized split window, the second panel is for VIIRS-split window, the third is for VIIRS-4 band without solar	

	zenith correction, the bottom panel is for VIIRS-5 bands algorithm (LC approach).....	48
Figure 24.	LST retrieval precision vs. temperature distribution for generalized split window, VIIRS-new algorithm and VIIRS-5 bands algorithm.	49
Figure 25.	LST retrieval error vs. LST distribution for VIIRS-4 bands algorithm. The upper panel: Without solar zenith angle correction. The bottom panel: With solar zenith angle correction during the daytime.....	50
Figure 26.	Comparison of LST precision distribution over LST for VIIRS-4 band algorithm (LC approach) during nighttime, and daytime with and without solar zenith correction.	51
Figure 27.	Nighttime LST precision (upper panel), accuracy (middle) and uncertainty (bottom) distribution over satellite view angle and LST by using VIIRS-4 band algorithm (LC approach)	52
Figure 28.	Daytime LST precision (upper panel), accuracy (middle) and uncertainty (bottom) distribution over satellite view angle and LST by using VIIRS-4 band algorithm (LC approach) with solar zenith correction.....	53
Figure 29.	Total column water vapor distribution over land in our global dataset.....	54
Figure 30.	The LST precision, accuracy and uncertainty distribution with the TCWV and view angle by using the generalized split window algorithm.....	58
Figure 31.	The LST precision, accuracy and uncertainty distribution with the TCWV and view angle by using Becker and Li's (1995) split window algorithm (with water vapor correction).	59
Figure 32.	The LST precision, accuracy and uncertainty distribution with the TCWV and view angle by using Coll and Caselles's (1997) split window algorithm (with water vapor correction).	60
Figure 33.	The LST precision, accuracy and uncertainty distribution with the TCWV and view angle by using the 3-band algorithm (emissivity approach).	61
Figure 34.	The LST precision, accuracy and uncertainty distribution with the TCWV and view angle by using the 5-band algorithm (emissivity approach).	62
Figure 35.	The LST precision, accuracy and uncertainty distribution with the TCWV and view angle by using the VIIRS 4-band algorithm (Land cover approach).	63
Figure 36.	Comparison of different algorithms with IPO 2415 profiles over land under clear condition with the published coefficients or global training coefficients.....	64

Figure 37.	LST retrieval to the IPO 2415 profiles over land under clear condition with self-training coefficients. Precision for different algorithms (Upper panel). Accuracy for different algorithms (lower panel).....	65
Figure 38.	The upper panel is the truth LST of IPO Olympic scene. The middle panel is the retrieved LST with sensor noise model 3, MTF model 4 and calibration error 2% by using VIIRS new algorithm. The bottom panel is the bias of the retrieved LST to its truth-value.	66
Figure 39.	Upper panel: LST retrieval precision vs. the truth LST for different algorithms. Bottom panel: LST retrieval accuracy vs. temperature distribution.	67
Figure 40.	a) Bangladesh truth LST; b) the retrieved LST; c) the bias distribution between the retrieved LST and the truth LST.	69
Figure 41.	Retrieved LST precision vs. temperature for different sensor noise models.	70
Figure 42.	(a) Retrieved LST precision vs. sensor noise model and calibration error without removing clouds. (b) Same as (a), but clouds was partly removed.	71
Figure 43.	Physical retrieval to the IPO 2450 profiles under cloudy condition. (a) Retrieved LST vs. truth LST scatter plot. (b) Bias vs. truth LST scatter plot.....	72
Figure 44.	Global land covers at 8-km resolution during July 1992.	75
Figure 45.	Global LST retrieval at 8-km resolution during July 1992.	76
Figure 46.	Difference between skin LST and surface air temperature from the model simulation. Upper panel: During daytime period. Lower panel: During nighttime period.	77
Figure 47.	Scatter plot of LST values. The time difference between the satellite pass and the ground measurement is less than one hour.....	78
Figure 48.	Split window LST accuracy relevant to calibration error.	79
Figure 49a.	LST precision vs. Calibration error for different algorithms.	80
Figure 49b.	LST accuracy vs. calibration error for different algorithms.	80
Figure 50.	LST precision at eight categories from split window. The temperature interval is 5K.....	81
Figure 51.	LST accuracy vs. Sensor Noise Model from split window.....	82
Figure 52.	LST precision from VIIRS-4 band (3.75, 4.005, 10.8, and 12 μm) day/night algorithm.	82

Figure 53.	The influence of band-to-band registration on LST retrieval precision.	83
Figure 54.	LST precision vs. band-to-band registration error for IPO 50m Olympic land scene with no sensor noise, no calibration error and no MTF effect aggregated to 1km and compared with the ground truth LST by using split window algorithm.....	84
Figure 55.	LST precision vs. geolocation error	84
Figure 56.	LST retrieval precision vs. GSD for MTF model 4 and 7.....	85
Figure 57.	LST precisions vs. skin LST with 0.005 emissivity error.	86
Figure 58.	LST precision vs. temperature by using VIIRS –4 bands day/night algorithm with 20% land cover classification error.	87

LIST OF TABLES

	<u>Page</u>
Table 1. Channel Characteristics of Satellite-borne Infrared Radiometers	5
Table 2. Recommended Bands and Their NEDT Values.....	5
Table 3. NEDT Values in Five IR Bands for Seven Sensor Noise Models	6
Table 4. Band-Averaged Emissivities of 23 Surface Types in VIIRS Bands 10, 11, 12, SST1, SST2, SST4.....	16
Table 5. Parameter n_i for Approximate Planck Function (Power Function) for Five VIIRS Bands	23
Table 6. Atmospheric Transmittance for Standard Atmosphere Profiles	25

GLOSSARY OF ACRONYMS

ATBD	Algorithm Theoretical Basis Document
ATSR	Along Track Scanning Radiometer
AVHRR	Advanced Very High Resolution Radiometer
ECMWF	European Center for Medium-Range Weather Forecast
EDR	Environmental Data Record
FOV	Field of View
IFOV	Instantaneous Field of View
IPO	Integrated Program Office
IR	Infrared
LST	Land Surface Temperature
MODIS	Moderate Resolution Imaging Spectroradiometer
MODTRAN	Moderate Resolution Atmospheric Radiance and Transmittance Model
MOSART	Moderate Spectral Atmosphere Radiance and Transmittance
NCEP	National Centers for Environment Prediction
NDVI	Normalized Difference Vegetation Index
NEDT	Noise Equivalent Temperature Difference
NPOESS	National Polar-orbiting Operational Environmental Satellite System
RSS	Root Sum Square
SBRS	Santa Barbara Remote Sensing
SST	Sea Surface Temperature
SWIR	Shortwave Infrared
TAR	Top of Atmosphere Radiance
TIR	Thermal Infrared
TOA	Top of Atmosphere
TPW	Total Precipitable Water
VIIRS	Visible/Infrared Imager/Radiometer Suite

ABSTRACT

This is the Algorithm Theoretical Basis Document (ATBD) for the National Polar-orbiting Operational Environmental Satellite System (NPOESS) Visible/Infrared Imager/ Radiometer Suite (VIIRS) Land Surface Temperature (LST) algorithm. LST is a VIIRS level 2 product and also an input variable for other VIIRS products such as soil moisture, land type classification, and infrared (IR)-band emissivity.

The atmospheric correction, the complexity of land surface types, and the sensor performance limit the accuracy of satellite LST measurements. The current satellite multi-channel LST algorithm can permit global LST retrievals on spatial scales of 8 km with 3 to 4 K measurement accuracy. The VIIRS LST Environmental Data Record (EDR) requires a global horizontal cell size of 4 km with 2.5 K measurement accuracy and 0.5 K measurement precision.

The VIIRS LST algorithms are based on physically based regression methods to retrieve skin LST. They will use radiances sensed by VIIRS visible and IR channels. Two algorithms are being developed using a global database (established by the NPOESS algorithm team) and a radiative transfer model. In the first algorithm, radiances from visible and near-IR channels will be used to determine land cover type and the Normalized Difference Vegetation Index (NDVI). Emissivities for all IR bands for a certain land cover type will be calculated according to the land cover type classification and NDVI value. This will be done by use of a kernel model or a spectral library. The LST will be decided by emissivities and brightness temperatures derived from VIIRS IR 10.8, 12, and 8.55 μm bands. The second algorithm establishes one equation for each land cover type and uses 4 thermal band brightness temperatures. This algorithm does not need emissivity information and yields better precision. Both algorithms are described in this document. The second algorithm is currently considered the baseline algorithm. However, ongoing algorithm development will determine the best algorithm.

Our simulation showed that the accuracy of VIIRS LST retrievals in the worst case is 2.1 K. In the first algorithm, the precision is 0.84 K for the split window (10.8 and 12 μm bands) algorithm and 0.59 K for the triple window (10.8, 12, and 8.55 μm bands) algorithm, without considering the errors in emissivities. If 1% errors in the emissivity are added, the precision is 1.57 K for the split window algorithm and 1.4 K for the triple window algorithm. For the second algorithm, the precision is 0.45 K with perfect land type classification, and 0.52 K with 20 percent land type classification errors.

Pre-launch and post-launch activities are discussed in this document. The validation of LST is limited by the availability of *in situ* observations. The VIIRS LST is defined as the skin temperatures of the uppermost layer of the land surface, while *in situ* observations are usually shelter temperatures. Reliable observed or analyzed skin temperatures will be a critical factor in validating the VIIRS LST retrieval.

The VIIRS LST retrieval is performed under clear sky conditions only. This will limit both regional and global coverage. A weekly 1.3 km resolution global LST field will be a goal of the VIIRS LST retrieval.

1.0 INTRODUCTION

1.1 PURPOSE

This is the Algorithm Theoretical Basis Document (ATBD) for the National Polar-orbiting Operational Environmental Satellite System (NPOESS) Visible/Infrared Imager/ Radiometer Suite (VIIRS) Land Surface Temperature (LST) algorithm. This document identifies sources of input data, and describes the theoretical basis and development process of the LST algorithms.

1.2 SCOPE

LST is a VIIRS level 2 product and also an input variable for other VIIRS products, such as soil moisture. The LST algorithms described in this document will be used to routinely retrieve LSTs from VIIRS measurements. However, future development efforts may result in modifications to the current operational algorithms. Only algorithms that will be implemented in the operational process are described in this document.

The next section of this document provides an overview of the LST retrieval algorithm. A description of the algorithms and their development is presented in Section 3. Section 3 also addresses error budgets, algorithm sensitivity, and validation. Constraints, assumptions, and limitations are identified in Section 4, and Section 5 presents references cited in the document.

1.3 VIIRS DOCUMENTS

Reference to VIIRS documents will be indicated by a number in italicized brackets, e.g., [V-1].

[V-1] VIIRS Sensor Requirements Document, NPOESS IPO

[V-2] VIIRS Sea Surface Temperature ATBD, SBRS Doc. Y 2386

1.4 REVISIONS

This is the third version of this document, dated May 2000. The first version was dated October 1998. The second version was dated June 1999.

2.0 EXPERIMENT OVERVIEW

2.1 OBJECTIVES OF LAND SURFACE TEMPERATURE RETRIEVALS

Land surface temperatures play an important role in land-surface processes on a regional as well as on a global scale. They are of fundamental importance to the net radiation budget at the Earth's surface and to monitoring the state of crops. LST is a good indicator of both the greenhouse effect and the energy flux between the atmosphere and the ground (Mannstein, 1987; Sellers *et al.*, 1988). Satellite-derived LST can be assimilated to climate, mesoscale and land surface models to estimate the sensible heat flux and latent heat flux from the Earth's surface. Satellite-based LST measurement has not been used operationally in regional weather forecasting and climate prediction due to large uncertainties. Satellite-based measurements, however, have the potential to provide LST information over vast remote regions such as deserts, and make it possible to calculate global surface temperature changes.

The accuracy of satellite LST measurement is limited by the atmospheric correction, the complexity of land surface types, and sensor performances. The current satellite multichannel LST algorithm can permit global LST retrievals on spatial scales of 8 km with 3 to 4 K measurement accuracy. (Becker and Li, 1990; Dozier and Wan, 1994; Li and Becker, 1993).

The overall scientific objective of the VIIRS LST retrievals is to provide improved measurements of global and regional LST fields. The VIIRS LST Environmental Data Record (EDR) requires a global horizontal cell size of 4 km with 2.5 K measurement accuracy and 0.5 K measurement precision. These requirements exceed the current state-of-the-art results. The requirement of measurement precision is difficult to meet because of the large variations of LST in both space and time. LSTs can vary by 10 K in just a few meters and by 50 K over the daily cycle (Prata, 1993).

2.2 INSTRUMENT CHARACTERISTICS

The VIIRS sensor is being designed based on the NPOESS sensor requirements and EDR thresholds and objectives. Therefore, the following specifications of VIIRS are used only in the current version of retrieval algorithms and are subject to changes during the flowdown process.

VIIRS bands in the far-infrared (IR) region must be placed to optimize their use for LST determination. Bands in the far-IR are usually located near the maximum Earth radiance. The influence of ozone and other atmospheric absorbers must be avoided. Figure 1a shows Moderate Resolution Atmospheric Radiance and Transmittance Model (MODTRAN) simulated radiances at satellite altitude for thermal infrared spectra. There are a total of five standard atmospheres. There are two regions suitable for far-IR band selection: 8–9 μm and 10–13 μm . VIIRS far-IR bands will be located in the two spectrums. Figure 1b shows the MODTRAN simulated atmospheric transmittance for five standard atmospheres. It shows that the 8–9 μm and 10–13 μm regions are transparent to the atmosphere. The detail of the LST band selection can be found in Caselles *et al.*, 1997.

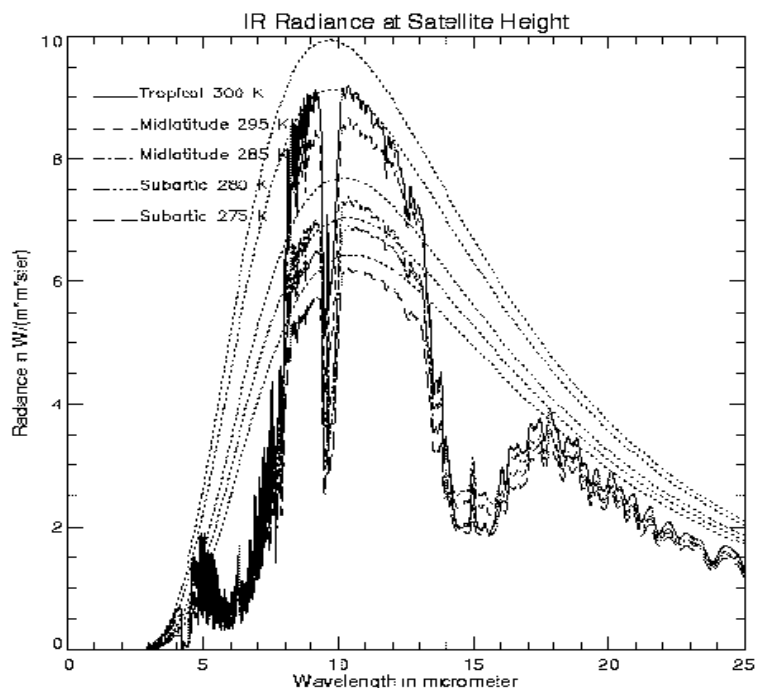


Figure 1a. IR radiance at the satellite for five atmospheres simulated by MODTRAN. The dashed lines are calculated from the Planck function.

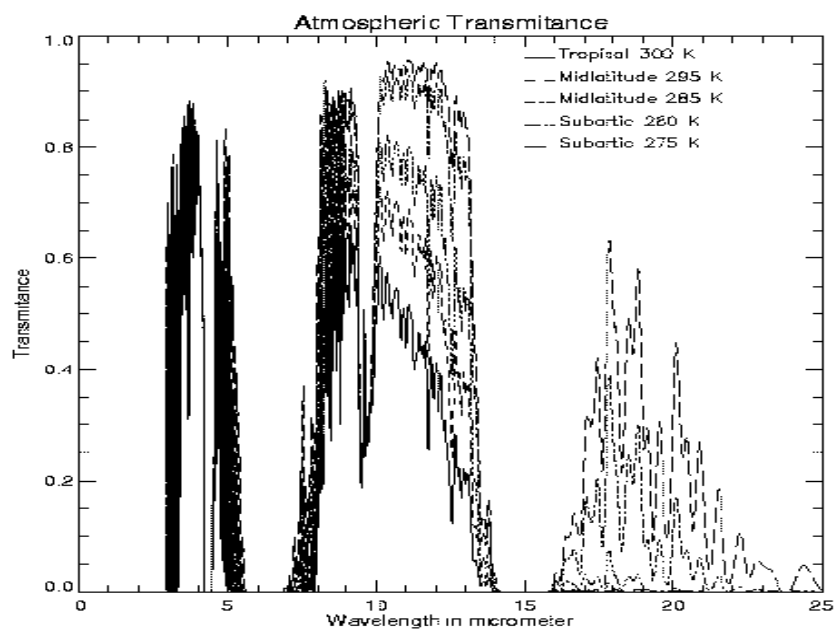


Figure 1b. Atmospheric transmittances for five atmospheres. The dashed lines are calculated from the Planck function.

Table 1 shows the bands in use or to be used by existing or proposed satellites to retrieve LST. The VIIRS band selection does not significantly differ from those of existing satellites.

Table 1. Channel Characteristics of Satellite-borne Infrared Radiometers

VIIRS baseline		MODIS		AVHRR		ATSR		OCTS		GLI	
λ μm	NEDT K	λ μm	NEDT K	λ μm	NEDT K	λ μm	NEDT K	λ μm	NEDT K	λ μm	NEDT K
3.75	0.18	3.75	0.05	3.75	0.1	3.7	0.019	3.7	0.15	3.715	< 0.15
4.0	0.15	3.96	0.07								
		4.02	0.07								
8.55	0.04	8.55	0.07					8.52	0.15	8.3	< 0.1
10.8	0.08	11.03	0.05	10.5	0.1	10.8	0.028	10.8	0.15	10.8	< 0.1
12	0.1	12.02	0.05	11.5	0.1	12	0.025	11.9	0.15	12	< 0.1

Three VIIRS bands will be used for LST retrieval. The specifications for the three bands are listed in Table 2.

Table 2. Recommended Bands and Their NEDT Values

λ (μm)	$\Delta\lambda$ (μm)	IFOV(km)		Detector Type	NEDT(K) (At 300 K)
		Nadir	EOS		
3.75	0.18	0.6	0.9	PV HgCdTe	0.18
4.0	0.154	0.6	0.9	PV HgCdTe	0.15
8.55	0.3	0.6	0.9	PV HgCdTe	0.10
10.8	1	0.6	0.9	PV HgCdTe	0.08
12*	1	0.3	0.45	PV HgCdTe	0.10

*Band $\lambda = 12 \mu\text{m}$ may be at a higher spatial resolution to support other EDR's, but it will be designed to "nest" into the larger pixels.

Table 3 shows the NEDT values for seven testing sensor noise models in the three bands. The base model is model 3.

Table 3. NEDT Values in Five IR Bands for Seven Sensor Noise Models

λ (μm)	$\Delta\lambda$ (μm)	NEDT(K at 300 K)/Apparent Aperture Diameter (cm)						
		Model 1 29 cm	Model 2 24 cm	Model 3 19 cm	Model 4 14 cm	Model 5 9 cm	Model 6 4 cm	Model 7 1 cm
3.75	0.18	0.12	0.14	0.18	0.26	0.47	1.71	18.31
4.005	0.154	0.10	0.12	0.15	0.22	0.38	1.31	14.50
8.55	0.3	0.03	0.03	0.04	0.07	0.15	0.7	10.39
10.8	1	0.04	0.06	0.08	0.13	0.30	1.43	20.88
12	1	0.05	0.07	0.10	0.17	0.38	1.85	26.92

There are a total of 16 suggested bands for VIIRS. These bands will be used to retrieve the cloud mask, land surface type classifications, and NDVI values, which are critical to the LST retrieval accuracy.

2.3 LAND SURFACE TEMPERATURE RETRIEVAL STRATEGY

Before LST retrievals can be performed within a given region, various atmospheric and surface parameters need to be determined. Here, a region is defined to be a target area of 32 by 32 pixels, covering only land. A cloud cover mask and a snow/ice mask will be used to eliminate cloud-contaminated or ice-covered pixels. The algorithms are run only under clear sky conditions. The following sequence of LST retrieval activity is performed on all suitable pixels within a region. First, the brightness temperatures are calculated for five mid-IR and far-IR bands from Top of Atmosphere (TOA) radiances. Land cover type and NDVI will be retrieved from visible and near-IR bands. Emissivities of thermal IR bands will be determined using a spectral library. The LST will be calculated using a regression equation. Pixels will then be aggregated to 1 km resolution. In the second algorithm, only land type will be needed. Either VIIRS Land type or ancillary land type data will be used to determine a pixel's type. An equation will then be determined to calculate LST. The first algorithm is a follow-up of Moderate Resolution Imaging Spectroradiometer (MODIS) algorithm (Wan and Dozier, 1996). The second algorithm is new and will need to be validated in the future.

3.0 ALGORITHM DESCRIPTION

3.1 PROCESSING OUTLINE

The VIIRS LST retrieval is initially assisted by an establishment of an ancillary data set. The coefficients of regression equations will be obtained using MODTRAN and a global database through our simulation processes. Figure 2a and Figure 2b depict the processing concept for LST retrievals. There are currently two methods. In the first algorithm, only one equation is established for the global data (Figure 2a). In the second algorithm, one equation is developed for each land type. There are a total of 21 equations for the global data (Figure 4).

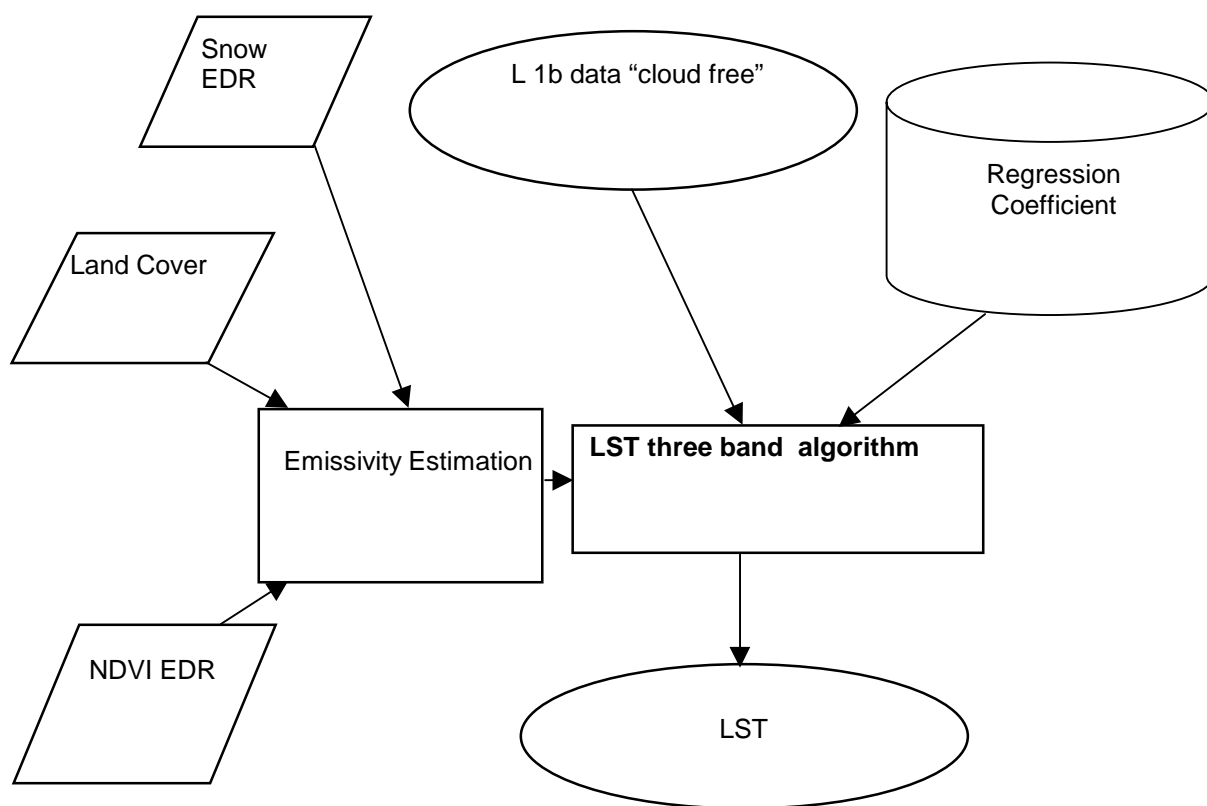


Figure 2a. LST flowchart 1: One equation for all land surface types.

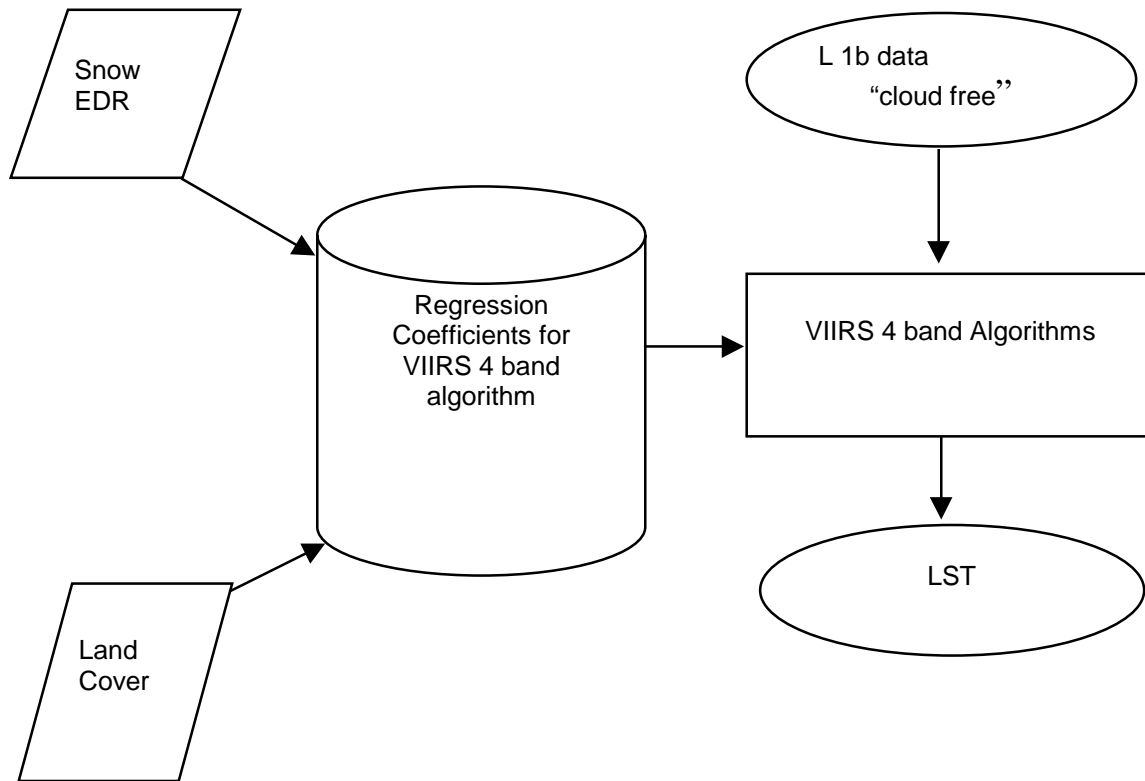


Figure 2b. LST flowchart 2: One equation for each land surface type.

3.2 ALGORITHM INPUT

3.2.1 VIIRS Data

VIIRS inputs required for the LST algorithm include cloud mask, land surface classification, and IR radiance.

3.2.2 Non-VIIRS Data

The LST algorithm requires a spectral library. Already available global land surface classification data with 1 km resolution will also be used. A land/ocean mask is needed to determine land pixels.

3.3 THEORETICAL DESCRIPTION OF LAND SURFACE TEMPERATURE RETRIEVAL

3.3.1 Physics of the Problem

In clear sky conditions, the outgoing infrared spectral radiance at the top of atmosphere can be represented by:

$$\begin{aligned}
 L(\lambda, \mu) = & \tau(\lambda, \mu) \epsilon(\lambda, \mu) B(\lambda, T_s) + L_a(\lambda, \mu) + L_s(\lambda, \mu, \mu_0, \phi_0) \\
 & + L_d(\lambda, \mu, \mu_0, \phi_0) + L_r(\lambda, \mu, \mu_0, \phi_0)
 \end{aligned} \tag{1}$$

Where τ is the transmissivity, ϵ the surface spectral emissivity, B the Plank function, L_a the thermal path radiance, L_s the path radiance resulting from scattering of solar radiation. L_d is the solar radiance and L_r the solar diffuse radiation and atmospheric thermal radiation reflected by the surface. λ is the wavelength. $\mu = \cos(\theta)$, $\mu_o = \cos(\psi)$, where θ is the satellite zenith angle, ψ the solar zenith angle. ϕ_o is the azimuth angle.

The wavelength is the wavelength center of a narrow interval because there is no way to measure the exact monochromatic signal as a continuous function of wavelength by satellite sensors. Equation 1 can be used in the 3–14 μm range. It requires complete calculations of the atmospheric radiative transfer to determine the values of all terms on the right side. This equation has been used in many atmospheric radiation models including LOWTRAN (Kneizys *et al.*, 1988), MODTRAN (Berk *et al.*, 1987), and Moderate Spectral Atmospheric Radiance and Transmittance (MOSART) (Cornette *et al.*, 1994).

For far-IR bands, L_d , L_s , and L_r are negligible. Therefore, only the first two terms on the right side of the above equation are important. The first term represents the surface contribution term, and it is the gray-body radiance emitted by the earth's surface. The second term is the atmospheric contribution term, and is the vertically integrated effect of emission from every atmospheric layer modulated by the transmittance of the air above that emitting layer.

$$L(\lambda, \mu) = \epsilon_0(\lambda, \mu) B(\lambda, T_s) \tau_0(\lambda, \mu) + \int_{\tau_0}^1 B(\lambda, T_p) d\tau(\lambda, \mu, \rho) \quad (2)$$

Where τ_0 is the transmittance at the Earth's surface.

In order to infer the surface information, we should choose window channel with no or less atmospheric contribution. As shown in Figure 1a, the wavelength between 3.5–4.2 micron, 8–9 micron, and 10–13 micron are some typical atmospheric windows, with less atmospheric absorption. For a perfect window, the total atmospheric transmittance $\tau_0(\lambda, \mu)$ should be 1.0, the transmittance weighting function should be 0. But as we see from Figure 1b, the transmittances at these windows are not 1.0, this is mainly the result of the water vapor absorption.

In order to see the water vapor's contribution at the atmospheric window channel, we did some simulations to the 2415 profiles offered by the IPO (Integrated Program Office) over land surfaces under clear sky conditions by using MODTRAN 3.7. The following five window bands are simulated: 3.75 μm , 10.8 μm (AVHRR channel 4), 12 μm (AVHRR channel 5), and two new VIIRS bands, including 4.005 μm and 8.55 μm .

As we can see from the transmittance vs. surface skin temperature distribution, shown as Figure 3a, at warmer temperature (285–310 K), for 10.8 and 12 μm channel, even 8.55 μm channel, the transmittances decrease significantly. Most values are below 0.8. This is why most existing split window algorithms using the 11 and 12 μm channels get larger errors in the temperature range 285–310 K. The transmittance for the Shortwave Infrared (SWIR) channel 3.75 μm and 4.005 μm is more stable, with less change to the surface skin temperature; most values are above 0.8. From this aspect, SWIR 3.75 μm and 4.005 μm channels are better window channels than the IR 11, 12, and 8.55 micron channels. The most stable channel is at 4.005 microns. From the

transmittance vs. precipitable water distribution (Figure 3b), we can also see that the transmittance at the 4.005 micron channel is the most stable. It changes very little with the column water vapor amount. While the transmittance at 3.75 micron channel has a linear relationship with the precipitable water, the transmittances at 11, 12, and 8.55 microns decrease significantly as the water vapor increases and the relationship is also not linear. We need to use the information from SWIR window channel when we retrieve warmer surface temperatures.

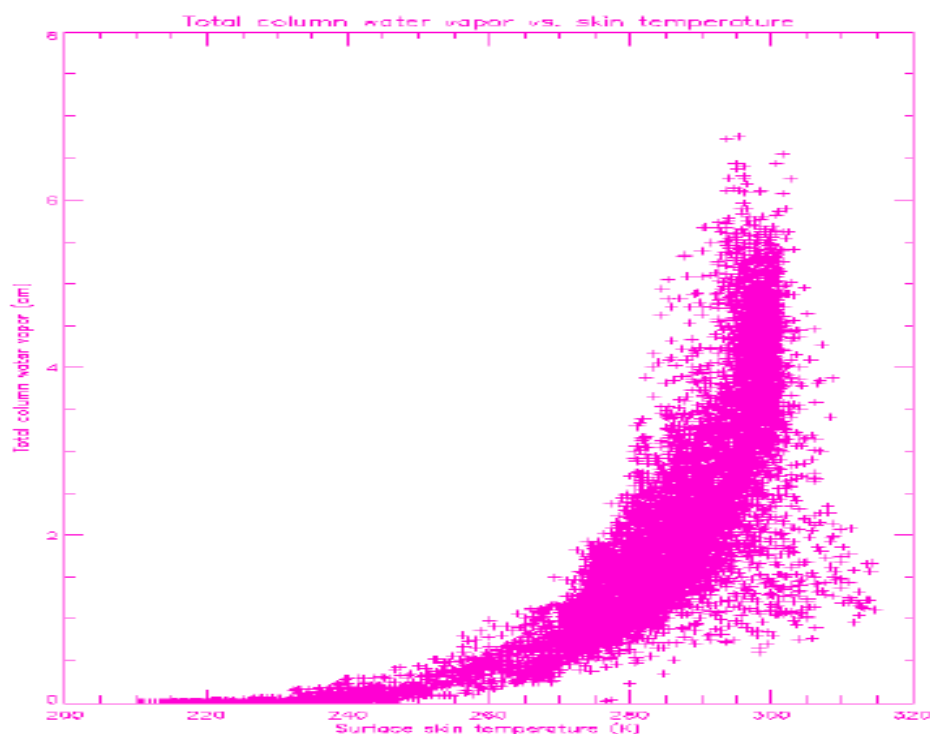
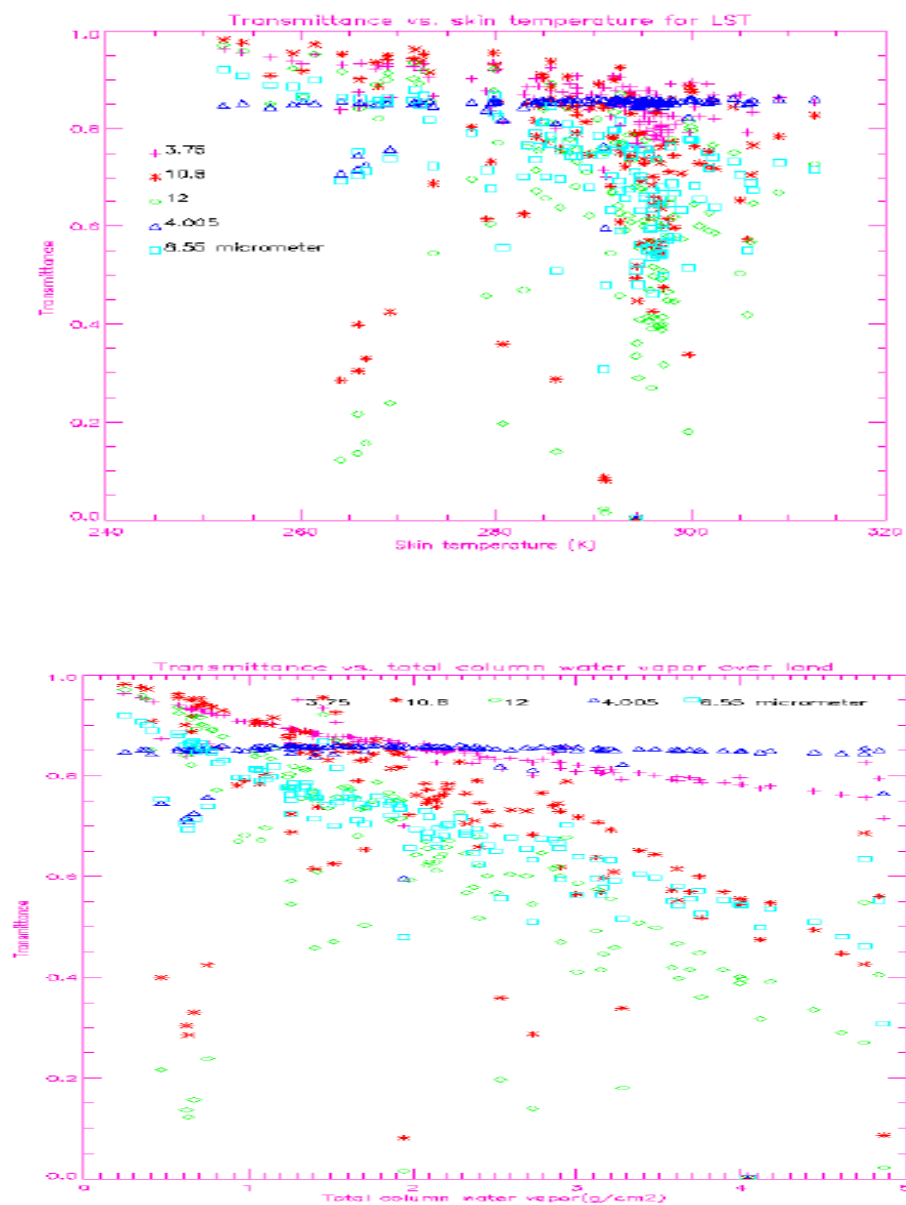


Figure 3a. Water vapor vs. surface skin temperature distribution.



**Figure 3b. Upper Panel: Transmittance vs. total column water vapor over land.
Bottom Panel: Transmittance vs. LST.**

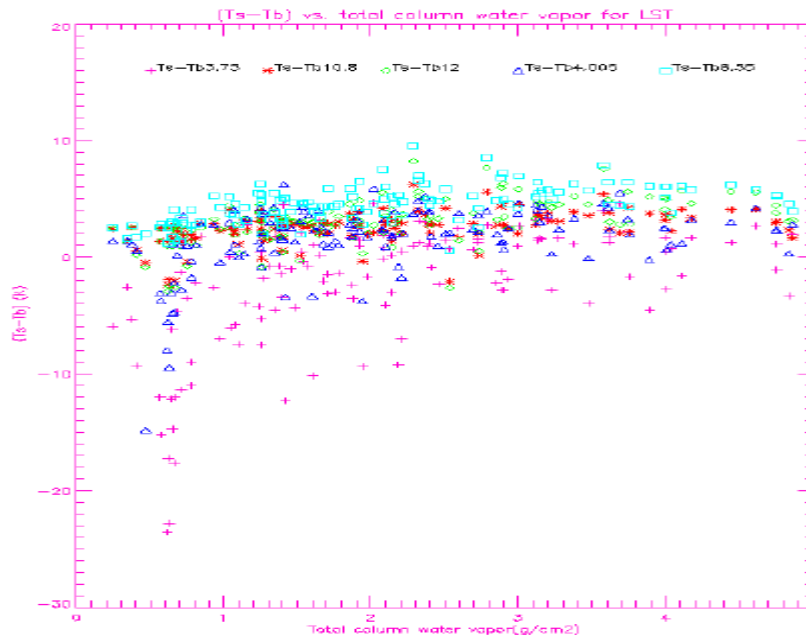


Figure 3c. Temperature deficits ($T_s - T_b$) vs. total column water vapor distribution.

But from the difference between the surface temperature and brightness temperature vs. precipitable water distribution, as shown in Figure 3c, the temperature deficit ($T_s - T_b$) at IR window channels 11, 12, and 8.55 microns is very stable, while the surface temperature at SWIR channels 3.75 and 4.005 microns can be much lower than the brightness temperature, sometimes by more than 10 degrees. This is because in the daytime, the SWIR channel contains both reflected solar radiation and radiation emitted by the surface and the atmosphere, this is the so-called solar glint. So the best way to retrieve surface temperature is to appropriately combine IR and SWIR window channels.

Currently, most existing LST algorithms are based on Becker and Li's split window technique (1990).

$$T_s = (A1 + A2 \frac{1 - \epsilon}{\epsilon} + A3 \frac{\Delta \epsilon}{\epsilon^2}) \frac{T_{11} + T_{12}}{2} + (B1 + B2 \frac{1 - \epsilon}{\epsilon^2} + B3 \frac{\Delta \epsilon}{\epsilon^2}) (T_{11} - T_{12}) + C \quad (3)$$

Where $\epsilon = (\epsilon_{11} + \epsilon_{12})/2$ and $\Delta \epsilon = \epsilon_{11} - \epsilon_{12}$. ϵ_{11} and ϵ_{12} are the emissivities at 10.8 μm and 12 μm bands respectively. T_{11} and T_{12} are the brightness temperatures at 10.8 μm and 12 μm bands respectively.

One of the major difficulties in the development of the LST algorithm is the considerable spectral variation in emissivities for different land surface types. Observation of emissivity spectra shows that in general, emissivity spectra with high values exhibit little variation, while those with lower values exhibit a greater variation, such as Grass, as shown in Figure 4.

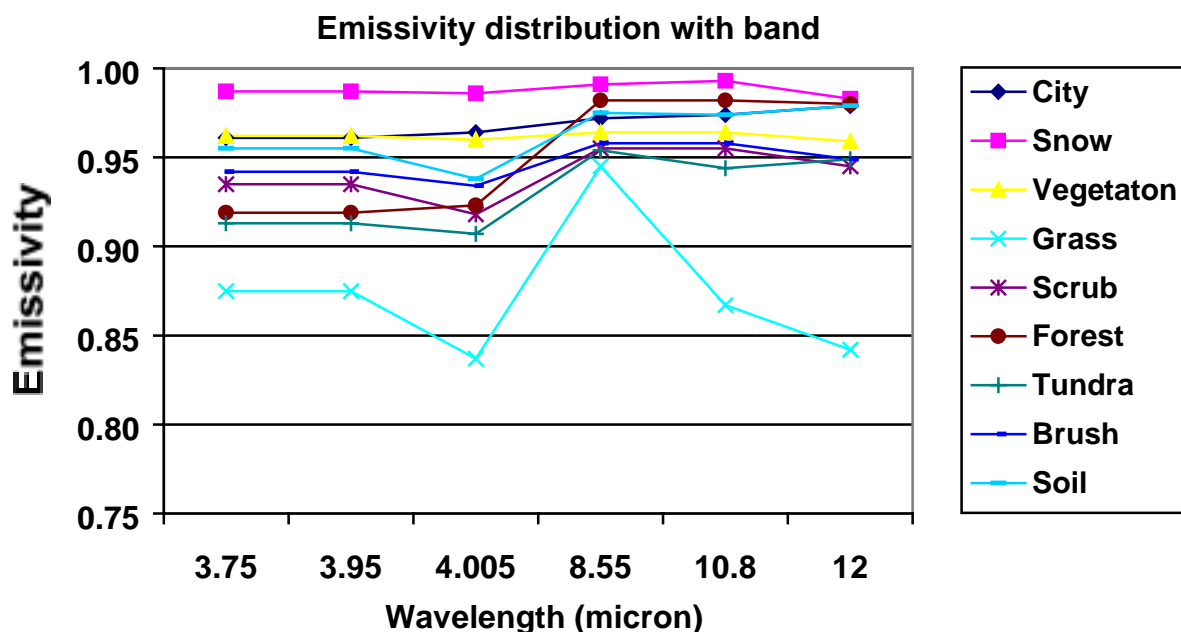


Figure 4. Variation in emissivity for different surface types.

If we ignore the change of emissivity for a certain land surface type, the radiance error introduced by the atmosphere ΔL can be represented by:

$$\begin{aligned}
 \Delta L &= B(\lambda, T_s) - L(\lambda, \mu) = B(\lambda, T_s) - \tau(\lambda, \mu)B(\lambda, T_s) - L_a(\lambda, \mu) \\
 &= - \int_1^{\tau(\lambda, \mu)} B(\lambda, T_s) d\tau(\lambda, \mu, p) + \int_1^{\tau(\lambda, \mu)} B(\lambda, T_p) d\tau(\lambda, \mu, p) \\
 &= - \int_1^{\tau(\lambda, \mu)} (B(\lambda, T_s) - B(\lambda, T_p)) d\tau(\lambda, \mu, p)
 \end{aligned} \tag{4}$$

From the Planck function we find:

$$\Delta L = \frac{\partial B}{\partial T} \Delta T = \frac{\partial B}{\partial T} (T_s - T_\lambda) \tag{5}$$

For an optically thin gas the following approximations can be made:

$$d\tau = d\{\exp(-k_\lambda L)\} = -k_\lambda dl \tag{6}$$

where k_λ is the absorption coefficient and l is the optical path-length. If we assume that the Planck function is adequately represented by a first order Taylor series expansion in each channel window, then:

$$B(\lambda, T_s) - B(\lambda, T_p) = \left. \frac{\partial B(\lambda, T_p)}{\partial T} \right|_{T_s} (T_p - T_s) \quad (7)$$

Substituting Equations 5, 6, 7 into Equation 4, we obtain:

$$T_s - T_\lambda = k_\lambda \int_1^\tau (T_s - T_p) dl \quad (8)$$

Therefore, if we select two spectral regions of the atmosphere, we will have two linear equations with different k_λ to solve simultaneously.

For example if we consider the two channels as $\lambda=1$ and $\lambda=2$, then we get:

$$T_s - T_1 = -(T_2 - T_1)k_1 / (k_2 - k_1) \quad (9)$$

This equation is similar to the Sea Surface Temperature (SST) equation, but can only be used for one land type, assuming the band emissivity does not vary within this land type. Figure 5a shows the relationship between band temperature deficits $T_s - T_{11}$ and $T_s - T_{12}$ for forests. The data are global data with 17,885 skin temperatures and atmospheric profiles. The relationship is rather linear, which confirms that for a particular land type, the linear split window algorithm used in SST retrieval can be adopted for LST retrieval (we call this the land surface separated method). Figure 5b is similar to Figure 5a, but for simulations of 23 land cover types. There is much more variation in this figure; the relationship is not linear. Emissivities, therefore, have to be considered as an important factor for Becker and Li's 1990 LST algorithm.

For land surfaces, the emissivity for each channel changes with surface type. Table 4 shows the band-averaged emissivities for 23 surface types derived from MOSART spectra. Although this table contains a majority of the NPOESS land surface types, the full spectral library for NPOESS land surface types is under development. The differences between 10.8 μm and 12 μm bands are small for most of the types, thus making the VIIRS land surface separated algorithm feasible.

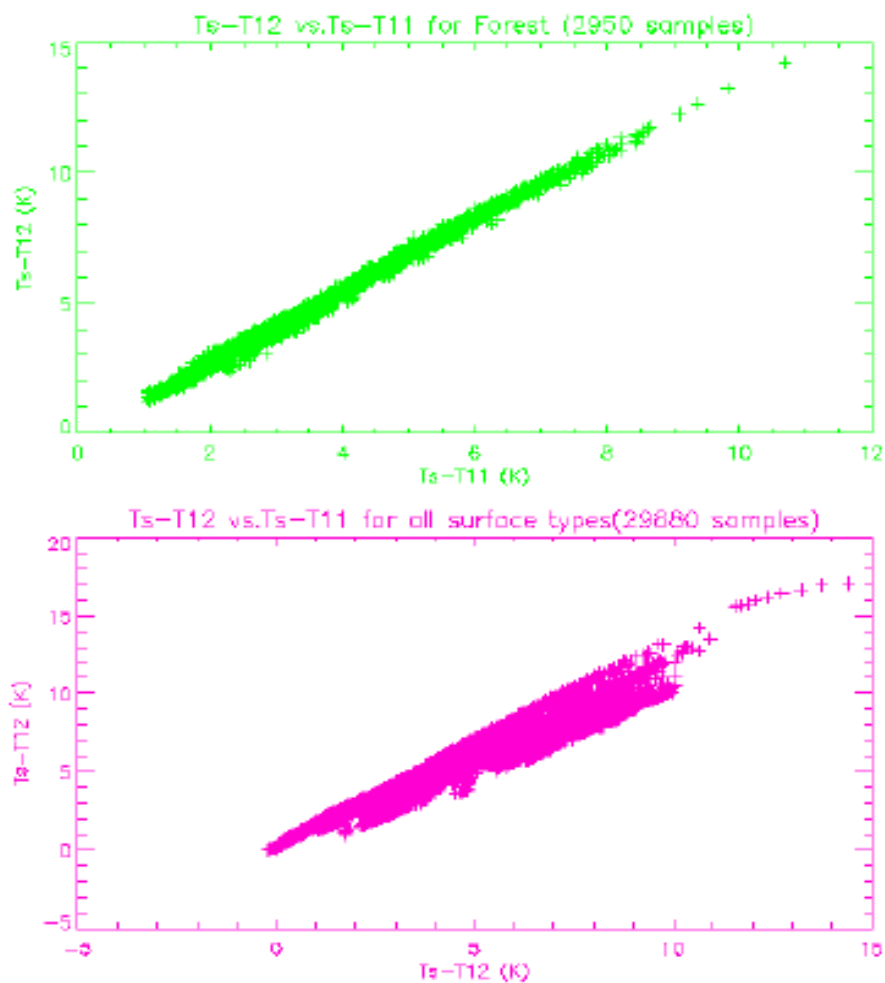


Figure 5. (Upper panel) Relationship between temperature deficits of 10.8 μm and 12 μm bands for forest only. (Bottom panel) Relationship between temperature deficits of 10.8 μm and 12 μm bands for all 23 land types.

**Table 4. Band-Averaged Emissivities of 23 Surface Types in VIIRS
Bands 10, 11, 12, SST1, SST2, SST4.**

Surface Type Index	Type of Materials	£ _{3.75}	£ _{10.8}	£ ₁₂	£ _{3.99}	£ _{4.00}	£ _{8.55}
1	Water	0.980	0.990	0.990	0.980	0.980	0.985
2	Old snow	0.987	0.993	0.983	0.987	0.986	0.991
3	Sea ice	0.987	0.995	0.983	0.987	0.982	0.992
4	Compacted soil	0.930	0.957	0.967	0.930	0.895	0.965
5	Tilled soil	0.951	0.970	0.977	0.951	0.926	0.975
6	Sand	0.500	0.950	0.980	0.500	0.550	0.900
7	Rock	0.800	0.915	0.960	0.800	0.840	0.895
8	Cropland	0.962	0.964	0.959	0.962	0.960	0.964
9	Meadow grass	0.875	0.867	0.842	0.875	0.837	0.945
10	Scrub	0.935	0.955	0.945	0.935	0.918	0.955
11	Broadleaf forest	0.952	0.962	0.956	0.952	0.957	0.962
12	Pine forest	0.905	0.990	0.990	0.905	0.907	0.990
13	Tundra	0.913	0.944	0.949	0.913	0.907	0.954
14	Grass-soil	0.908	0.921	0.918	0.908	0.872	0.957
15	Broadleaf-pine forest	0.919	0.982	0.980	0.919	0.923	0.982
16	Grass-scrub	0.905	0.911	0.893	0.905	0.877	0.950
17	Soil-grass-scrub	0.915	0.929	0.923	0.915	0.885	0.956
18	City	0.961	0.974	0.979	0.961	0.964	0.972
19	Pine-brush	0.920	0.973	0.967	0.920	0.913	0.973
20	Broadleaf-brush	0.942	0.958	0.949	0.942	0.934	0.958
21	Wet soil	0.955	0.974	0.979	0.955	0.938	0.975
22	Scrub-soil	0.932	0.956	0.959	0.932	0.904	0.961
23	Broadleaf (70%)—Pine (30%)	0.938	0.970	0.966	0.938	0.942	0.970

Figure 6 shows the emissivity change as a function of surface types for five VIIRS mid-IR and far-IR bands. Far-IR band emissivities are relatively stable for all land types. The changes of mid-IR emissivity are larger at land type 6 (sand) and type 7 (rock).

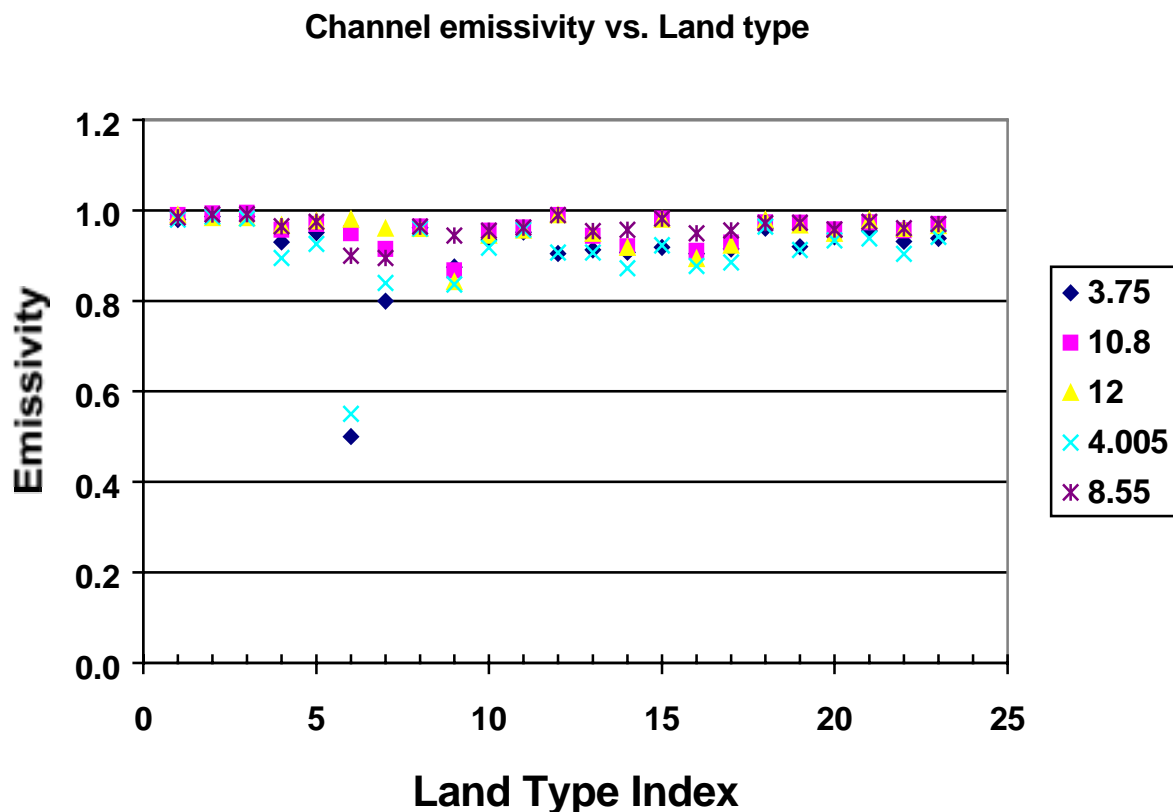


Figure 6. Channel emissivities for 23 land types.

In general, Equation 7 can be written as:

$$T_s = CT_b \quad (10)$$

The coefficient vector C , relating observed brightness temperatures to LST, is determined using a regression method by solving:

$$C = YX^T(XX^T)^{-1} \quad (11)$$

The Y matrix contains a large number of training LSTs and the X matrix contains brightness temperatures from VIIRS far-IR and mid-IR channels. In general, the X matrix may include non-linear terms.

Currently, the LST uncertainty from the regression algorithm is about 1 ~ 3 K.

3.3.2 Mathematical Description of the Algorithm

To solve Equation 1 physically is not easy, even if we only consider the first two terms on the right side. In order to calculate L_a , we must know the atmospheric profile for each pixel (unlikely to be available in the near future), and also the surface emissivity for each band. Because the surface emissivity for each band is different, the number of unknowns is always larger than the number of equations discussed above. A number of ways have been suggested to physically retrieve the surface temperature and emissivity. These methods include the two temperature method (Watson, 1992), the temperature emissivity separation method (Kealy and Hook, 1993), and the day/night method (Wan and Dozier, 1996). However, these methods demand many more far-IR bands than in the VIIRS baseline design. Like the physical retrieval approach we are going to discuss here, 230 CrIS channels are used to retrieve atmospheric profile information combining with 7 window channels to retrieve surface properties (LST, surface emissivities, and reflectance). In our improved statistical regression method (land surface separated method), the VIIRS land cover product will be an input for LST retrieval. The following equations are currently used in VIIRS LST algorithms.

(1) Regression method (Emissivity approach)

Generalized Split Window:

Split Window (10.8, 12 μm bands) Algorithm (Wan and Dozier (1996), based on Becker and Li's 1990 algorithm):

$$T_s = a_0 + (a_1 + a_2\varepsilon_1 + a_3\varepsilon_2)T_1 + (a_4 + a_5\varepsilon_1 + a_6\varepsilon_2)T_2 \quad (12)$$

Where $\varepsilon_1 = \frac{1 - (\varepsilon_{11} + \varepsilon_{12})/2}{(\varepsilon_{11} + \varepsilon_{12})/2}$, $\varepsilon_2 = \frac{\varepsilon_{11} - \varepsilon_{12}}{((\varepsilon_{11} + \varepsilon_{12})/2)^2}$, and ε_{11} and ε_{12} are emissivities corresponding to 10.8 and 12.0 μm bands, respectively.

$T_1 = (T_{11} + T_{12})/2$ and $T_2 = T_{11} - T_{12}$ where T_{11} and T_{12} are brightness temperature at 10.8 and 12.0 μm bands, respectively.

New 3-bands (10.8, 12, 8.55 μm bands) Algorithm (if possible, see (4) for detail derivation)

$$T_s = a_0 + a_1 \frac{(1 - \varepsilon_{10.8})}{\varepsilon_{10.8}} T_{10.8} + a_2 \frac{(1 - \varepsilon_{12})}{\varepsilon_{12}} T_{12} + a_3 \frac{(1 - \varepsilon_{8.55})}{\varepsilon_{8.55}} T_{8.55} + a_4 (\sec \theta - 1) \quad (13)$$

Five bands (10.8, 12, 8.55, 3.75, 4.005 μm bands) Algorithm:

$$T_s = a_0 + a_1 \frac{(1 - \varepsilon_{10.8})}{\varepsilon_{10.8}} T_{10.8} + a_2 \frac{(1 - \varepsilon_{12})}{\varepsilon_{12}} T_{12} + a_3 \frac{(1 - \varepsilon_{8.55})}{\varepsilon_{8.55}} T_{8.55} + a_4 (\sec \theta - 1) + a_5 T_{3.75} + a_6 T_{4.005} \quad (14)$$

Where $\varepsilon_{8.55}$ and $T_{8.55}$ are the emissivity and brightness temperature at the suggested 8.55 μm band.

(2) Improved regression method (Land Cover approach)

As discussed above, for a specific surface type, the linear split window algorithm used in SST retrieval can be adopted for LST retrieval.

For each of the VIIRS 21 surface types, establish one equation by using 11 and 12 micron split window, this is our VIIRS split window algorithm.

$$LST_i = a_0(i) + a_1(i) T_{11} + a_2(i) (T_{11} - T_{12}) + a_3(i) (\sec \theta - 1) + a_4(i) (T_{11} - T_{12})^2 \quad i = 1, 21 \quad (15)$$

VIIRS-4 band day/night LST algorithm is our baseline algorithm, and establishes one equation to each surface type by using 4 VIIRS bands (10.8, 12, 3.75, and 4.005 μm), and it added a solar zenith angle correction during the daytime:

Daytime:

$$LST_i = a_0(i) + a_1(i) T_{11} + a_2(i) (T_{11} - T_{12}) + a_3(i) (\sec \theta - 1) + a_4(i) T_{3.75} + a_5(i) T_{4.0} + a_6(i) T_{3.75} \cos \varphi + a_7(i) T_{4.0} \cos \varphi + a_8(i) (T_{11} - T_{12})^2 \quad i = 1, 21 \quad (16)$$

Nighttime or day and night:

$$LST_i = b_0(i) + b_1(i) T_{11} + b_2(i) (T_{11} - T_{12}) + b_3(i) (\sec \theta - 1) + b_4(i) T_{3.75} + b_5(i) T_{4.0} + b_6(i) T_{3.75}^2 + b_7(i) T_{4.0}^2 + b_8(i) (T_{11} - T_{12})^2 \quad i = 1, 21 \quad (17)$$

Where i is the index of 21 VIIRS surface types.

Without the solar zenith angle correction, Equation 17 is used for both day and nighttime.

The VIIRS-5 band LST algorithm is used to establish one equation to each surface type by using 5 VIIRS bands (10.8, 12, 3.75, 4.005 and 8.55 μm), and includes the potential 8.55 μm band brightness temperature term. The equation is similar to the VIIRS-4 band equation during nighttime, but the term $T_{8.55}$ is added.

(3) Physical Retrieval Approach

(a) Linearize the Radiative Transfer Equation (RTE)

Linearize the radiative transfer equation with the nonlinearized terms being handled by physical kernel functions or Jacobians. Solve the linearized radiative transfer equations with the nonlinearities being handled through an optimized numerical iteration procedure (Marquardt-Levenberg Iteration) to get the surface skin temperature, atmospheric profiles (Temperature, Water vapor, Ozone) and surface emissivities and cloud properties. In order to retrieve surface properties, we need to select some window channels. In our work, we select 7 channels which are atmospheric windows or more surface-sensitive, and we assume the channel indexes are:

$$k_1, k_2, \dots, k_7.$$

For the single Field of View (FOV), the linearized RTE for the channel j is:

$$\begin{aligned} \delta TB = & K_{T_s} \delta T_s + \int_0^{P_s} K_T \delta T dp + \int_0^{P_s} K_q \delta \ln q dp + K_{\varepsilon_1}^* \delta \varepsilon_1 + K_{\varepsilon_2}^* \delta \varepsilon_2 + \dots + K_{\varepsilon_7}^* \delta \varepsilon_7 \\ & + K_{\rho_1}^* \delta \rho_1 + K^* \delta \rho + \dots + K_{\rho_7}^* \delta \rho_7 + K_N \delta N + K_{P_c} \delta P_c \end{aligned} \quad (18)$$

Where TB is the brightness temperature, T_s is the surface skin temperature, T is the temperature profile, q is the water vapor profile, $\varepsilon_1, \varepsilon_2, \dots, \varepsilon_7$ are the surface emissivities for 7 window channels, $\rho_1, \rho_2, \dots, \rho_7$ are the surface reflectance for the seven window channels. N is the cloud fraction, P_c is the cloud top pressure. K is the physical kernel function or Jacobians for the the corresponded term.

$$K_{\varepsilon_i} = \partial TB_{k_i} / \partial \varepsilon$$

$$K_{\rho_i}^* = \xi(k_i, j) K_{\rho_i}$$

$$K_{\varepsilon_i} = \xi(k_i, j) K_{\varepsilon_i}$$

$$\xi(k, j) = \begin{cases} 1 & k = j \\ 0 & k \neq j \end{cases}$$

$$k_i = 1, 2, \dots, 7$$

Equation (17) can be written in a more compact form as,

$$\delta y = K \delta x \quad (19)$$

Where $\delta y = \delta TB$. The Jacobian K is a matrix containing the Jacobians in (17)

$$K = [K_{T_s} \ K_T \ K_q \ K_{\varepsilon_1} \dots K_{\varepsilon_7} \ K_{\rho_1} \dots K_{\rho_7} \ K_N \ K_{P_c}]$$

And δx is a vector of the variables to be retrieved,

$$\delta x = [\delta T_s \ \delta T \ \delta \varepsilon_1 \dots \delta \varepsilon_7 \ \delta \rho_1 \dots \delta \rho_7 \ \delta N \ \delta P_c]^T$$

(b) Marquardt-Levenberg retrieval algorithm

This retrieval algorithm uses a hybrid nonlinear Newtonian iteration scheme, called the Marquardt-Levenberg method to find the maximum likelihood solution.

The Marquardt-Levenberg method is formulated as:

$$x_{n+1} = x_n - [\nabla^2 J(x_n) + \gamma I]^{-1} \nabla J(x_n) \quad (20)$$

Where γ is a parameter used to control the rate of convergence, $J(x)$ is the probability density function defined as,

$$J(x) = (x - x_b)^T S_b^{-1} (x - x_b) + (y - F(x))^T (y - F(x)) \quad (21)$$

Where x is the state vector, x_b is the initial state and S_b is its expected error covariance matrix. S is the expected covariance of the combined measurement and forward model error. Y is a vector of brightness temperature measurements, and $F(x)$ is the forward model.

Therefore, the maximum likelihood solution by using Marquardt-Levenberg iteration is given as:

$$X_{n+1} = X_b + (K_n^T S^{-1} K_n + S_b^{-1} + \gamma I)^{-1} [K_n^T S^{-1} ((y - F(X)) + K_n (X_n - X_b)) + \gamma I (X_n - X_b)] \quad (22)$$

(c) Convergence Criteria

Each iteration of Equation 22 required the application of a convergence test to determine whether the solution is or is not convergent. The γI matrix may then be adjusted based on the result of the convergence test. The convergence test applied to the Marquardt-Levenberg iteration determines the fit between the measurements and solution in terms of the “distance” between two consecutive solution sets:

$$d_{n+1} = (x_{n+1} - x_n)^T (K_n^T S^{-1} K_n + \gamma I)^{-1} (x_{n+1} - x_n) \quad (23)$$

with d_{n+1} being the “distance” between solutions x_{n+1} and x_n . If $d_{n+1} < d_n$, meaning the solution is converging, the γI elements are decreased and the state vector solution is updated. However, for the divergent solution, $d_{n+1} \geq d_n$, the γI elements are increased and the iteration is repeated with the “same state vector x ” that was used in the previous iteration.

(4) Physical retrieval combined with statistical retrieval

(New development, we can call this as VIIRS-3 band algorithm.)

Starting from the radiative transfer equation, the radiance measured by the channel i of a satellite sensor can be written as:

$$B_i(T_i) = \tau_i[\varepsilon_i B_i(T_s) + \rho_i R_i^\downarrow] + R_i^\uparrow \quad (24)$$

Where B_i is Plank function weighted for channel i , T_i is the rightness temperature measured at satellite level in the channel i , τ_i is the atmospheric transmittance for channel i , R_i^\downarrow is the hemispheric downward atmospheric radiance for the waveband of channel i , R_i^\uparrow is the upward radiance emitted by the atmosphere in the waveband of channel i , ρ_i is the channel bi-directional reflectivity of the surface. For simplicity, we assume Lambertian reflection, this is $\rho_i = (1 - \varepsilon_i)$.

Define brightness temperature at surface level T_i^* :

$$B_i(T_i^*) = \varepsilon_i B_i(T_s) + (1 - \varepsilon_i) R_i^\downarrow \quad (25)$$

Define mean radiative temperature of the atmosphere in the upward direction T_a^\uparrow , and downward direction T_a^\downarrow :

$$B_i(T_a^\uparrow) = \frac{R_i^\uparrow}{1 - \tau_i}, \quad B_i(T_a^\downarrow) = \frac{R_i^\downarrow}{1 - \tau_i}$$

Then inserting Equation 22 into Equation 21:

$$B_i(T_i) = \tau_i B_i(T_i^*) + (1 - \tau_i) B_i(T_a^\uparrow)$$

Linearize the Plank function around T_i :

$$\begin{aligned} \frac{\partial B}{\partial T} \Big|_{T_i} L(T_i) &= \tau_i \frac{\partial B}{\partial T} \Big|_{T_i} (T_i^* - T_i + L(T_i)) + (1 - \tau_i) \frac{\partial B}{\partial T} \Big|_{T_i} (T_a^\uparrow - T_i + L(T_i)) \\ L(T_i) &= B_i(T_i) / \frac{\partial B}{\partial T} \Big|_{T_i} \end{aligned}$$

The Planck function can be well approximated using a simple power function (Price, 1989):

$$B_i(T_i) = \alpha_i T_i^{n_i}$$

Parameters α_i and n_i are constants obtained by a least-square regression fitting. In order to have the best approximation of the Planck function, we divide the temperature range into two parts, less than 285 K, and warmer than 285 K. The parameter n_i is compiled in Table 5 in each case.

**Table 5. Parameter n_i for Approximate Planck Function
(Power Function) for Five VIIRS Bands**

Channel (μm)	n_i ($T_i < 285$ K)	n_i ($T_i > 285$ K)
3.75	13.87795	12.89512
10.8	4.99027	4.57420
12	4.51020	4.15224
4.005	13.32985	12.19271
8.55	6.27005	5.76009

The power law approximation is very useful for analyses involving the Planck function, with this approximation.

$$L(T_i) = \frac{T_i}{n_i}$$

So the atmospheric correction for brightness temperature can be written as:

$$T_i^* = T_i + \frac{1 - \tau_i}{\tau_i} (T_i - T_a^\uparrow) = \frac{1}{\tau_i} T_i - \frac{1 - \tau_i}{\tau_i} T_a^\uparrow \quad (26)$$

T_i^* depends only on the spectral because of its spectral dependence of surface emissivity. We linearize Planck function in (3.2) around T_i^* obtaining the emissivity correction, this is:

$$T_s = T_i^* + \frac{(1 - \epsilon_i)}{\epsilon_i} \left[\frac{T_i^*}{n_i} + \frac{(n_i - 1)}{n_i} (1 - \tau_i) T_i^* - (1 - \tau_i) T_a^\downarrow \right] \quad (27)$$

Inserting Equation 23 into Equation 24, we get:

$$T_s = C_{1i} T_i - C_{2i} T_a^\uparrow - C_{3i} T_a^\downarrow$$

Where:

$$C_{1i} = \frac{1}{\tau_i} \left[1 + \frac{(1 - \epsilon_i)}{n_i \epsilon_i} + \frac{(1 - \epsilon_i)(1 - \tau_i)(n_i - 1)}{n_i \epsilon_i} \right]$$

$$C_{2i} = \frac{(1-\tau_i)}{\tau_i} \left[1 + \frac{(1-\varepsilon_i)}{n_i \varepsilon_i} + \frac{(1-\varepsilon_i)(1-\tau_i)(n_i-1)}{n_i \varepsilon_i} \right] \quad (28)$$

$$C_{3i} = \frac{(1-\varepsilon_i)}{\varepsilon_i} (1-\tau_i)$$

Suppose surface emissivity and the atmospheric transmittance are known, and n_i is a constant that depends on the spectral channel. So now we have the three unknown parameters T_s , T_a^\uparrow and T_a^\downarrow , and we can only use the information of three channels to resolve the equation to obtain the surface temperature. In order to take advantage of all the information we can get, we can choose to use 3 bands to solve the equations, assume the channel indexes are: k_1, k_2, k_3

$$\begin{aligned} Ts &= C_{1k_1} T_{k_1} - C_{2k_1} T_a^\uparrow - C_{3k_1} T_a^\downarrow \\ Ts &= C_{1k_2} T_{k_2} - C_{2k_2} T_a^\uparrow - C_{3k_2} T_a^\downarrow \\ Ts &= C_{1k_3} T_{k_3} - C_{2k_3} T_a^\uparrow - C_{3k_3} T_a^\downarrow \\ T_a^\uparrow &= \frac{(C_{3k_3} - C_{3k_2})(C_{1k_3} T_{k_3} - C_{1k_2} T_{k_2}) - (C_{3k_2} - C_{3k_1})(C_{1k_2} T_{k_2} - C_{1k_1} T_{k_1})}{(C_{2k_3} - C_{2k_2})(C_{3k_3} - C_{3k_2}) - (C_{3k_2} - C_{3k_1})(C_{2k_2} - C_{2k_1})} \\ T_a^\downarrow &= \frac{(C_{1k_1} T_{k_1} - C_{1k_2} T_{k_2})}{(C_{3k_1} - C_{3k_2})} - \frac{(C_{2k_1} - C_{2k_2})}{(C_{3k_1} - C_{3k_2})} T_a^\uparrow \\ Ts &= C_{1k_1} T_{k_1} - C_{2k_1} T_a^\uparrow - C_{3k_1} T_a^\downarrow \end{aligned} \quad (29)$$

If we know the surface emissivity and the atmospheric transmittance for three channels, we can calculate the surface temperature T_s according to Equation 22, so this algorithm is actually a physical retrieval approach. In our IPO data set, we did simulations of all 2415 profiles under clear conditions over land surface. We have calculated the atmospheric transmittance for each profile and can use this new physical algorithm.

In MODTRAN's standard atmosphere profiles, we can also calculate their atmospheric transmittance, as shown in Table 6.

Table 6. Atmospheric Transmittance for Standard Atmosphere Profiles

Atmosphere	Precipitable water(g/cm-2)	$\tau_{10.8}$	τ_{12}
U.S. standard	1.13	0.8552	0.8014
Tropical	3.32	0.5574	0.4159
Midlatitude summer	2.36	0.6915	0.5786
Midlatitude winter	0.69	0.8993	0.8646
Subarctic summer	1.65	0.7847	0.7011
Subarctic winter	0.33	0.9336	0.9147

In the event that the atmospheric transmittance not available, we can use these typical atmosphere's transmittance, and then combined with the regression method to find the appropriate coefficients for each term in the above Equation 27:

$$C_{ji} = a_0(j) + a_1(j) \frac{(1 - \epsilon_i)}{\epsilon_i}, \quad j = k_1, k_3$$

Ts can then be written as:

$$Ts = a_0 + a_1 T_{k_1} + a_2 T_{k_2} + a_3 T_{k_3} + a_4 \frac{(1 - \epsilon_{k_1})}{\epsilon_{k_1}} T_{k_1} + a_5 \frac{(1 - \epsilon_{k_2})}{\epsilon_{k_2}} T_{k_2} + a_6 \frac{(1 - \epsilon_{k_3})}{\epsilon_{k_3}} T_{k_3} \quad (30)$$

If we add limb dark (view zenith angle) correction, then:

$$Ts = a_0 + a_1 T_{k_1} + a_2 T_{k_2} + a_3 T_{k_3} + a_4 \frac{(1 - \epsilon_{k_1})}{\epsilon_{k_1}} T_{k_1} + a_5 \frac{(1 - \epsilon_{k_2})}{\epsilon_{k_2}} T_{k_2} + a_6 \frac{(1 - \epsilon_{k_3})}{\epsilon_{k_3}} T_{k_3} + a_7 (\sec \theta - 1) \quad (31)$$

(5) Comparison with other algorithms

There are many published LST algorithms available, some of them were chosen for study here:

Price's (1984) algorithm:

$$T_{price} = [a_0 + a_1(T_4 - T_5)] \left(\frac{5.5 - \varepsilon_4}{4.5} \right) + a_3 T_4 \Delta \varepsilon$$

$$\Delta \varepsilon = \varepsilon_4 - \varepsilon_5$$
(32)

Vidal's (1991) algorithm:

$$T_{vidal} = a_0 + a_1(T_4 - T_5) + a_2 \frac{(1 - \varepsilon)}{\varepsilon} + a_3 \frac{\Delta \varepsilon}{\varepsilon}$$

$$\varepsilon = \frac{\varepsilon_4 + \varepsilon_5}{2}$$

$$\Delta \varepsilon = \varepsilon_4 - \varepsilon_5.$$
(33)

Prata's (1993) algorithm:

$$T_{pra} = \frac{a_0}{\delta} T_4 - \frac{2.42}{\delta} T_5 + d$$

$$\delta = \varepsilon_4 + 2.42 \tau_5 \Delta \varepsilon$$

$$d = \left[\frac{1 - \delta}{\delta} \right] \left[(B(T_4) - 6) \left(\frac{\partial B_4}{\partial T} \right)^{-1}_{T_4} - T_4 \right]$$
(34)

Becker and Li's (1995) algorithm:

$$T_{BL} = A_0 + PT^+ + MT^-$$

$$T^+ = \frac{T_4 + T_5}{2}$$

$$T^- = \frac{T_4 - T_5}{2}$$

$$A_0 = a_0 + a_1 W$$

$$P = a_2 + (a_3 + a_4 w \cos \theta)(1 - \varepsilon_4) - (a_5 + a_6 W) \Delta \varepsilon$$

$$M = a_7 + a_8 W + (a_9 + a_{10} W)(1 - \varepsilon_4) + (a_{11} + a_{12} W) \Delta \varepsilon$$
(35)

Coll and Caselles's (1997) algorithm:

$$\begin{aligned}
T_{CC} &= a_0 + a_1 T_4 + [(a_2 + a_3(T_4 - T_5))(T_4 - T_5) + \alpha(1 - \varepsilon_4) - \beta \Delta \varepsilon] \\
\varepsilon &= \frac{\varepsilon_4 + \varepsilon_5}{2} \\
\alpha &= (b_4 - b_5) \gamma \tau_5 + b_4 \\
\beta &= \gamma \tau_5 b_5 + \frac{\alpha}{2} \\
\gamma &= \frac{1 - \tau_4}{\tau_4 - \tau_5} \\
b_4 &= (c_0 + c_1 W) T_4 + (c_2 W + c_3) \\
b_5 &= (c_4 + c_5 W) T_5 + (c_6 W + c_7)
\end{aligned} \tag{36}$$

Subscripts 4 and 5 in equations 32 to 36 refer to 10.8 and 12 μm band, T is the brightness temperature, ε is the surface emissivity, τ is the transmittance. W in Equations 35 and 36 is the total precipitable water or total column water vapor.

As we can see in some algorithms, the satellite zenith angle at the Earth's surface, the solar zenith angle, and the column water are also included in the regression equation. In the nighttime, the emissivity and brightness temperature at the 3.75 μm band are also used to reduce the measurement uncertainty due to atmospheric correction.

3.3.3 Data Set Description

The data set we used to test our algorithms here including:

- IPO simulated scene;
- National Center for Environmental Prediction (NCEP) global snapshot surface temperature data set with matching atmospheric profiles at the resolution 2.5 x 2.5 degrees;
- 8344 profiles offered by IPO with matching surface skin temperature;
- NASA/NOAA pathfinder land data set with 8-km resolution.

3.3.4 Archived Algorithm Output

Brightness temperatures at a 1.3 km horizontal cell size are computed for all VIIRS mid-IR and far-IR bands for all satellite viewing angles. The best LST estimates are archived at 1.3 km resolution. The LST field will be aggregated to 4 km resolution globally.

3.3.5 Variance and Uncertainty Estimate

There are mainly three factors that contribute to the uncertainty of satellite LST retrieval: land surface classification and emissivity determination errors; atmospheric correction errors; and sensor performance. The atmospheric correction error and sensor performance have been discussed in the VIIRS LST ATBD [V-2]. The total precision is about 0.45 K. If the emissivities

are known exactly, the LST precision will be similar to SST precision. We have performed two experiments on a global data set. In one, the algorithm is applied for each surface type, assuming that the emissivity does not vary within each type. The precision errors in this case are indeed smaller than 0.5 K for almost all land surface types. In another, the algorithm is applied to all surface types with different emissivities. The precision is about 0.84 K for the split window and 0.59 K for the triple window.

One important data set we used to test LST algorithms is the IPO-simulated scene. IPO offered us land cover image at different locations and different resolutions. We then found the matched surface reflectance for the simulated bands from our spectral databases, and performed sensor and view geometry calculations, with appropriate surface truth. The MODTRAN 3.7 radiative transfer code was used to derive simulated top-of-the-atmosphere (TOA) radiance in different bands. The Santa Barbara Remote Sensing (SBRS) noise models, Modulation Transfer Function (MTF) model and calibration error were applied to the TOA radiances. We performed many tests on the different IPO scenes. Following is a discussion of these tests and their results.

Figure 7 shows the IPO Tercat scene at 50m resolution. The truth LST for this scene is shown as the upper panel of Figure 8. Most currently used algorithms are based on Becker and Li's 1990 algorithm. Figure 8 bottom panel is the retrieved LST distribution by using this split window algorithm. As we can see most of the retrieved land surface temperature are colder than the truth LST. From the retrieved precision distribution, shown as Figure 9, we can clearly see that most biases are negative. This is because the truth LST for this scene is warm temperature, most temperature values are above 296K. As we discussed before, split window algorithms by using 11 and 12 μm get bigger error at warmer temperature. Figure 10 shows the precision distribution vs. temperature, we can see split window algorithm can't meet the threshold requirement 0.5K for all temperature above 293 K. All the existing LST algorithms, although there are many different kinds of forms, are split window algorithms by using 11 and 12 micron bands. Like AVHRR channel 4 (11 μm band) and channel 5 (12 μm band) of NOAA series polar orbiting satellites, or similar bands on the Geostationary Meteorology satellites such as GOES and GMS (Japan). But as shown here, the split window algorithms can't give good retrieval at warmer temperature above 280 K. Therefore new algorithms need to be developed to overcome this problem. The NCEP global data set was used to test and train our new algorithms, we choose to use global data set because we expect it has good representative.

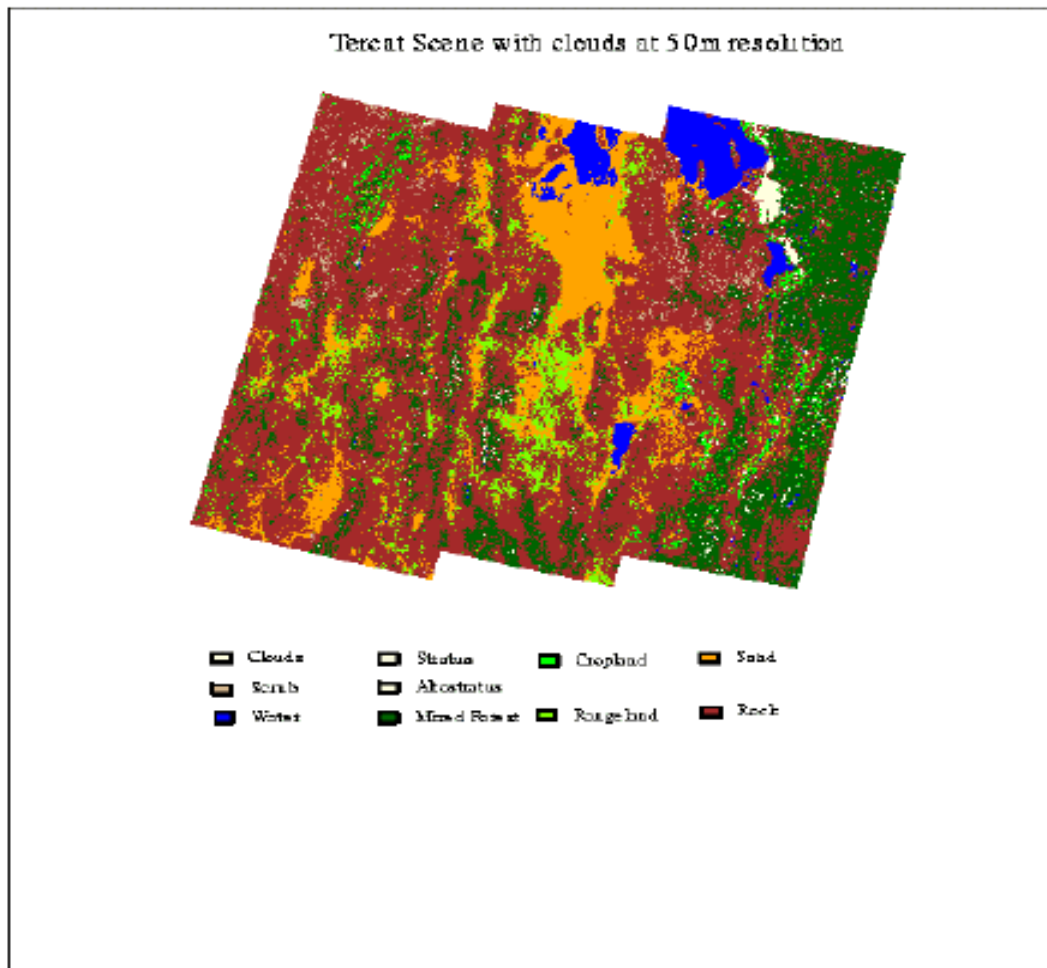


Figure 7. IPO Tercat scene at 50m resolution.

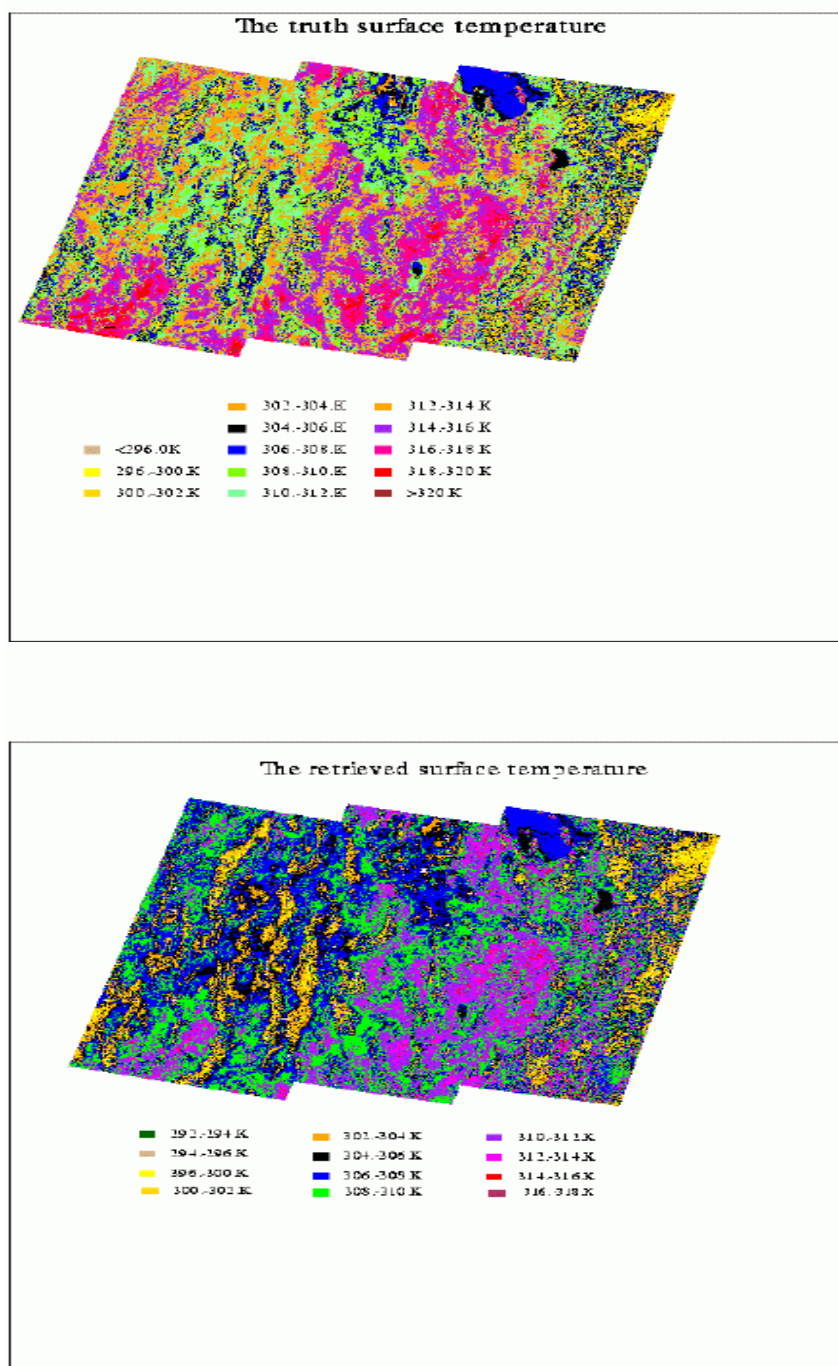


Figure 8. Truth land surface temperature for IPO 50 m Tercat scene (upper panel); retrieved LST distribution by using generalized split window algorithm (bottom panel).

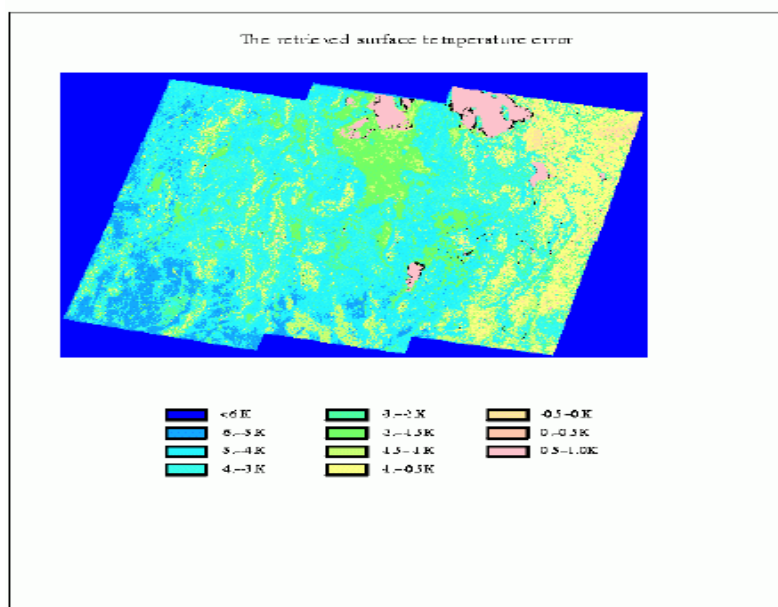


Figure 9. LST retrieval bias distribution by using generalized split window algorithm.

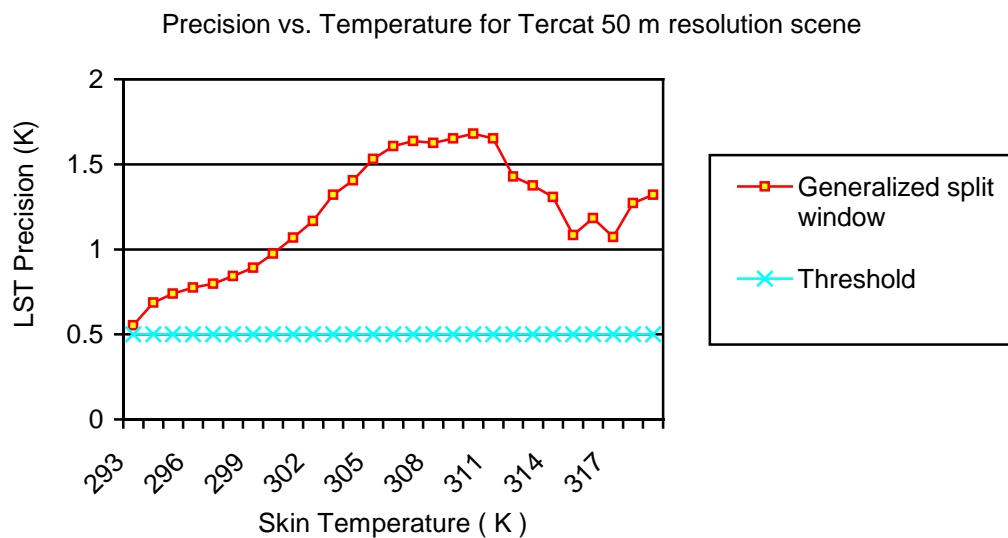


Figure 10. Precision vs. temperature distribution for IPO 50 m Tercat scene.

The global snapshot surface temperature data set is at 2.5° by 2.5° resolution supplied by the National Centers for Environment Prediction (NCEP), with matching atmospheric profiles. Another data set used is a surface temperature scene at 1-km resolution derived from Advanced Very High-Resolution Radiometer (AVHRR) 1b data. These data were used to simulate the top-of-atmospheric radiance (TAR) with MODTRAN. The Santa Barbara Remote Sensing (SBRS) sensor noise models were applied to the TOA radiance. Both noise-free TOA radiance and noisy TOA radiance were used to retrieve LST. The upper panel in Figure 11 shows the LST distribution for the global data set at 00 Z, July 1, 1993. The middle panel shows the retrieved LST with the generalized split window algorithm for the case of sensor noise model 3. The lower panel is the difference. The temperature range is from 210 to 315 K, the precision is 0.73 K and the maximum error is 3.58 K. The total precision for all temperature range still can't meet the threshold 0.5 K, so we need to develop new algorithms to meet the IPO requirement for 0.5 K precision. In the following section, we will compare and discuss different approach to retrieve LST and try to find the best way.

Emissivity approach

Figure 12 shows the LST retrieval error vs. temperature distribution with our new development VIIRS-3 bands algorithm with different combination compared with the generalized split window algorithm. The upper panel is for generalized split window algorithm. As we can see the generalized split window by using 11 and 12 μm bands got bigger error at warmer temperature between 280-310K. The second panel is VIIRS-3 bands algorithm with the combination of 11, 12 μm bands with 3.75 μm band. The third is for combination of 11, 12 μm with 4.005 μm band. The bottom panel is for combination of 11, 12 with 8.55 μm . VIIRS-three bands algorithm by combining 11 and 12 μm with 8.55 μm gives the best result. When 3.75 μm band was added to 11 and 12 μm , it obtained a little improvement to the split window algorithm by using 11 and 12 μm bands. Compared with 3.75 μm band, 4.005 μm band combined with 11 and 12 μm bands shows better result. However, 8.55 μm band combined with 11 and 12 μm gave the best result.

Although 3 bands algorithm by combining 11, 12 μm with the new IR-8.55 μm band gave the better result than the generalized split window, but it still show bigger error at warmer temperature between 295~305 K. At cold temperature below 225 K, it is even worse than the generalized split window. Figure 13 shows more clearly that the LST precision can't meet the threshold 0.5 K below 225 K and between 295 to 305 K. At warmer temperature range 295~305K, the precision increased with the satellite view angle, this is because with the satellite view angle increase, the optical path increase, atmospheric absorption increased. If we separate the whole temperature range into two categories below 285 K and above 285 K, the result is shown in Figure 14. Then, the precision at cold temperature below 285 K can meet the threshold 0.5 K, it is only about 0.25 K, the precision became much better at warmer temperature too, it is greater than 0.5 K only for view angle greater than 30 degree.

From figure 14, we can see even we separate temperature range into two categories, the precision at colder temperature range below 225 K can be improved to meet the threshold. But at warmer temperature between 295 to 305 K, the precision is still greater than 0.5 K for view angle greater than 30 degree. This is because the transmittance of 8.55 μm band also decreases rapidly at

warmer temperature range 295-305 K, as shown in figure 3 (b). When we derived our 3-band algorithm, we supposed the transmittance as constant coefficients, which will be found through regression method. In fact, the transmittance changed with band, atmospheric profile, and surface skin temperature. If we used the same regression coefficients, it certainly caused some error due to the uncertainty of the atmospheric transmittance. As shown in figure 3, the transmittance at the new SWIR 4.005 μm band almost doesn't change with the total column water vapor content. It has linear relationship with the water vapor content at the 3.75 μm , so if we add these two bands, it can be expected to overcome the atmospheric transmittance' effect. So we added two term the brightness temperature at the 4.005 μm band $T_{4.005}$ and $T_{3.75}$ at the 3.75 μm band to our 3-band equation, and formed a 5-band equation to calculate the LST. The result is shown in figure 15, the LST precision can meet the threshold 0.5 K at all temperature range and over all view angles.

The IPO requirement for LST accuracy and uncertainty is 2.5 K, our accuracy and uncertainty can meet the threshold in every case.

In case of the new IR 8.55 μm band may be removed due to its high expense. We must try to find a way without using the 8.55 μm band but it can still meet the 0.5 K precision threshold. In our new development derivation, three channel's information can resolve the equation, four bands' information can also resolve the problem, so we can get the following equation by using 11, 12, 3.75 and 4.005 μm bands:

$$Ts = a_0 + a_1 T_{11} + a_2 T_{12} + a_3 T_{3.75} + a_4 T_{4.005} + a_5 \frac{(1-\epsilon_{11})}{\epsilon_{11}} T_{11} + a_6 \frac{(1-\epsilon_{12})}{\epsilon_{12}} T_{12} + a_7 \frac{(1-\epsilon_{3.75})}{\epsilon_{3.75}} T_{3.75} + a_8 \frac{(1-\epsilon_{4.005})}{\epsilon_{4.005}} T_{4.005} + a_9 (\sec \theta - 1) \quad (37)$$

Due to solar contamination existed in the SWIR bands 3.75 and 4.005 μm band. So when we used these bands during daytime, we need to do solar zenith correction, so we have the following equation during daytime.

$$Ts = a_0 + a_1 T_{11} + a_2 T_{12} + a_3 T_{3.75} + a_4 T_{4.005} + a_5 \frac{(1-\epsilon_{11})}{\epsilon_{11}} T_{11} + a_6 \frac{(1-\epsilon_{12})}{\epsilon_{12}} T_{12} + a_7 \frac{(1-\epsilon_{3.75})}{\epsilon_{3.75}} T_{3.75} + a_8 \frac{(1-\epsilon_{4.005})}{\epsilon_{4.005}} T_{4.005} + a_9 (\sec \theta - 1) + a_{10} T_{3.75} \cos \phi + a_{11} T_{4.005} \cos \phi \quad (38)$$

During nighttime, equation (37) is used to calculate LST. The result was shown in figure 16, the precision can meet the threshold 0.5 K at most cases, except at 280-285 K and view angle greater than 40 degree. Equation (38) was employed to calculate LST during daytime, see figure 17, even with the solar zenith correction, the precision is greater than 0.5 K at warmer temperature above 290 K. This is because at some surface such as rock, sand, and desert, the surface skin temperature during daytime is very high, but the surface emissivity at the 3.75 and 4.005 μm band is only 0.5 and 0.55 over sand, 0.8 and 0.844 over rock. So 4-band algorithm with emissivity approach cause bigger error at warmer temperature above 290 K. Why 5-band algorithm through

emissivity approach can reach the requirement? Because the surface emissivity at 8.55 μm band is very stable, it helps to compensate the emissivity variation at the 3.75 and 4.005 μm band.

In recent years, some scientists developed some advanced split window algorithms. In 1995, Becker and Li added water vapor correction to their original split window algorithm in 1990. In 1997, Coll and Caselles developed a new split window algorithm, added water vapor and transmittance correction. Figure 18 gave the retrieved LST error by using these algorithms and compared with the generalized split window algorithm (based on Becker and Li's 1990 algorithm with no water vapor correction). We can see that the retrieved LST bias by using the split window algorithms with water vapor correction is less than the generalized split window algorithm. Even at the water temperature above 280 K, most of the bias values are between threshold -2.5 K to 2.5 K. This demonstrates that split window algorithms with water vapor correction really corrected the water vapor's effect, gave better results than the generalized split window algorithm with no water vapor correction. But if we compared the error distribution vs. temperature value and view angles, as shown in figure 19 and 20, with our three-band and five band algorithms (see figure 14 and 15), the error performances of Becker and LI' (1995) and Coll and Caselles's (1997) are still a little worse at warmer temperature above 280 K.

3.3.6 Land cover approach

As discussed in the section 3.3.1 about the physics of the problem, for a specific surface type, the deficits between the surface temperature and the brightness temperature at 11 μm and 12 μm have very good linear relationship, therefore split window algorithm can be adopted to a specific surface type. For each surface type, we establish one set of regression coefficients between the surface temperature and 11 μm and 12 μm brightness temperature, we call this algorithm as VIIRS split window algorithm. Figure 19a displays the LST precision for different land surface types. The upper line represents the result derived from the generalized split window algorithm. The other lines present the results from the VIIRS split window algorithm (surface separated method) for various land surface types. This figure shows that the surface separated method can improve the retrieval precision for all surface types. Figure 12b shows the total statistics of retrieval for all the surface types vs. different sensor noise model. The VIIRS split window method shows better precision than that of the generalized split-window algorithm. The generalized split window algorithm can't meet the threshold 0.5 K for all sensor noise models, but VIIRS split window algorithm can meet the threshold for sensor noise model 1 to 4. However, when we analyzed the bias distribution vs. temperature values, we found that bigger error still exists for warmer temperature above 280K. This result confirmed with our discussion in the chapter 3.31 about the physics of the problem. From Figure 3a, we can see clearly that the transmittance of the 10.8 and 12 micron channels decreased significantly at the temperature range 280~310K, this is why the split window algorithms by using 10.8 and 12 μm channel cause bigger error to the warmer temperature retrieval. Even different surface type were separated when VIIRS split-window algorithm was adopted, it can only correct surface emissivity's effect, it can't eliminate the atmospheric effect (mainly water vapor absorption at most window channels).

Now that the VIIRS for the next generation polar orbiting satellite increased some new SWIR and IR window channels, such as SWIR window channel 4.005 μm band, new IR window channel 8.55 μm band, we should try to use the information offered by these new window

channels to retrieve LST. As discussed in the section 3.3.1, we can develop some good ways to combine these new bands with the 11 μm and 12 μm bands to get better LST retrieval.

We extended land surface separated method to multi-channel case. Multi-channel SST algorithms were adopted to a specific surface type, such as SST-5 bands equation, it was named VIIRS-5 bands LST algorithms as described in the chapter of mathematical description. Compared with the split window algorithms, this algorithm really got very good result, as shown in Figure 20 with the case of sensor noise model 3. As 8.55 μm band may be removed due to its large expense, we tried to remove this band at the 5-bands algorithm, the result became worse but at least better than the split window algorithms. Figure 21 show the comparison of the bias distribution between the generalized split window, VIIRS split window, VIIRS -4 bands algorithm and VIIRS-5 bands algorithm with sensor noise model 3 without solar zenith angle correction for day and night time including 10 view zenith angles. It was clearly demonstrated that split window algorithms gave bigger error at warmer temperature above 280K, VIIRS -4 bands algorithm show less error but VIIRS -5 bands got the best result.

Figure 22 further shows the precision vs. temperature distribution, LST retrieval precision for generalized split window can meet the threshold below 290K, but it got very bad precision for warmer temperature above 290K. VIIRS-5 bands algorithm got the best precision for all temperature range, the precision can be below 0.5 K for all temperature case.

As discussed above, Five-band algorithms no matter emissivity approach or land-cover approach got the best precision, but they depend on the new 8.55 μm band. In case of this band maybe removed due to its higher expense, we must explore a good way to use other bands to overcome split window algorithms' shortcoming to try to meet the threshold for all temperature case. From the discussion about the physics of the problem, at SWIR bands 3.75 μm and 4.005 μm , there is the so-called solar glint existed, during daytime, the brightness temperature at these two bands can be much higher than the surface temperature due to the surface reflection to the solar radiation. So solar correction is needed when these bands are used to retrieve LST during daytime. We attempted to add solar zenith angle correction during daytime by using VIIRS -4 bands algorithm when 8.55 μm band was supposed to be removed. As shown in Figure 23, it can get almost the same good result as VIIRS-five bands algorithm. So solar zenith angle correction is very important when SWIR bands 3.75 μm and 4.005 μm are used to retrieve LST during daytime. In section 3.3.5, we tried the same way to add the solar correction to our emissivity 4 - band algorithm, there is no significant improvement to the warmer temperature above 290 K. This is because the variation of the surface emissivity at the 3.75 and 4.005 μm bands was observed to be very large, as shown in table 4 and Figure 6.

From the discussion above, VIIRS-4 band day/night LST algorithm (LC approach) with solar zenith angle correction and 5 band LST algorithm (emissivity approach) gave the best precision and the precision can meet the threshold 0.5 K at all LST and satellite view angles.

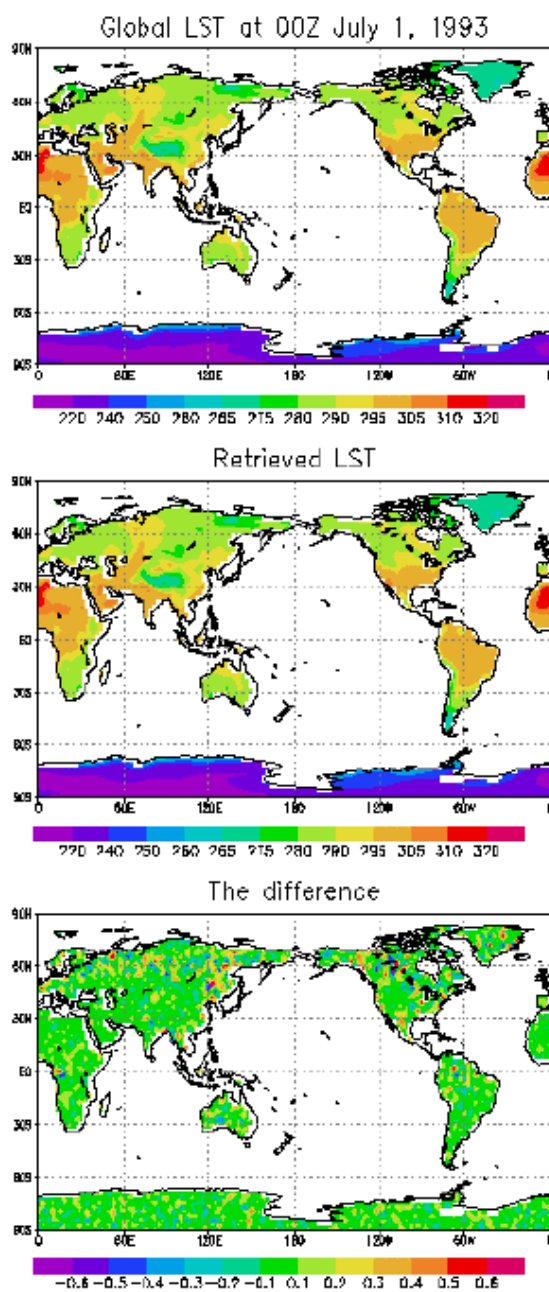


Figure 11. Upper panel: Global LST. Middle panel: Retrieved LST. Lower panel: The difference between the LST values.

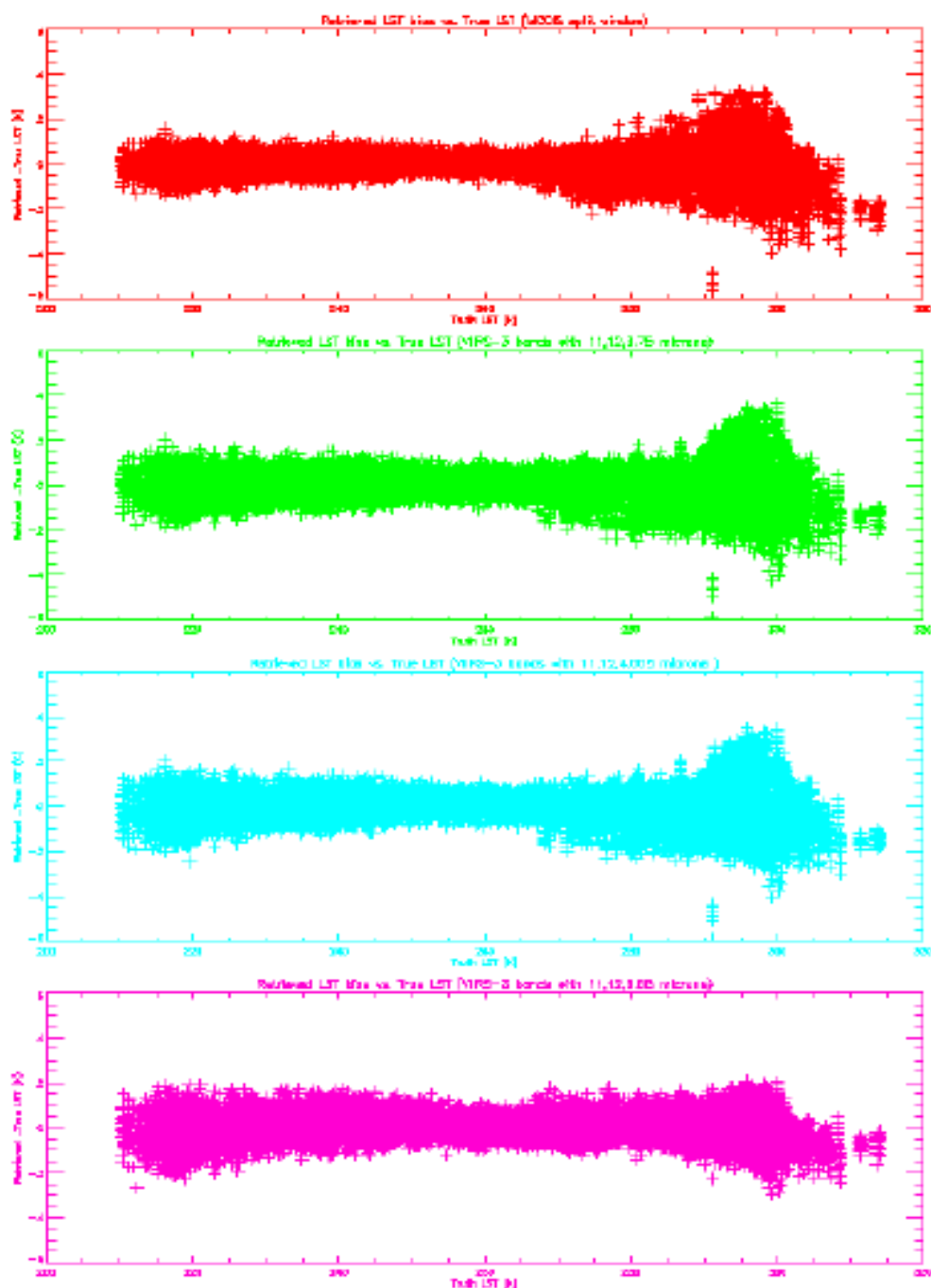


Figure 12. LST retrieval error vs. temperature distribution with SNR 3 for VIIRS-new band algorithm with different combination, compared with generalized split window. The upper panel: generalized split window. The second: 11,12 and 3.75 μm . The third: 11, 12 and 4.005 μm . The bottom: 11, 12 and 8.55 μm .

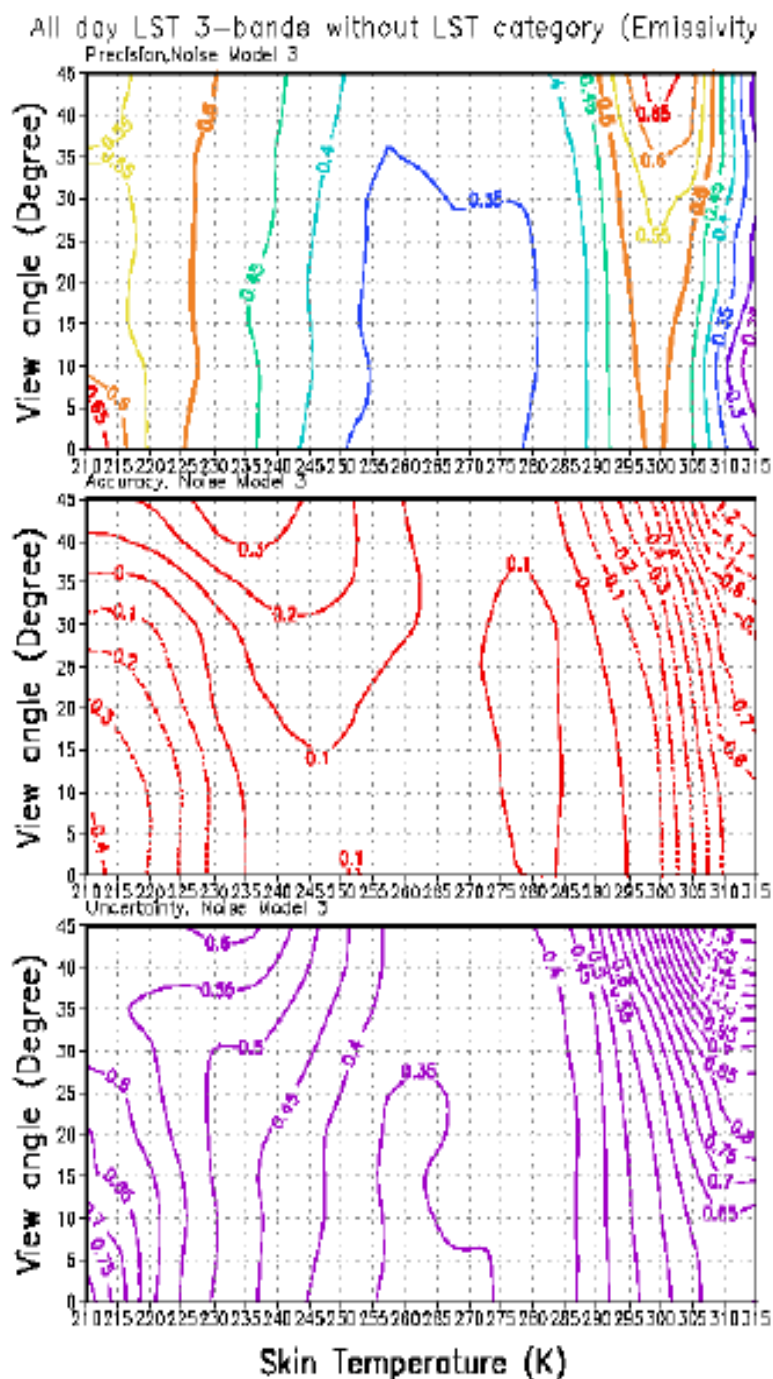


Figure 13 LST precision (upper panel), accuracy (middle) and uncertainty (bottom) distribution vs. satellite view angle and LST for 3-band algorithm (emissivity approach) without temperature category.

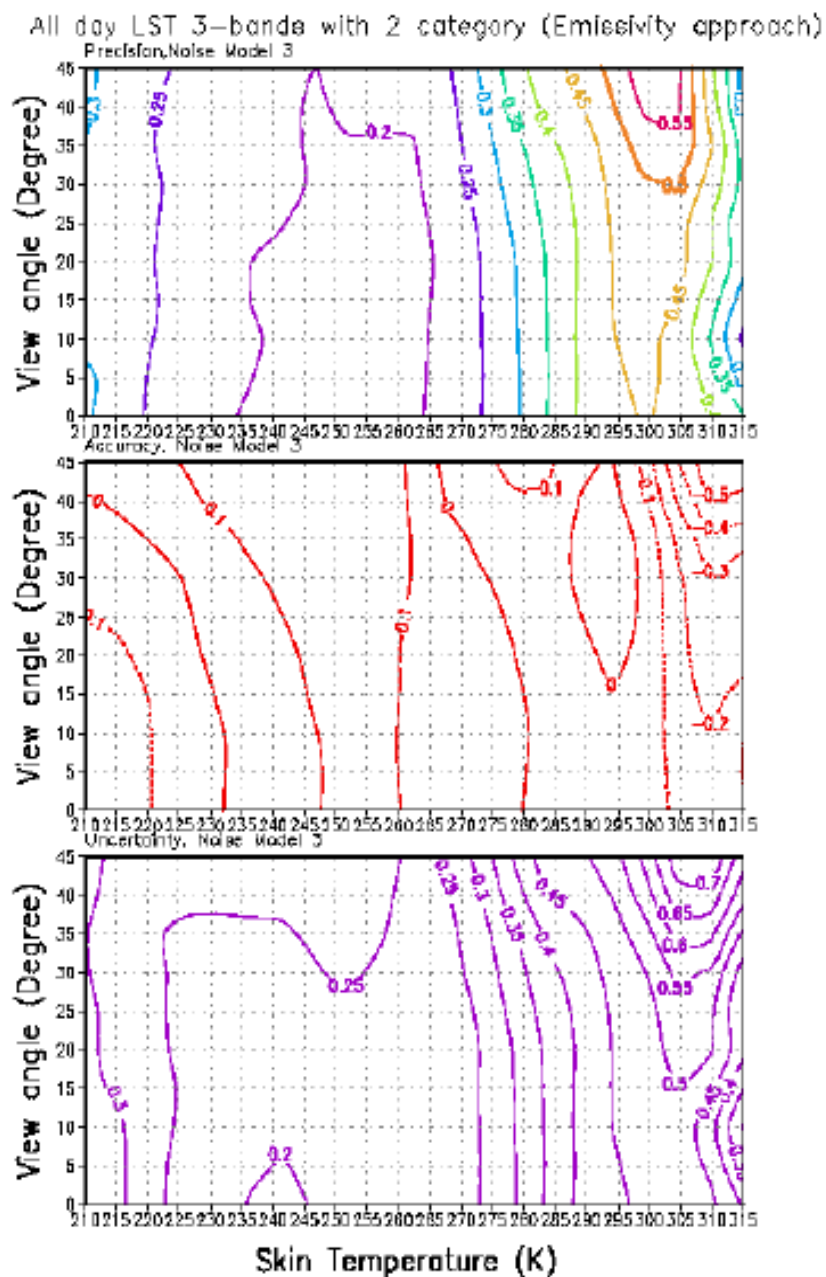


Figure 14. Same as figure 13, but with two temperature category (below 285 K) and above 285 K.

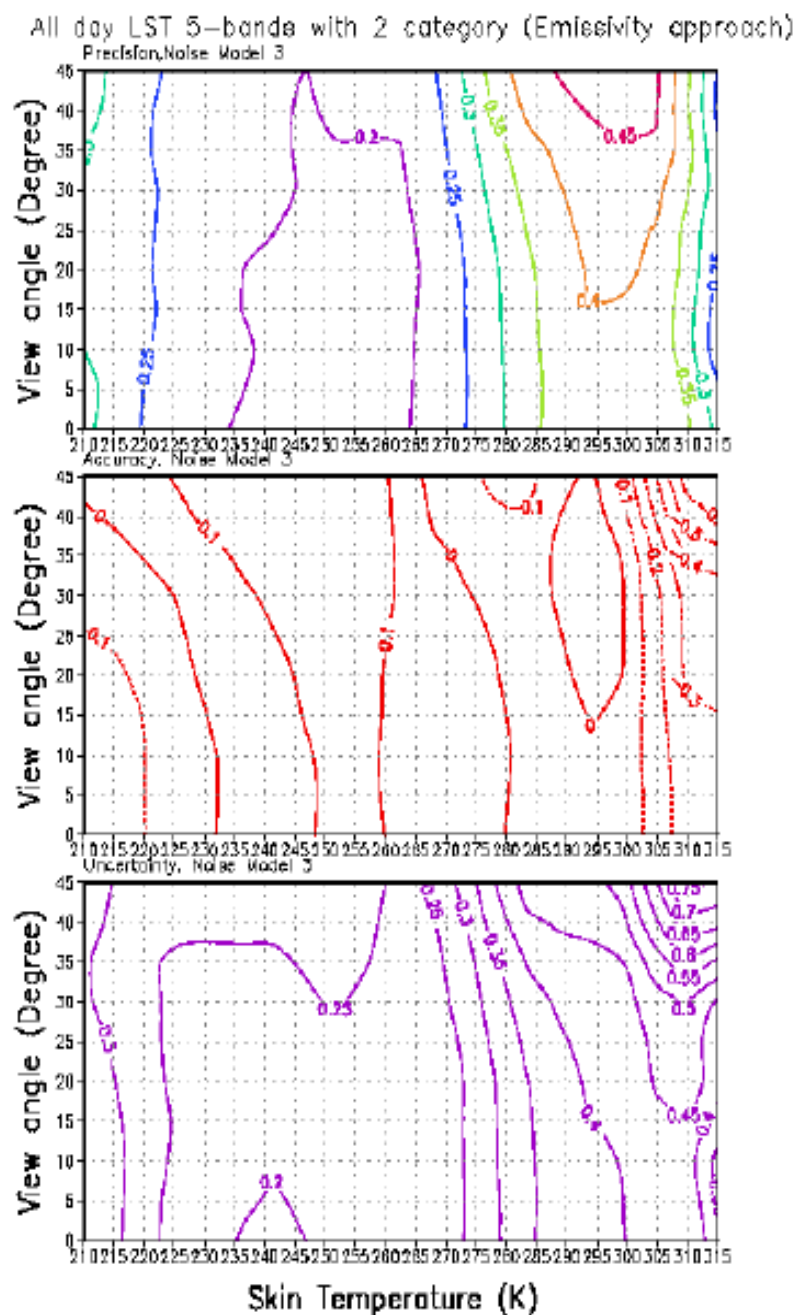


Figure 15 LST precision (upper panel), accuracy (middle) and uncertainty (bottom) distribution vs. satellite view angle and LST for 5-band algorithm (emissivity approach) with two-temperature category below 285 K and above 285 K.

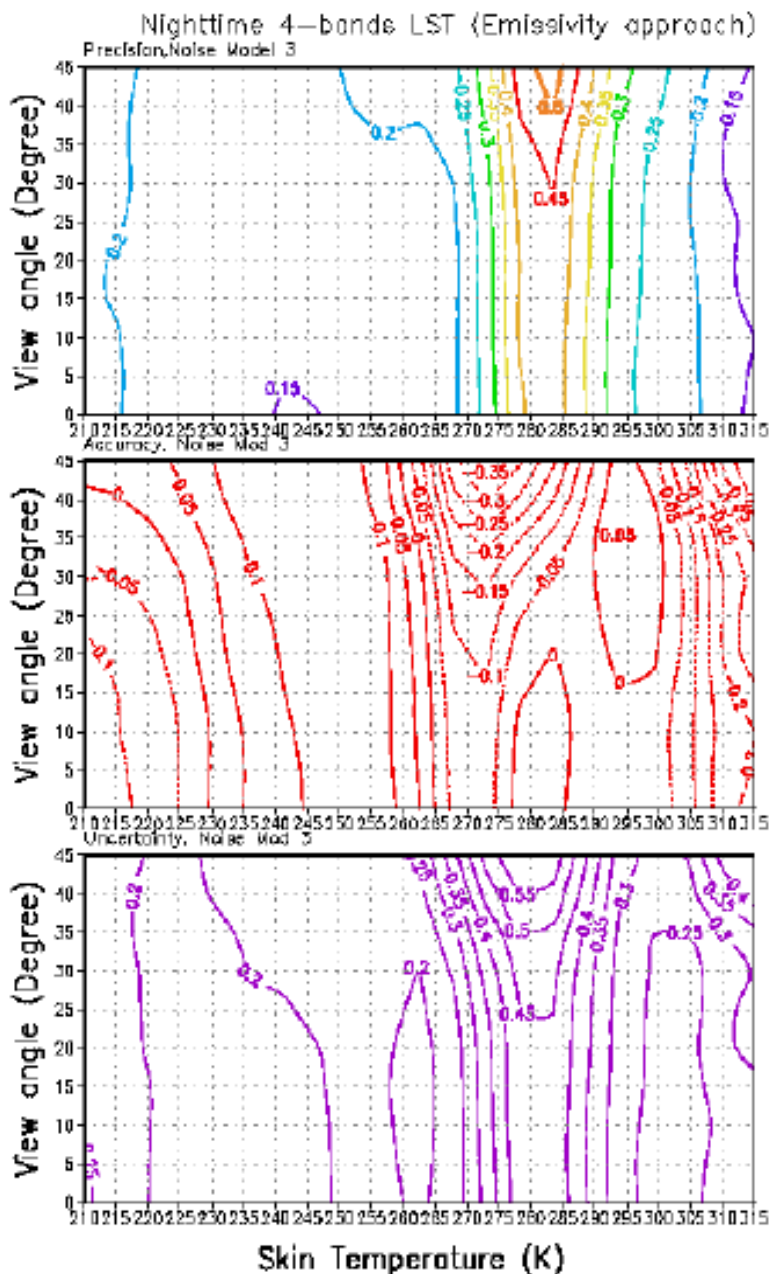


Figure 16 Nighttime LST precision (upper panel), accuracy (middle) and uncertainty (bottom) distribution vs. satellite view angle and LST for 4-band algorithm (emissivity approach) with two temperature category below 285 K and above 285 K.

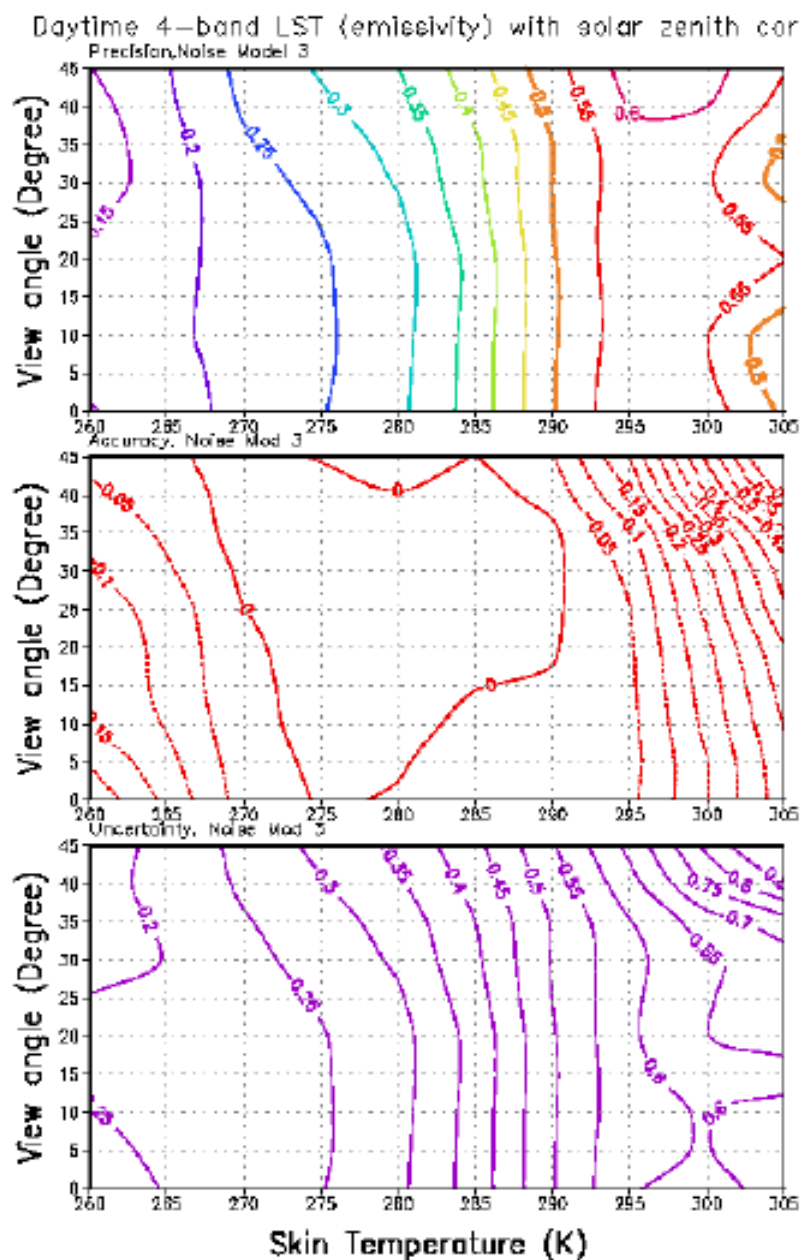


Figure 17 Daytime LST precision (upper panel), accuracy (middle) and uncertainty (bottom) distribution vs. satellite view angle and LST for 4-band algorithm (emissivity approach) with solar zenith correction with two temperature category below 285 K and above 285 K.

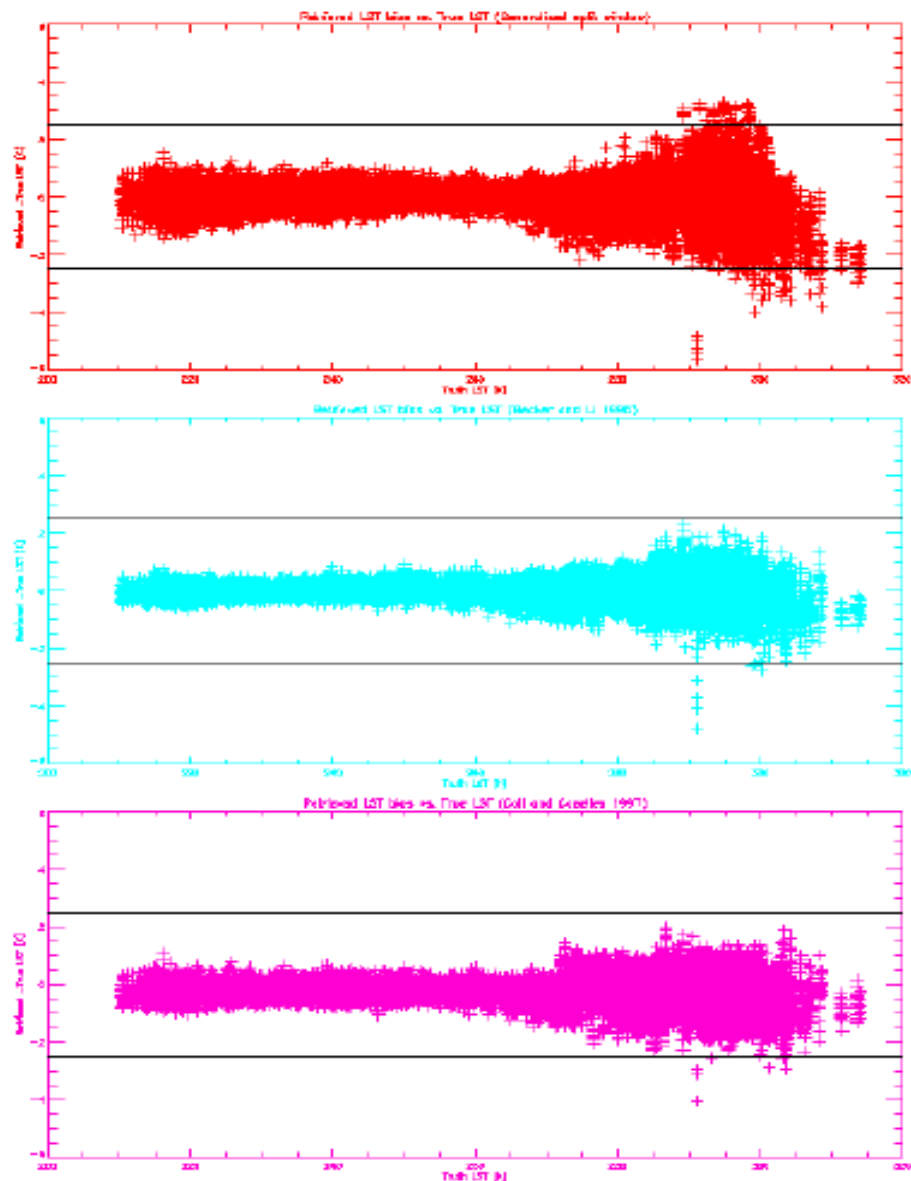


Figure 18. LST retrieval error vs. temperature distribution with SNR 3 some split window algorithms. The upper panel: generalized split window. The second: Becker and LI' 1997 split window algorithm with water vapor correction. The third: Coll and Case11es's (1997) split window algorithm with water vapor correction.

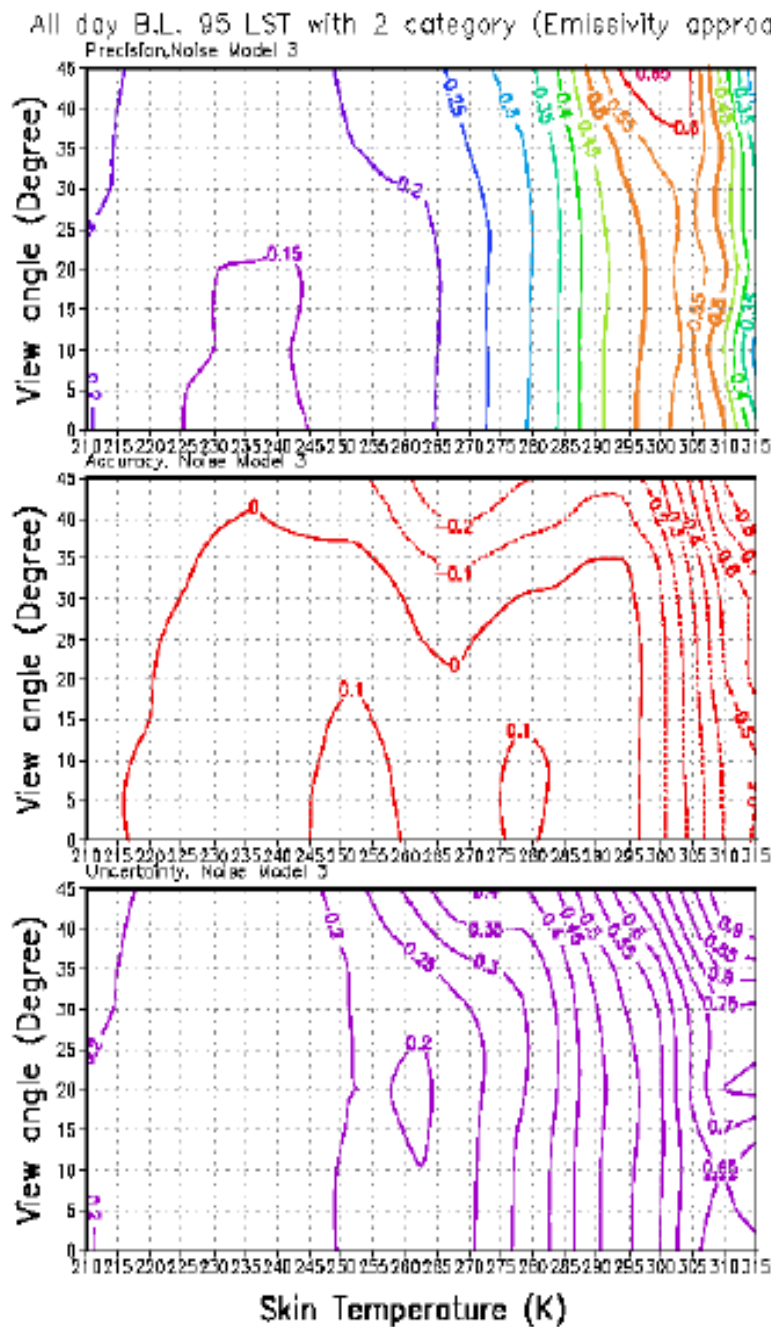


Figure 19. LST precision (upper panel), accuracy (middle) and uncertainty (bottom) distribution vs. satellite view angle and LST for Becker and Li's(1995) split window algorithm (emissivity approach with water vapor correction) with two-temperature category below 285 K and above 285 K.

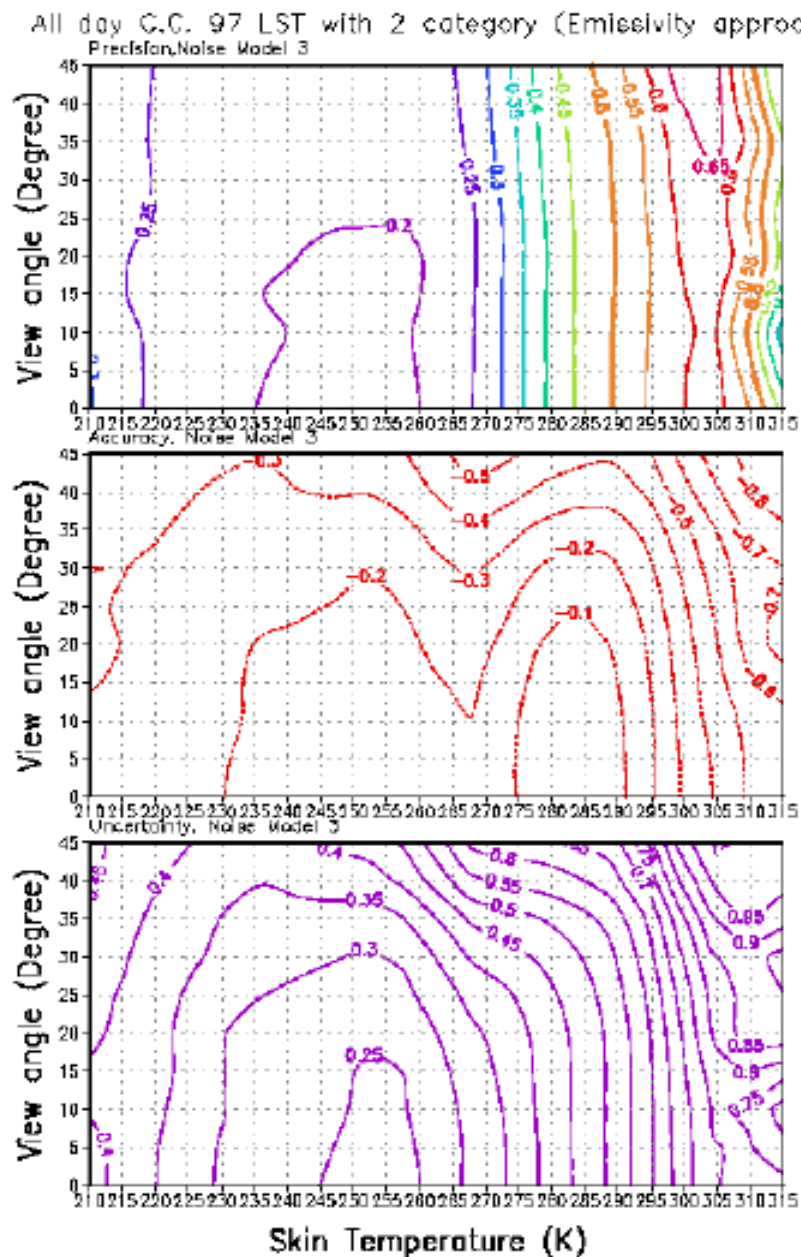


Figure 20. LST precision (upper panel), accuracy (middle) and uncertainty (bottom) distribution vs. satellite view angle and LST for Coll and Caselles's (1997) split window algorithm (emissivity approach with water vapor correction) with two-temperature category below 285 K and above 285 K.

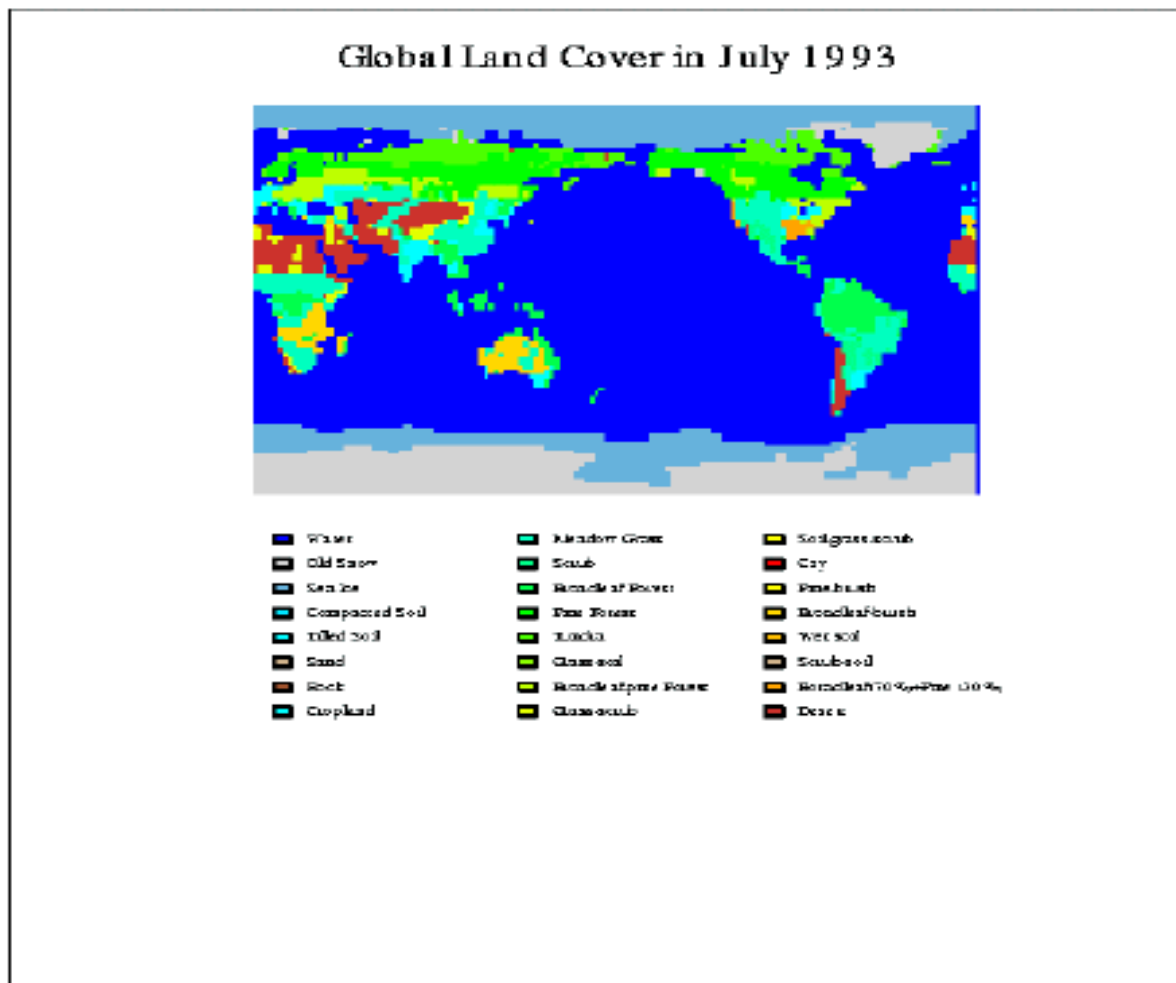


Figure 21. Global land cover distribution in July 1993.

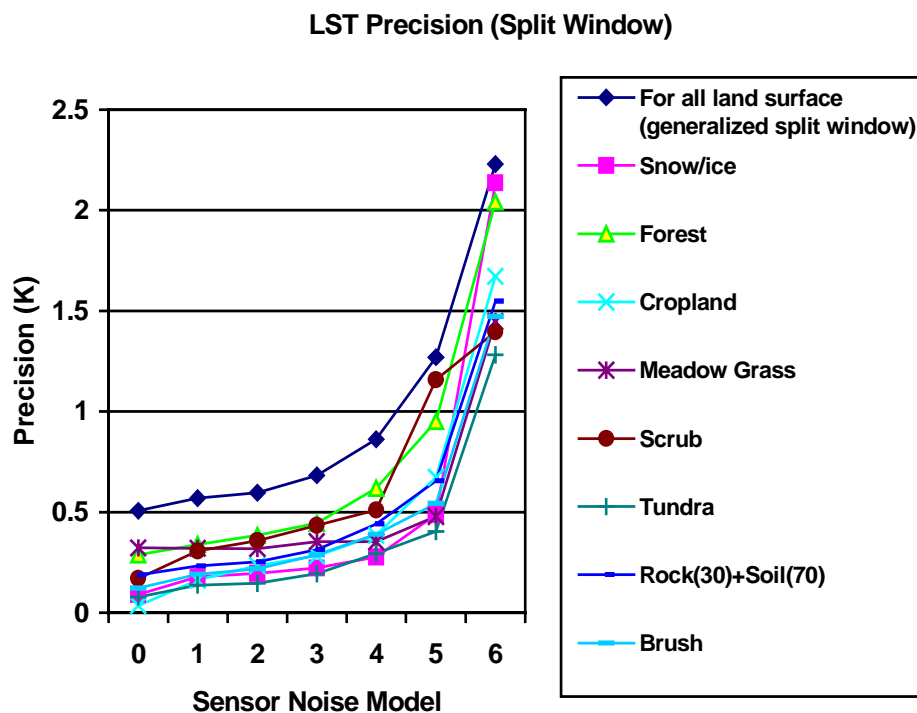


Figure 22a. Precision analysis for the two different retrieval methods.

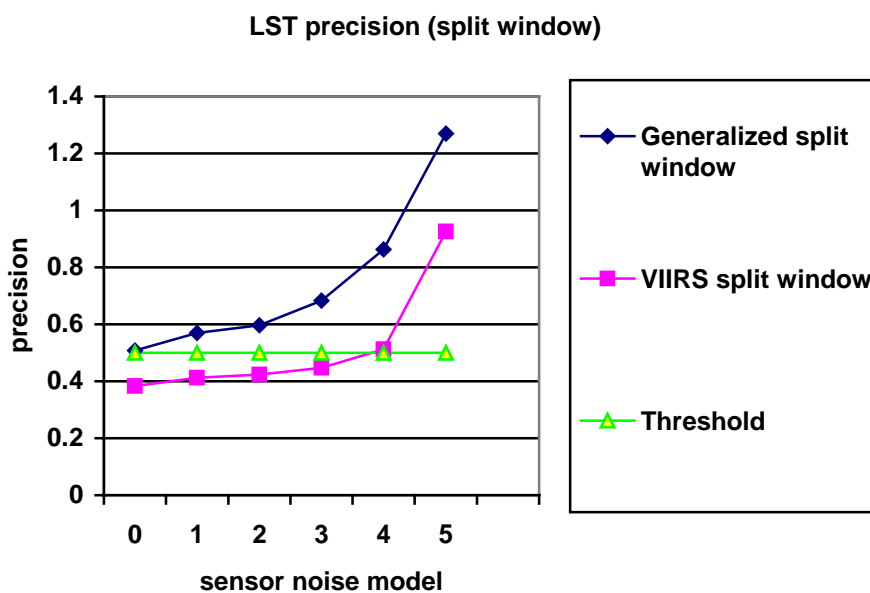


Figure 22b. Global LST retrieval precision from the two retrieval methods.

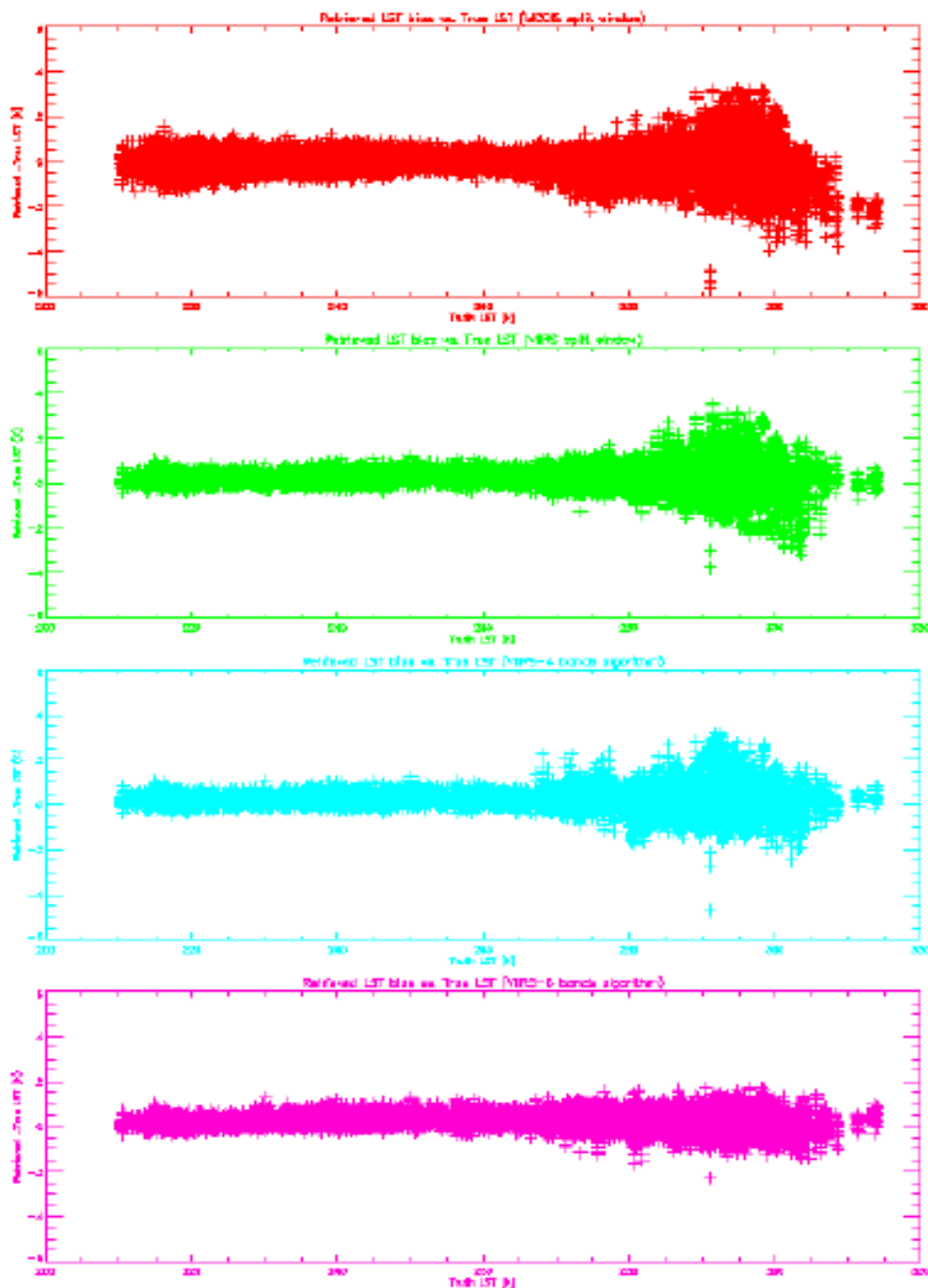


Figure 23. LST retrieval error distribution with sensor noise model 3 for different approaches. The upper panel is for generalized split window, the second panel is for VIIRS-split window, the third is for VIIRS-4 band without solar zenith correction, the bottom panel is for VIIRS-5 bands algorithm (LC approach).

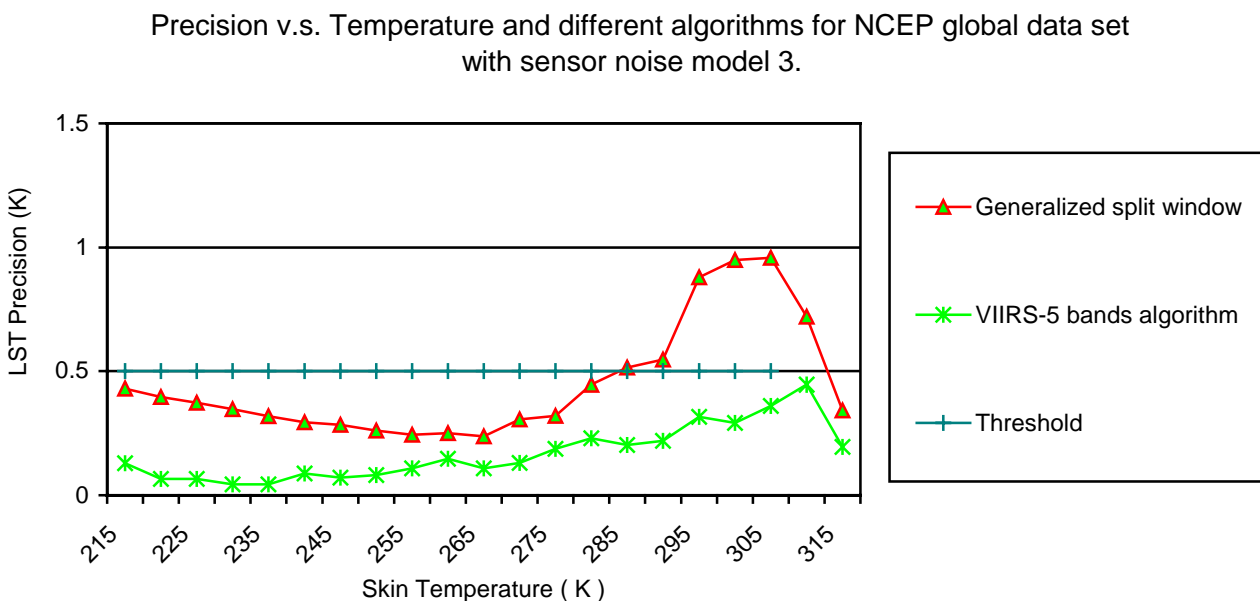


Figure 24. LST retrieval precision vs. temperature distribution for generalized split window, VIIRS-new algorithm and VIIRS-5 bands algorithm.

From Figure 22 and 23, we can see VIIRS-4 bands algorithm with solar zenith angle correction can get very good result as VIIRS-5 bands algorithm. So in case of 8.55 μm is removed. We can use this algorithm.

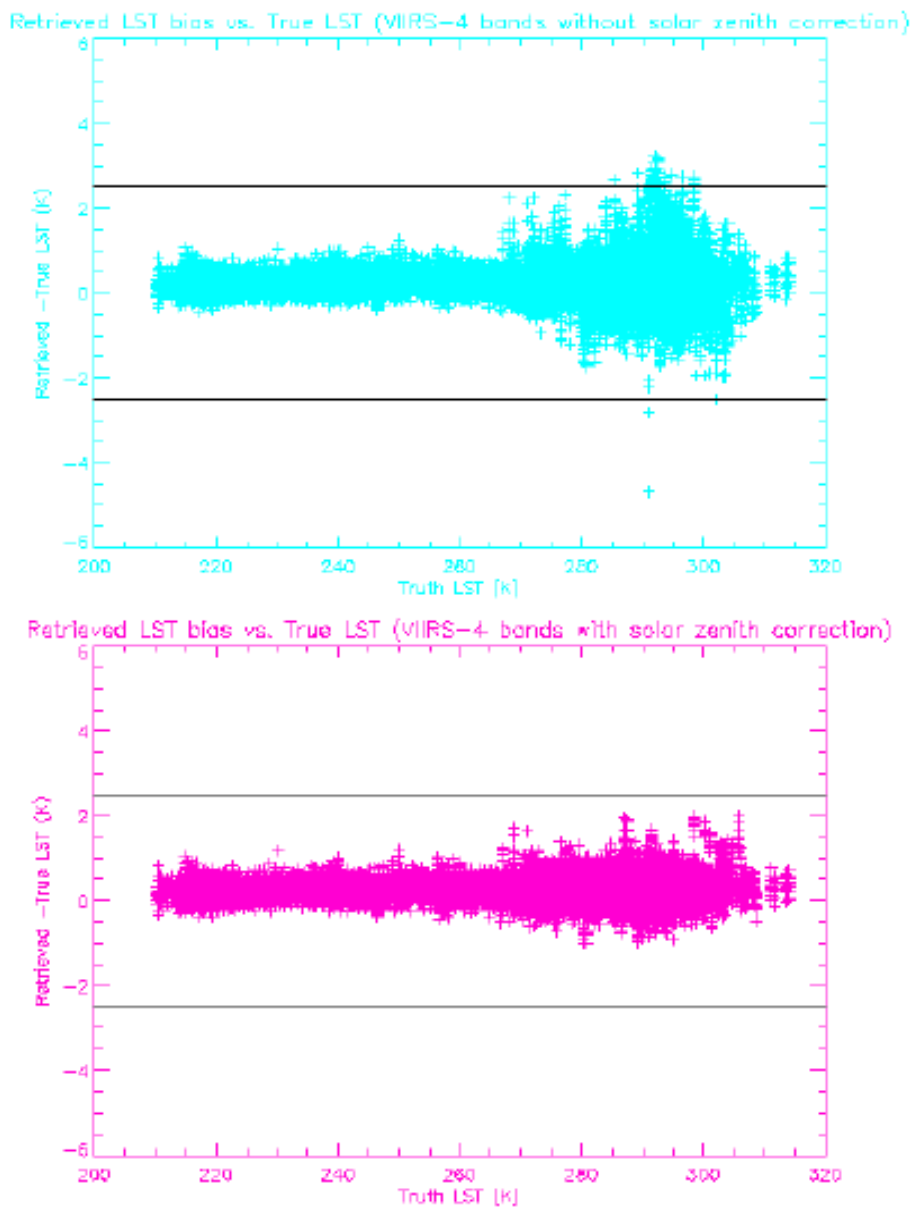


Figure 25. LST retrieval error vs. LST distribution for VIIRS-4 bands algorithm. The upper panel: Without solar zenith angle correction. The bottom panel: With solar zenith angle correction during the daytime.

**Precision v.s. Temperature for VIIRS-4 band day/night algorithm
for NCEP global data set with sensor noise model 3.**

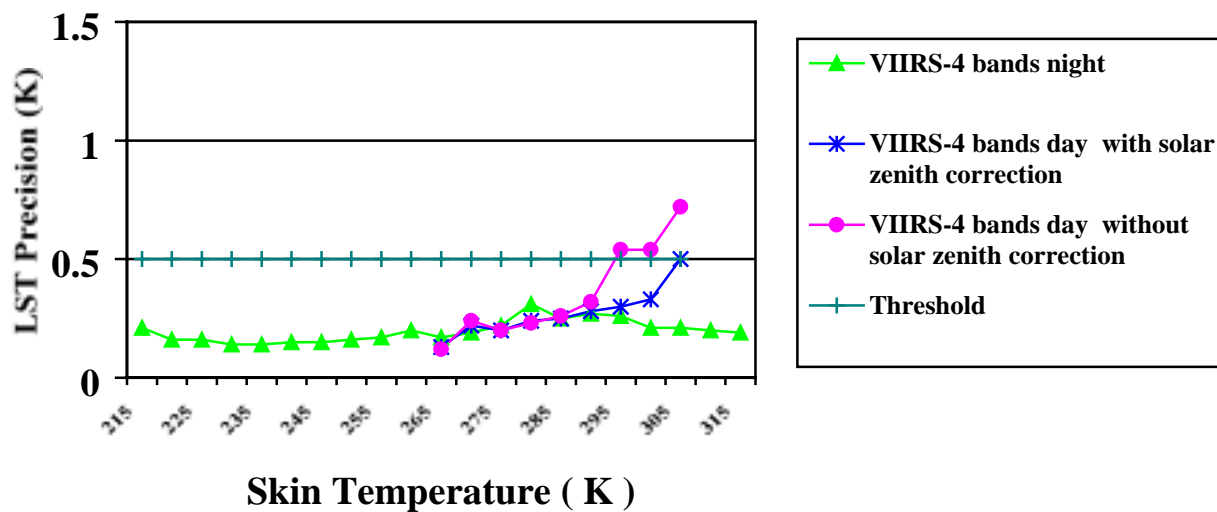


Figure 26. Comparison of LST precision distribution over LST for VIIRS-4 band algorithm (LC approach) during nighttime, and daytime with and without solar zenith correction.

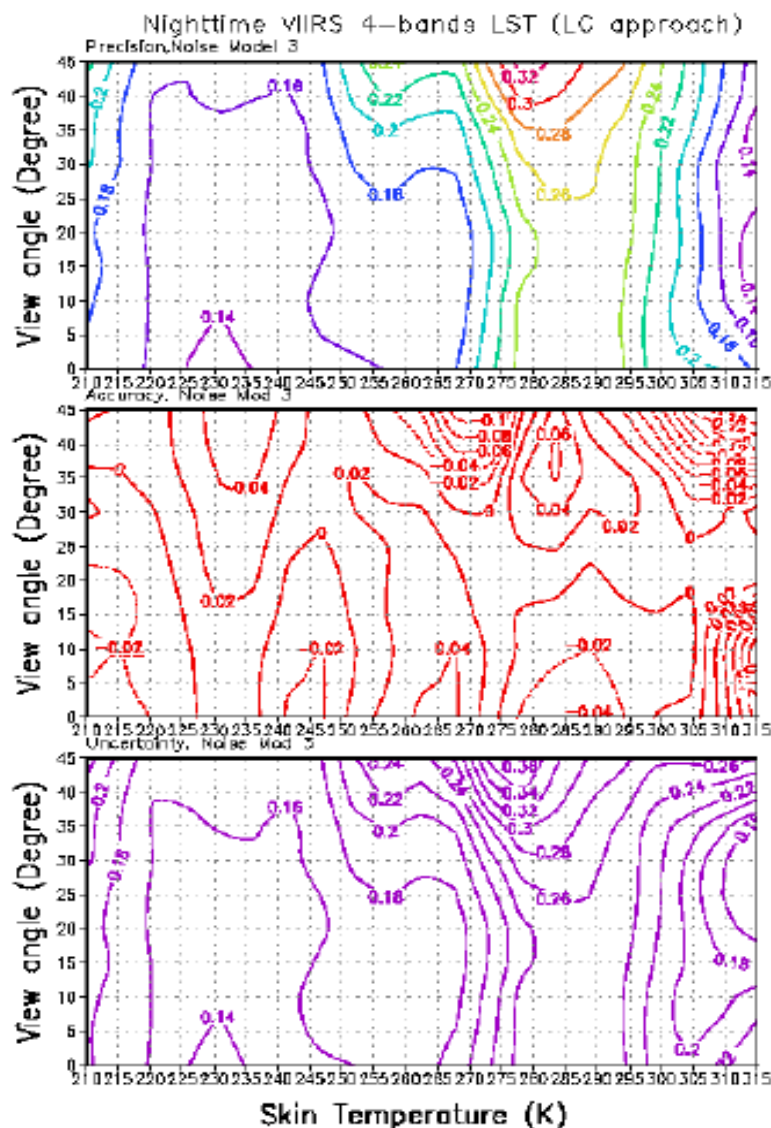


Figure 27. Nighttime LST precision (upper panel), accuracy (middle) and uncertainty (bottom) distribution over satellite view angle and LST by using VIIRS-4 band algorithm (LC approach) .

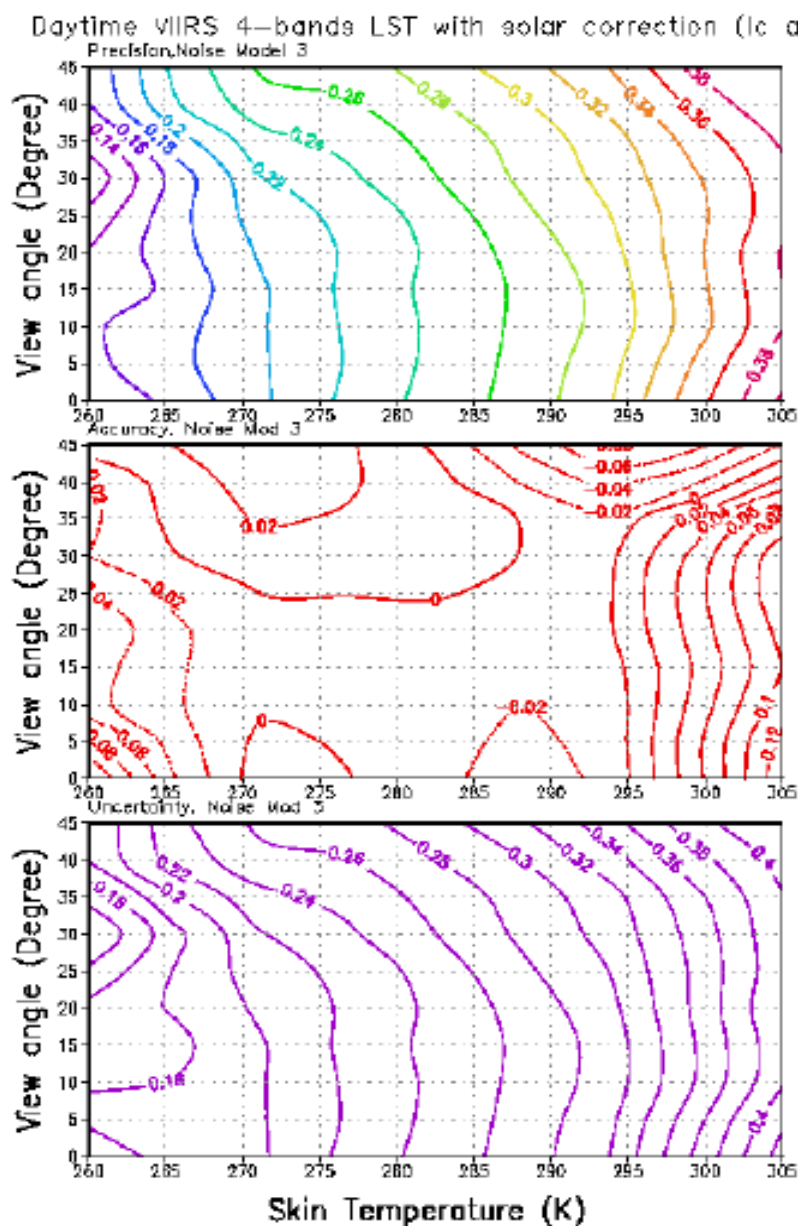


Figure 28. Daytime LST precision (upper panel), accuracy (middle) and uncertainty (bottom) distribution over satellite view angle and LST by using VIIRS-4 band algorithm (LC approach) with solar zenith correction.

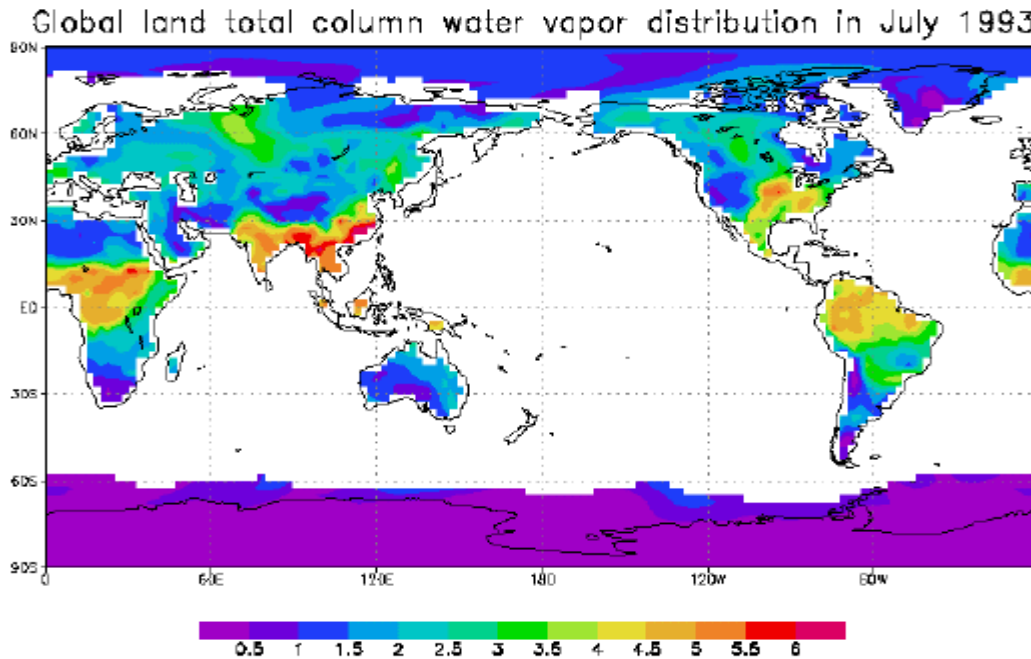


Figure 29. Total column water vapor distribution over land in our global dataset.

3.3.7 Water vapor's effect

In window channels, the main atmospheric effect comes from the water vapor absorption. So the total column water vapor amount has important effect to LST retrieval error. Figure 29 show the total column water vapor (TCWV) distribution in this global dataset.

Because more water vapor exists at higher temperature, as shown in figure 3(a), and LST bigger error occurred at warmer temperature above 280 K. So we emphasized to analyze the relationship of LST retrieval error at temperature range 280-305 K with water vapor amount. Figure 30 shows the LST retrieval precision, accuracy and uncertainty distribution at warmer temperature (280-305 K) over total column water vapor and satellite view angle by using the generalized split window algorithm. The LST precision is greater than the threshold 0.5 K for water vapor amount greater than 0.5 g/cm², it increases with the water vapor amount, especially for water vapor greater than 5 g/cm², and the LST precision increases rapidly. Between TCWV 3 - 5 g/cm², LST precision increases with the satellite view angle. Split window algorithms with water vapor correction such as Becker and L's (1995) (figure 31) and Coll and Caselles's (1997) (figure 32) shows better precision, the retrieved LST precision can meet the threshold between TCWV 1.0 to 3.0 g/cm² for Becker and Li's (1995) algorithm. But their performances are still as well as our 3-band and five-band (emissivity approach) and 4-band algorithm (Land cover approach). The 3-band algorithm with emissivity approach show (figure 28) better precision than the generalized split window, the LST precision can meet the threshold 0.5 K at TCWV 1.0 to 5.5 g/cm², it can't meet the threshold at TCWV 0.5-1.0 g/cm² and greater than 5 g/cm². It increases with the TCWV amount and the view angle for TCWV greater than 4.5 g/cm². Although the 5-band LST algorithm with emissivity approach can meet the threshold at all temperature range and view angle, as shown in figure 15, if we show the its error distribution with the TCWV, see figure 29,

the precision can't meet the threshold at TCWV 0.5 g/cm² and for TCWV greater than 4.5 g/cm², the precision is greater than 0.5 K for view angle greater than 20 degree.

One point needs to be especially noticed the LST precision is bigger at TCWV 0.5-1.0 g/cm². We checked figure 26 and figure 18 and found TCWV amount between 0.5 to 1.0 g/cm² corresponds to rock, sand, desert or sea ice area. Since we just analyzed warmer temperature above 280 K, it is mainly the rock, sand, and desert, the surface emissivity of 3.75 and 4.005 μm bands over sand, rock and desert existed big variation. This is why the LST retrieval with emissivity approach cause big error at TCWV 0.5 –1 g/cm². Harris and Mason (1992) revealed that for a given change in surface temperature ΔT₀, resulting in changes in brightness temperatures in the two wavebands has the following relationship:

$$\frac{\Delta T_2}{\Delta T_1} = \frac{\epsilon_2}{\epsilon_1} \frac{\tau_2(0, p_0)}{\tau_1(0, p_0)} \quad (39)$$

$$\tau_\lambda(0, p_0) = \exp(-k_{w\lambda} U_w(0, p_0)) \exp(-k_{o\lambda} U_o(0, p_0))$$

So surface emissivities as well as atmospheric transmittance changes cause brightness temperature change. If we divide the absorbing gases into water vapor and other gases

$$\frac{\Delta T_2}{\Delta T_1} = \frac{\epsilon_2}{\epsilon_1} \exp((k_{w1} - k_{w2}) U_w(0, p_0)) \exp((k_{o1} - k_{o2}) U_o(0, p_0))$$

Where $k_{w\lambda}$ and $k_{o\lambda}$ are the band-averaged absorption coefficients for water vapor and other gases, respectively; $U_w(0, p_0)$ and $U_o(0, p_0)$ are the total column contents of water vapor and other gases, respectively. Apply this to equation (39), we have

Suppose the magnitude $(k_{w1} - k_{w2}) U_w(0, p_0)$ is small, and it is reasonable to take the first-order expansion, As $U_w(0, p_0)$ is the total column water or precipitable water W, so we have

$$\frac{\Delta T_2}{\Delta T_1} \approx \frac{\epsilon_2}{\epsilon_1} (1 + KW + \text{const.}) \quad (40)$$

So surface emissivity and atmospheric total column water vapor cause the brightness temperature change and therefore cause LST retrieval error. At TCWV 0.5-1.0 g/cm², the is mainly the emissivity change at the 3.75 and 4.005 μm bands over rock, sand and desert cause LST retrieval error. This is also why LST precision by the 4-band LST algorithm with emissivity approach is greater than 0.5 K at the warmer temperature above 290 K.

While VIIRS-4 band algorithm by land cover approach show the LST precision can meet the threshold 0.5 K at all TCWV range and all view angles, shown as Figure 30. This is because this method overcomes the surface emissivity's effect.

In order to find the best LST algorithm, we compared our algorithm developed here with the physical retrieval discussed in section 3.3.2, and some published algorithms. Since some LST

algorithms developed recently like Becker and Li (1995) and Coll and Caselles's (1997) algorithms need the total column water vapor or precipitable water and the transmittance, we did simulation to the IPO 2415 profiles over land under clear condition by using MODTRAN 3.7. And we output the atmospheric transmittance at VIIRS 3.75, 4.005, 8.55, 11 and 12 μm bands and calculated the total precipitable water for each profiles. We firstly tried some published algorithms with their published coefficients. Since there is no land cover information in this dataset, so we can only try our emissivity approach algorithms with the global training coefficients. WE also tried the physical retrieval; we combined 230 CrIS channels (CrIS simulation came from CrIS group) with the VIIRS bands and used singular value decomposition with 200 eigenvectors as the initial guess field. The results was shown in figure 31, Becker and Li's 1995 new algorithm got the best precision 0.42 K, our 5-band algorithm got 0.51 K, 3-band algorithm got 0.68 K, physical retrieval got 0.7 K, Coll and Caselles's (1997) algorithm got 0.87 K precision, respectively. Some published algorithms such as Price (1984), Becker and Li' (1990, the basis for generalized split window), Vidal (1991, based on Becker and Li 1990) by using their published coefficients got very big error. This is because maybe their coefficients came from LOWTRAN simulation or from the model standard atmosphere, but our IPO dataset have thousands of profiles, for those algorithms which didn't consider the profile's information (such as total column water vapor or atmospheric transmittance) surely cause bigger error. If we took 30% data from this dataset for training, then the precision became much better, see figure 32, Our 5-band algorithm got the best precision 0.31 K, Becker and Li (1995) and Coll and Caselles's (1997) algorithms also got better precision. This is because they considered the water vapor and the atmospheric transmittance's effect, and did some correction to the atmospheric water vapor absorption. So split window algorithms with water vapor and transmittance correction can get also get good LST retrieval. The problem is that usually this information can't be available. The physical retrieval introduced here needs a large amount of sounding channels; otherwise, it's more computer time-consuming. It maybe used for CrIS profile retrieval since their horizontal resolution is just 50 km, but our VIIRS resolution is required to be about 1.3 km, so this physical retrieval algorithm can't be used operationally for our VIIRS, we can just used it for research purpose. So 5-band algorithm with emissivity approach we developed here is a feasible way to retrieve LST in case of the surface land cover information can't be available.

From the above discussions, we can see most existing split window LST algorithms used 10.8 and 12 μm bands, because the surface emissivity at the 10.8 and 12 μm are more stable than other bands, and the 3.75 or 3.9 μm are contaminated by solar radiation during daytime. From the physical discussion of chapter 3.3.1, we can see that the atmospheric transmittance at 10.8 and 12 μm channel decreased significantly at the warmer temperature range 280-310K. So split window algorithms by using 10.8 and 12 μm bands without transmittance or water vapor correction can't get good estimation to warmer temperature above 280K, as shown in Tercat scene LST retrieval (Figure 10). Although some algorithms developed recently considered the water vapor or atmospheric transmittance effect and got better LST retrieval, but usually these information can't be available. In our VIIRS-4 band day/night LST algorithm with land cover approach, we added 3.75 and 4.005 μm band and add solar zenith correction during daytime to overcome the so called solar glint problem, otherwise, since we retrieve LST to each surface type separately, it overcomes the surface emissivity's effect. Therefore it can get better result. But due to our regression coefficients for each surface type came from our global training data set, if the surface

types for a local scene can't match our global database, or surface type information can't be available, we can use our new 5- band algorithm with emissivity approach to retrieve LST. In this new algorithm, both of the surface reflection and the atmospheric emission were considered, so it should be expected to get better result than the split window algorithms under the condition that the water vapor information can't be available.

We further compared our new algorithm with some of the existing algorithms' behavior based on IPO Olympic land scene. As shown in the upper panel of figure 33, the truth LST for this scene is colder than the Tercat scene, temperature values are below 294K. So we can expect the existing split window algorithms can also get good precision. Due to only 5 surface types in this scene match our global database, so VIIRS baseline algorithm can't be used here. 5-band algorithm was used to retrieve the LST, The middle panel is the retrieved LST, and the bottom panel is the bias distribution. We can see that the retrieved LST agreed quite well with the truth LST, the bias error is between $-0.6\sim0.6$ K. Figure 34 upper panel shows the LST retrieval precision distribution for different algorithms with IPO 600m Olympic scene. As we can see the new 5-band algorithm developed here gave the best precision, while Price's algorithm (Price, 1984) got the worst precision. Prata's algorithm (Prata 1998) got the best accuracy; 5-band algorithm and the generalized split window algorithm overestimate the LST below 288 K.

From the above discussions, we can see that VIIRS 4 –band day/night algorithm with land cover approach got the best LST retrieval, so we define this algorithm as our baseline algorithm. In case of the surface land cover information can't be available or the surface types for a local scene can't match our global training databases, we take 5-band algorithm with emissivity approach as our alternative baseline algorithm.

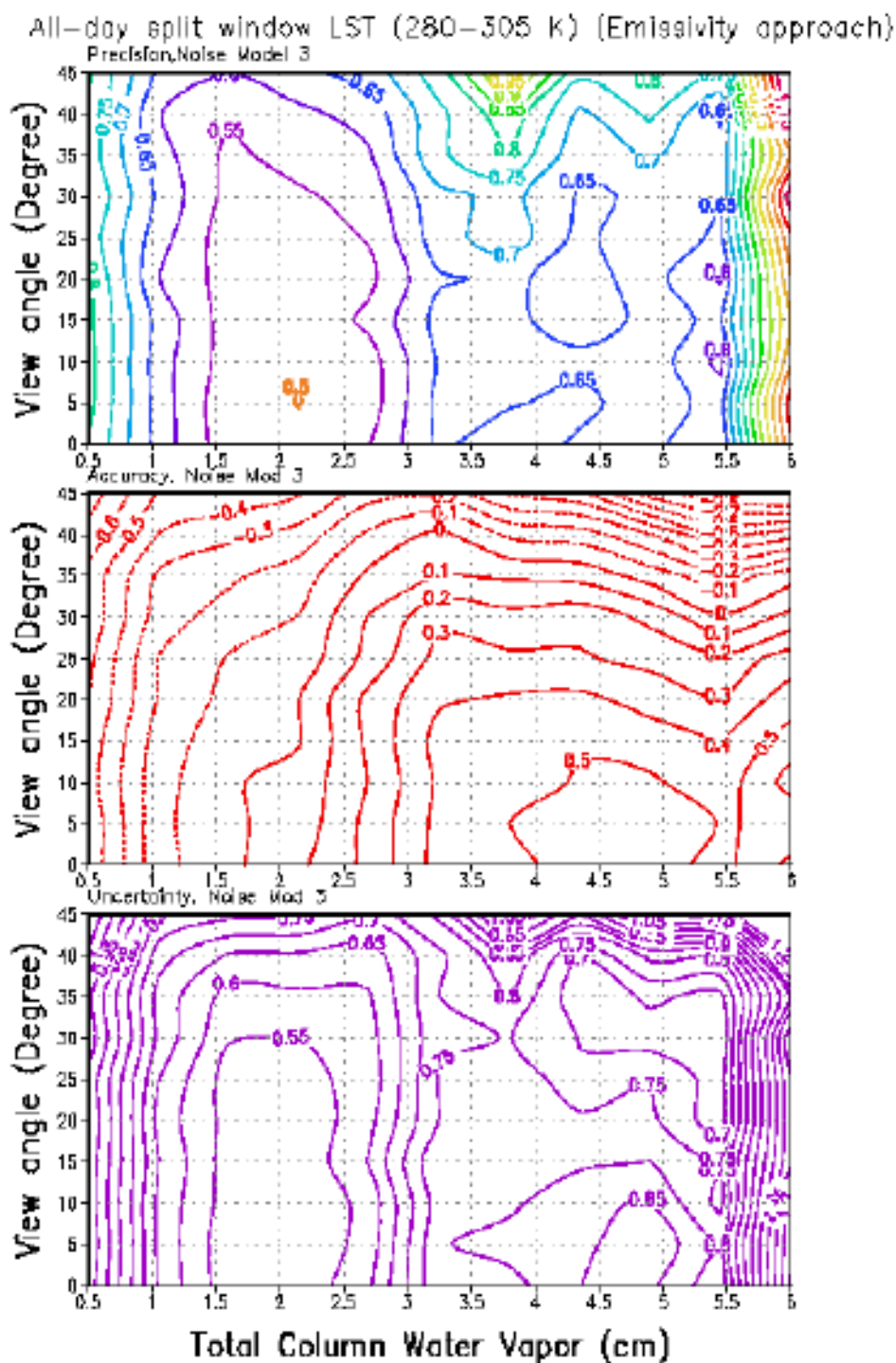


Figure 30. The LST precision, accuracy and uncertainty distribution with the TCWV and view angle by using the generalized split window algorithm.

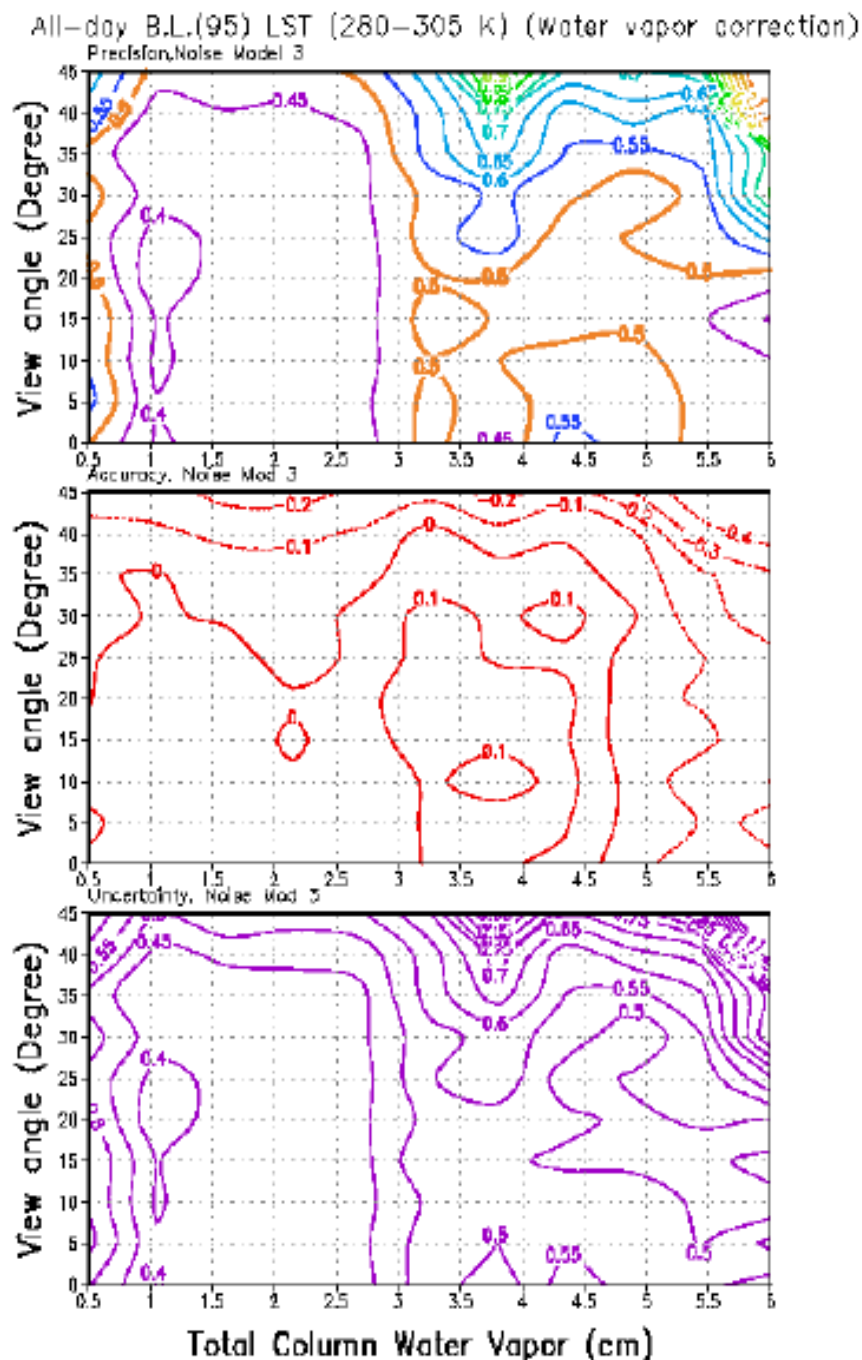


Figure 31. The LST precision, accuracy and uncertainty distribution with the TCWV and view angle by using Becker and Li's (1995) split window algorithm (with water vapor correction).

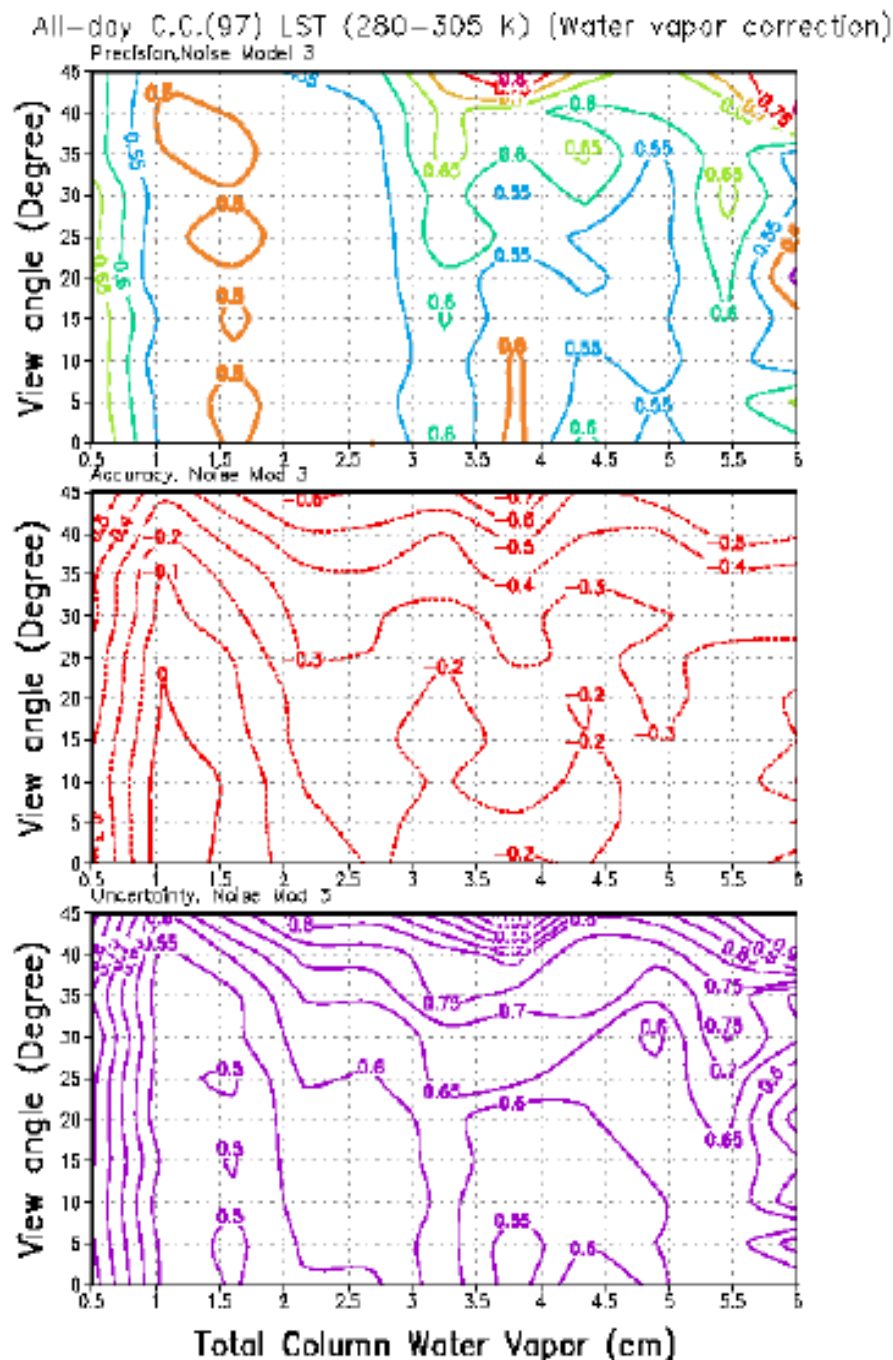


Figure 32. The LST precision, accuracy and uncertainty distribution with the TCWV and view angle by using Coll and Caselles's (1997) split window algorithm (with water vapor correction).

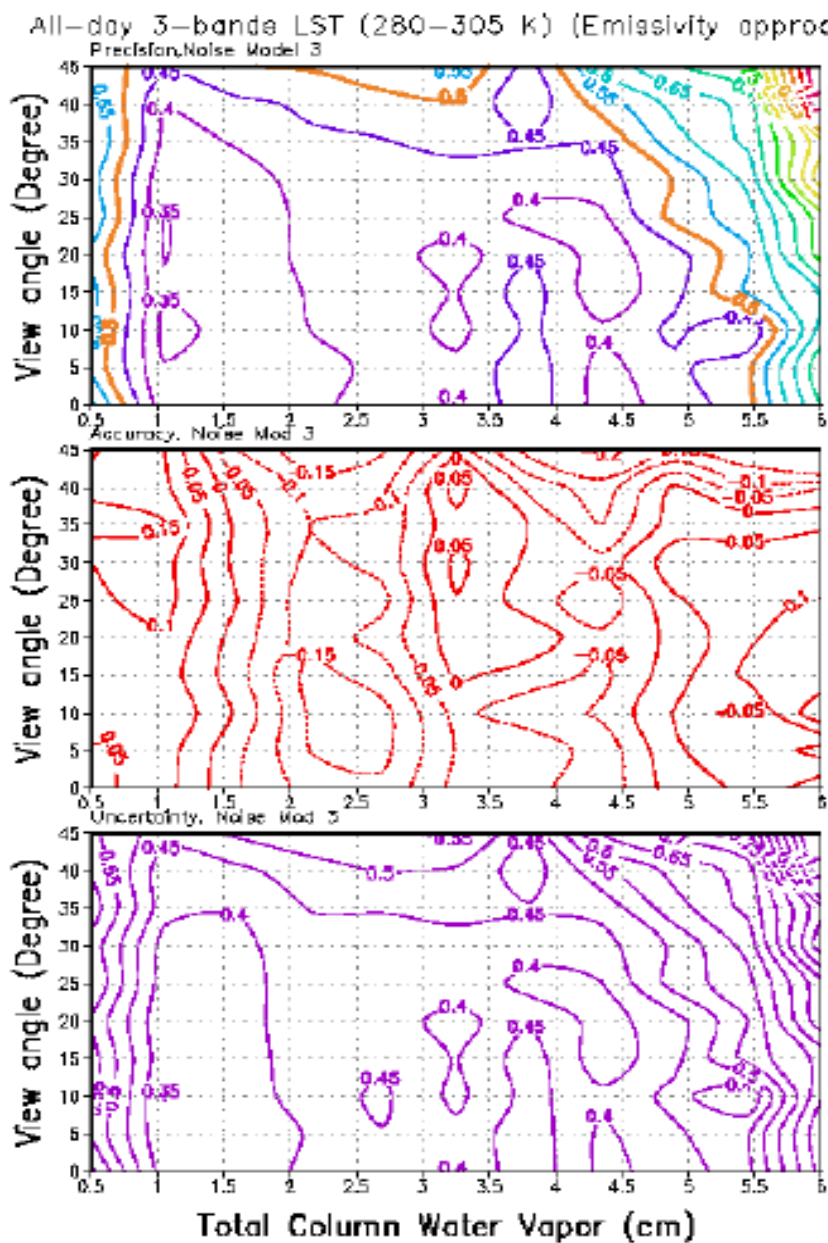


Figure 33. The LST precision, accuracy and uncertainty distribution with the TCWV and view angle by using the 3-band algorithm (emissivity approach).

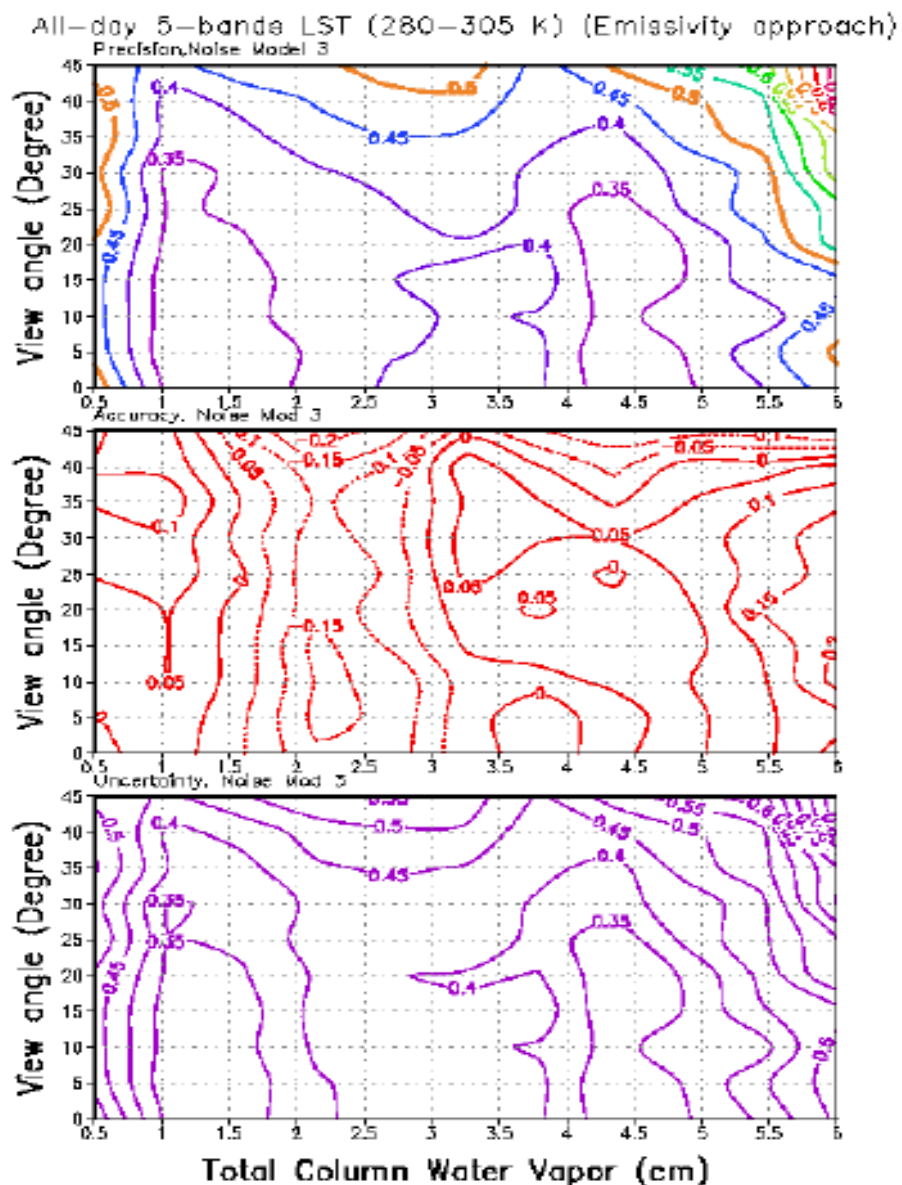


Figure 34. The LST precision, accuracy and uncertainty distribution with the TCWV and view angle by using the 5-band algorithm (emissivity approach).

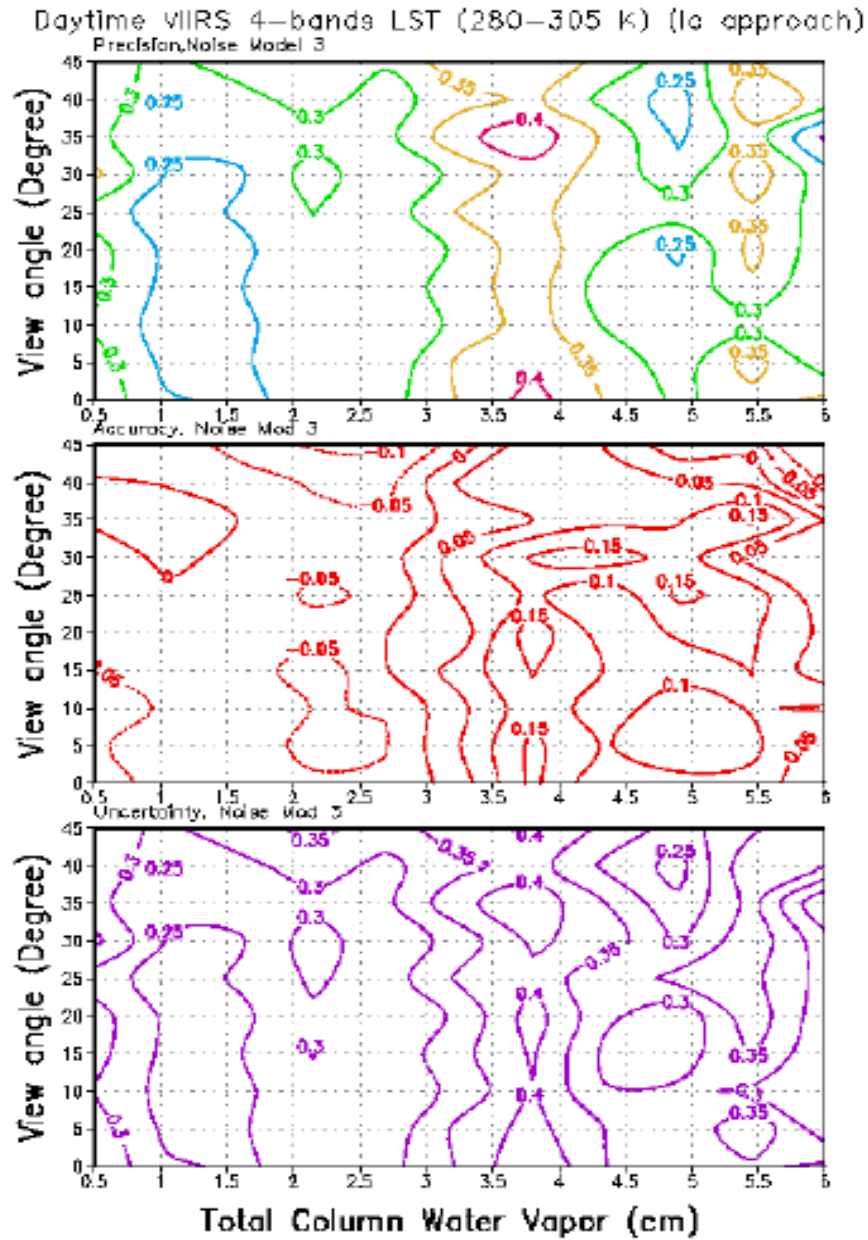


Figure 35. The LST precision, accuracy and uncertainty distribution with the TCWV and view angle by using the VIIRS 4-band algorithm (Land cover approach).

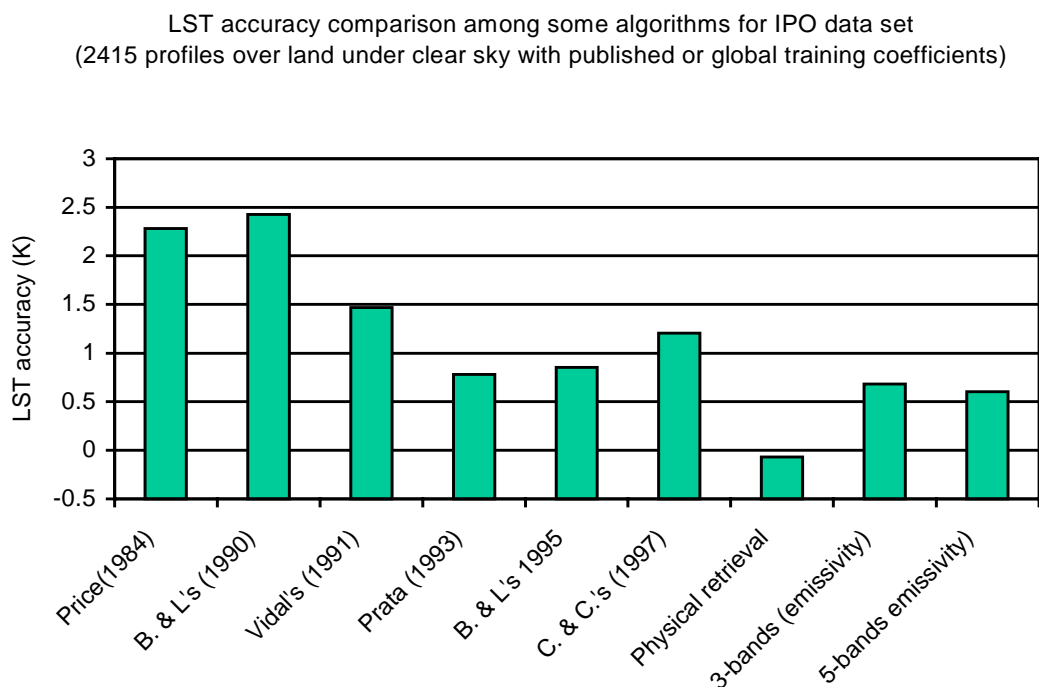
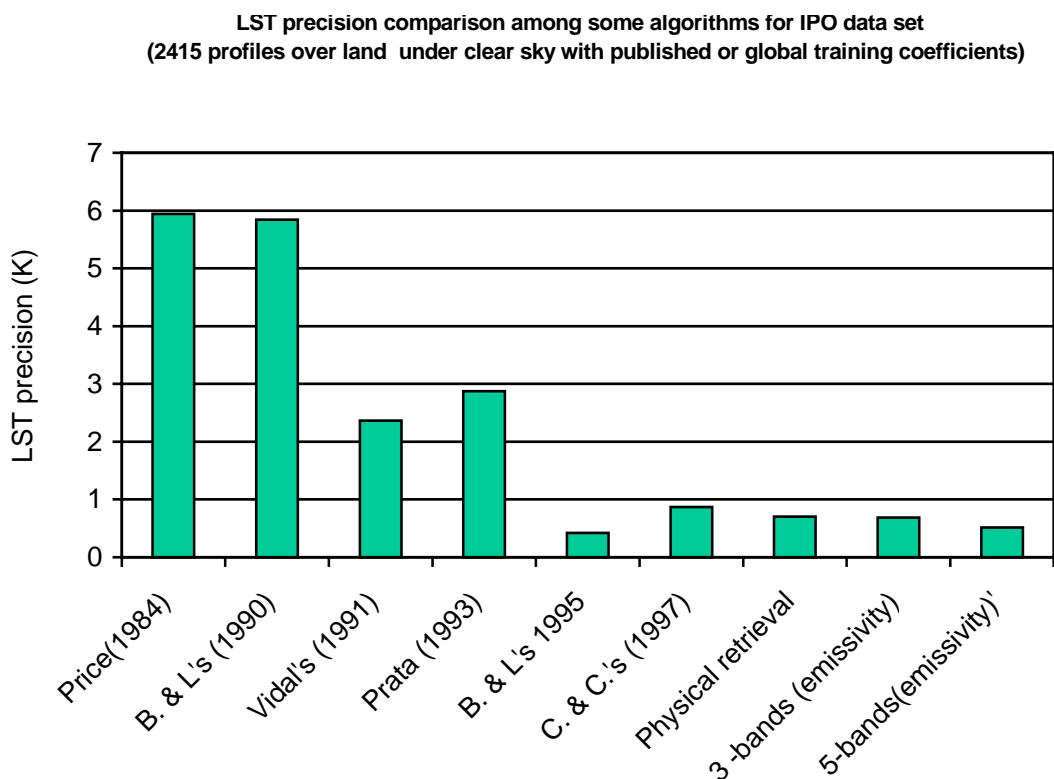
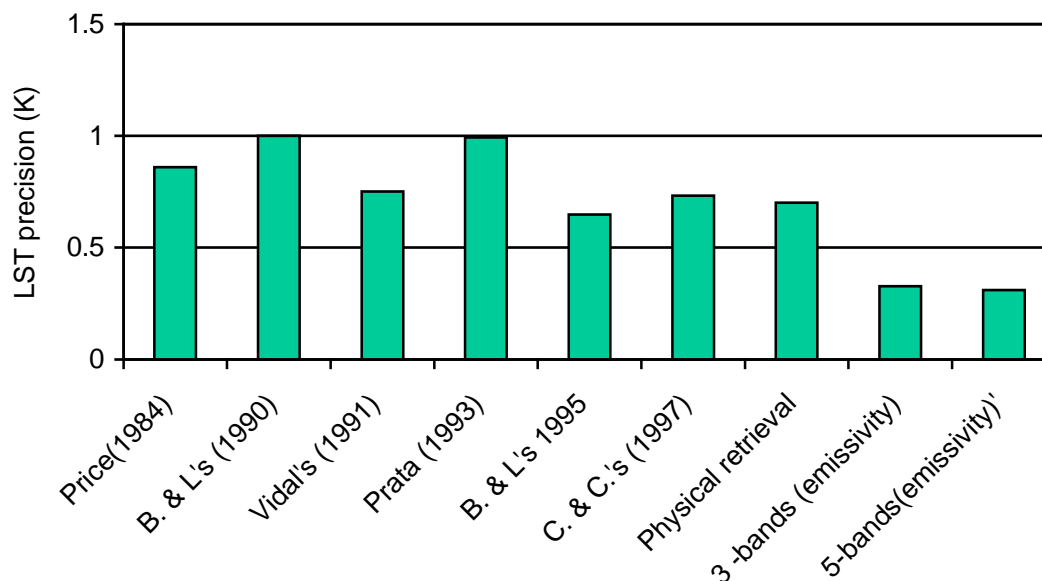


Figure 36. Comparison of different algorithms with IPO 2415 profiles over land under clear condition with the published coefficients or global training coefficients.

**LST precision comparison among some algorithms for IPO data set
(2415 profiles over land under clear sky with 30% data for training)**



**LST accuracy comparison among some algorithms for IPO data set
(2415 profiles over land under clear sky)**

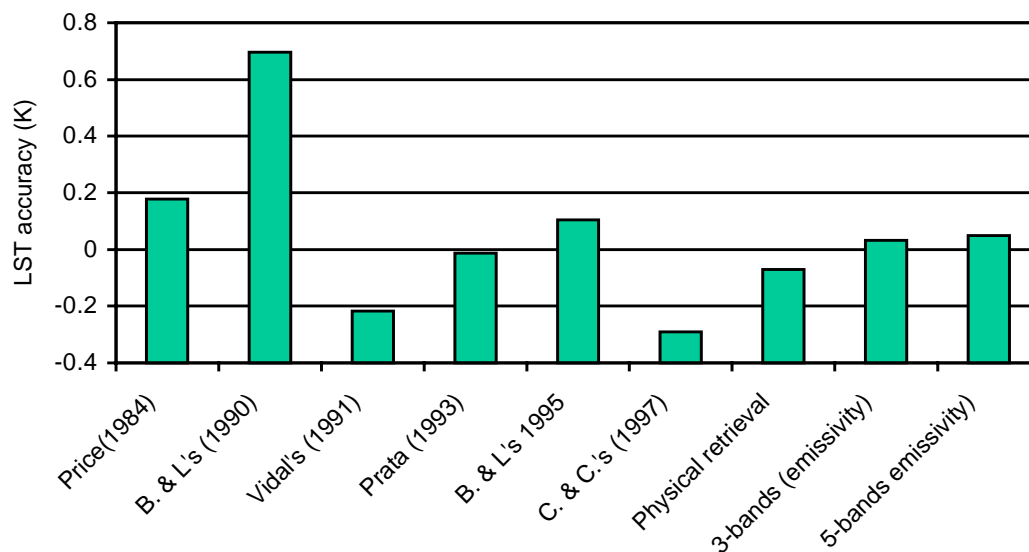


Figure 37. LST retrieval to the IPO 2415 profiles over land under clear condition with self-training coefficients. Precision for different algorithms (Upper panel). Accuracy for different algorithms (lower panel).

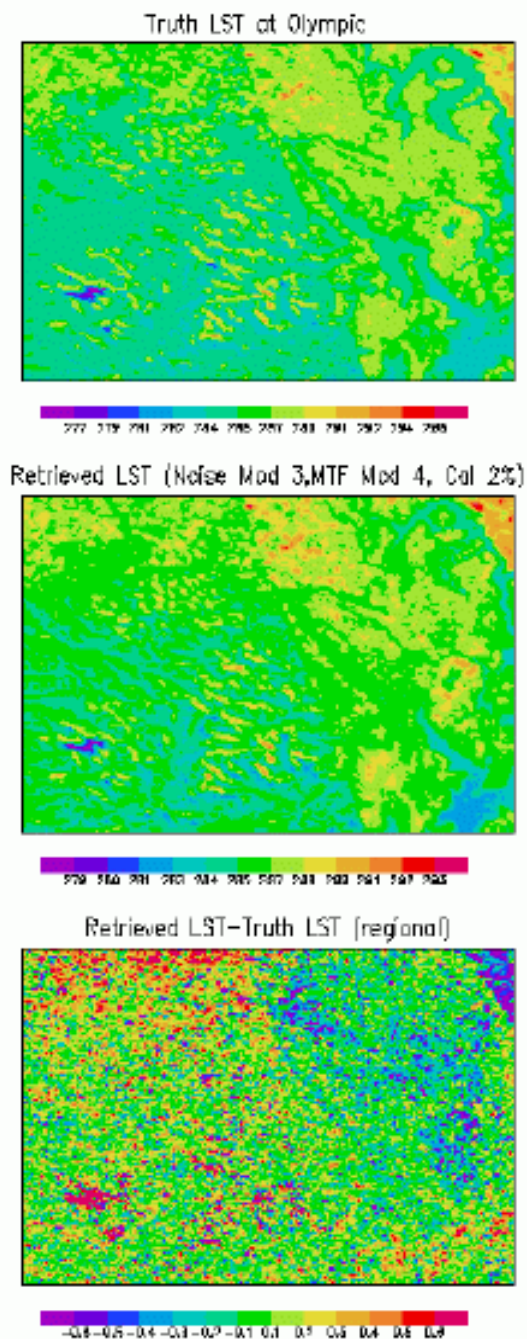


Figure 38. The upper panel is the truth LST of IPO Olympic scene. The middle panel is the retrieved LST with sensor noise model 3, MTF model 4 and calibration error 2% by using VIIRS new algorithm. The bottom panel is the bias of the retrieved LST to its truth-value.

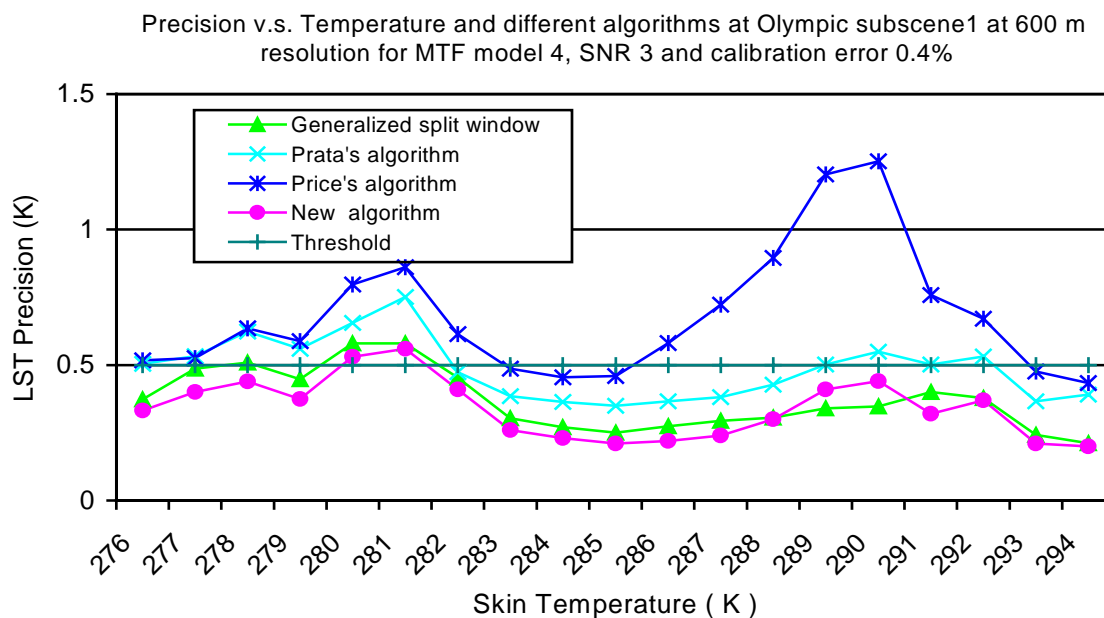
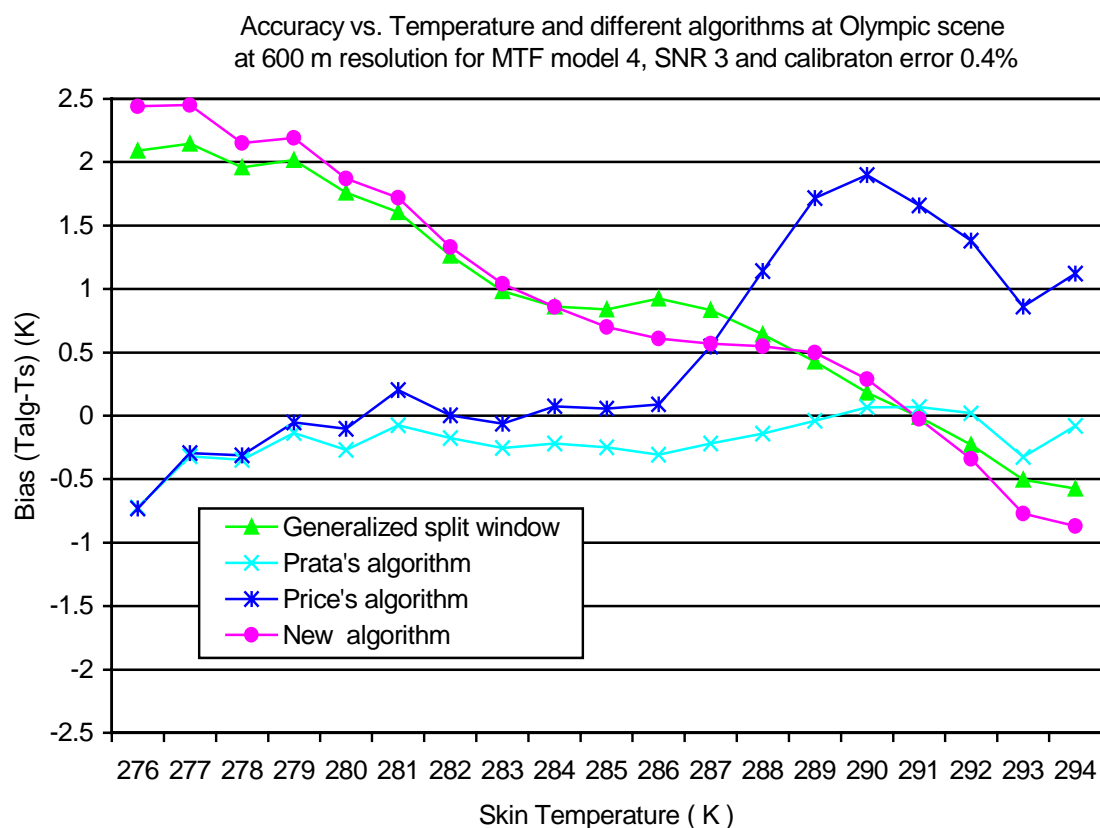


Figure 39. Upper panel: LST retrieval precision vs. the truth LST for different algorithms. Bottom panel: LST retrieval accuracy vs. temperature distribution.

3.3.8 Cloud contamination studies

The VIIRS LST algorithm is required to retrieve surface skin temperature only under clear sky conditions. Under actual conditions, it seems impossible for a whole scene to not have any clouds. We did some tests to some scenes contained cloud. IPO Bangladesh scene contains some clouds. Figure 20 shows our LST retrieval result to the Bangladesh cloud scene by using our new VIIRS algorithm. The upper panel is the truth LST for this scene, the middle panel is the retrieved LST, and the bottom panel shows the bias distribution between the retrieved LST and the truth LST. A greater error occurred at temperatures below 280K.

The retrieved LST precision distribution for different sensor models is shown in Figure 21. The precision cannot meet the threshold of 0.5 K below 280 K, even for sensor noise models 2 and 3. As shown above, the new algorithm cannot meet threshold for temperatures below 220 K for sensor noise model 3 cases. The temperature range for this scene is between 283–298 K. we checked the simulation input and found that the areas below 280K are cloudy pixels. This is a result of cloud contamination as the VIIRS LST precision requirement is only for clear sky conditions so clouds must be removed. There are several methods by which clouds can be removed. We can manually determine the cloud mask by comparing the visible image and the infrared image. Usually, clouds appear bright in the visible image due to their high reflectivity, while they appear dark in the infrared image because of cold brightness temperature at the cloud top. Other methods used to check the cloud mask include using some thresholds developed by VIIRS and MODIS cloud mask EDRs. As shown in Figure 22, without moving the clouds, the precision is unable to meet the threshold for sensor noise model 2 and 3 with a 2% calibration error. After partly removing some of the clouds, the precision improved. If a threshold of (Tb11-Tb12) is greater than 3.0K, it is most likely a cloud pixel. If a pixel is determined to be a cloud, then no statistics were performed on this pixel. This threshold, however, cannot remove all clouds.

LST retrieval under cloudy conditions is not required for VIIRS, because visible and infrared measurements can't provide useful information of land surface properties. Retrieving LST under cloudy conditions is a challenge. With the physical retrieval approach we previously discussed, we can retrieve LST under both clear and cloudy conditions. Figure 23 shows the results from retrieving 2,450 profiles under cloudy conditions. The Marquardt-Levenberg retrieval algorithm was used to resolve the linearized radiative transfer equation. While surface skin temperature is derived, atmospheric profiles (temperature, water vapor, ozone), surface emissivities and reflectance at seven window channels, cloud top pressure and cloud fraction at two cloud layers were derived at the same time. IPO atmospheric profiles had 66 levels, resulting in a total of 217 parameters that need to be resolved ($1+66 \times 3 + 7 \times 2 + 2 \times 2$). The 230 CrIS vertical sounding channels were used to obtain atmospheric profile information, and seven window channels were used to derive surface properties. Singular value decomposition methods with 200 eigenvectors were used to give the first guess field. As shown in Figure 23, we can achieve 0.09K accuracy and 1.322 K precision for surface skin temperature retrieval—a very exciting result.

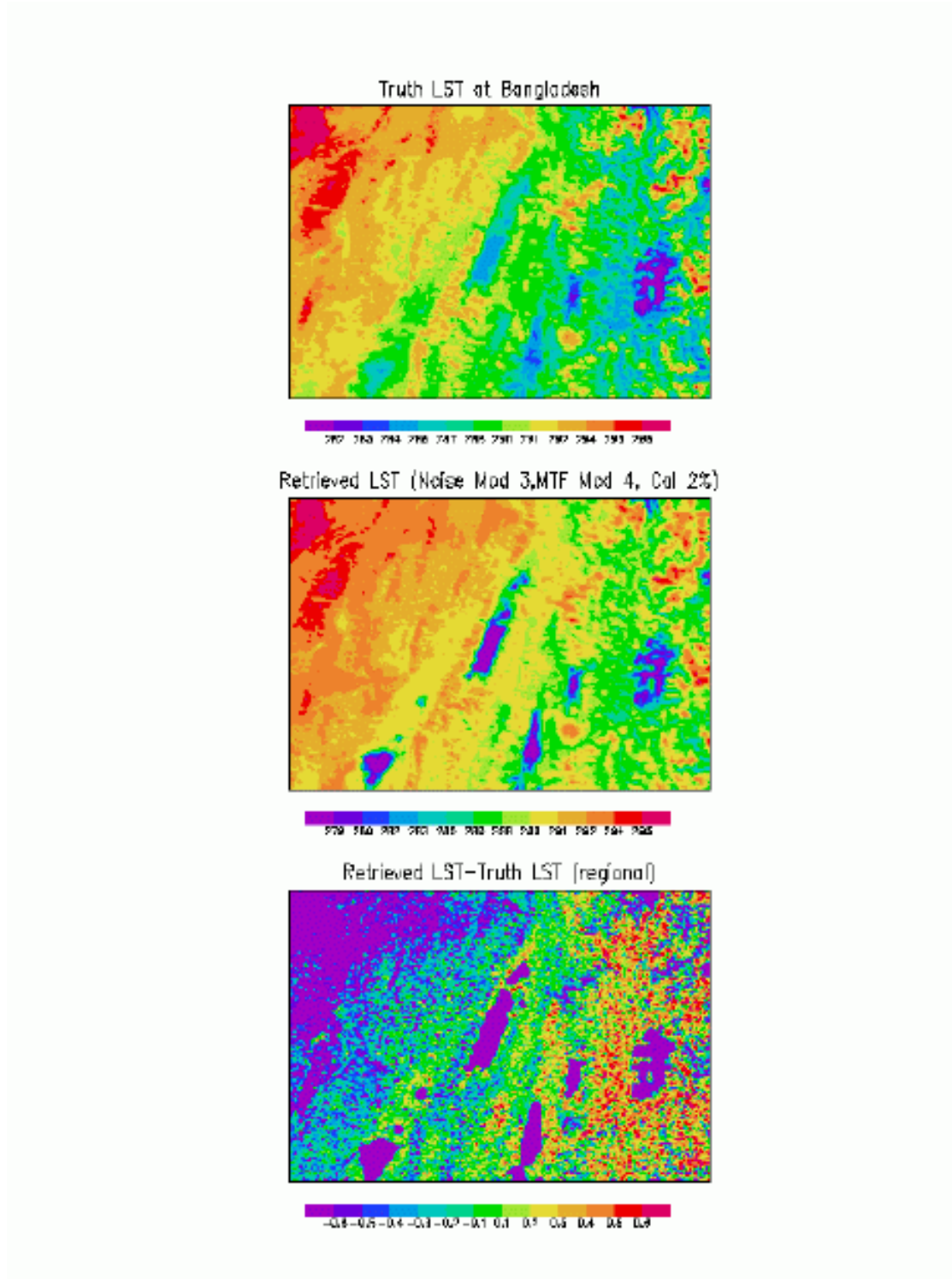


Figure 40. a) Bangladesh truth LST; b) the retrieved LST; c) the bias distribution between the retrieved LST and the truth LST.

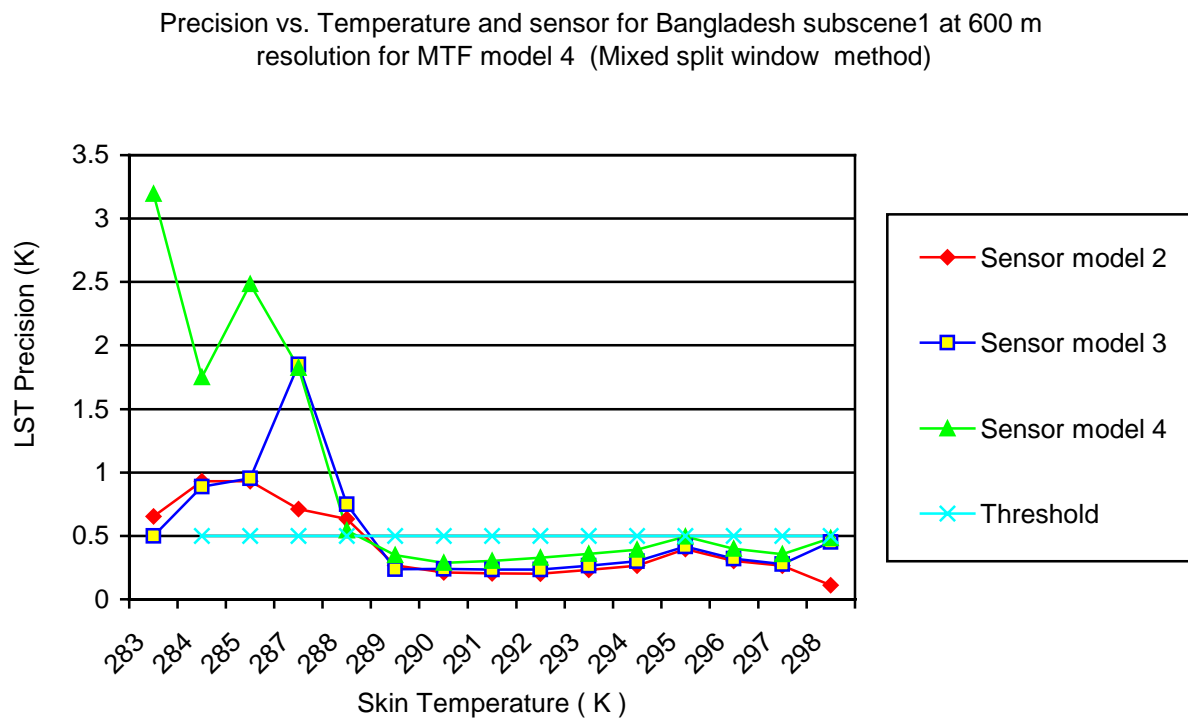


Figure 41. Retrieved LST precision vs. temperature for different sensor noise models.

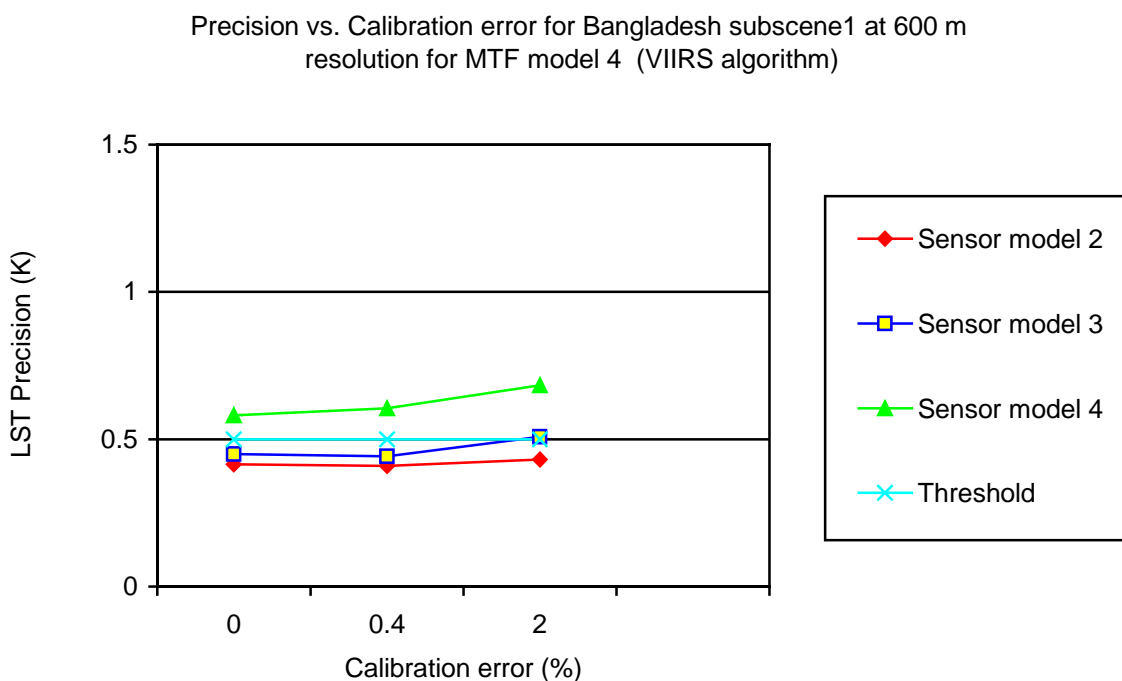
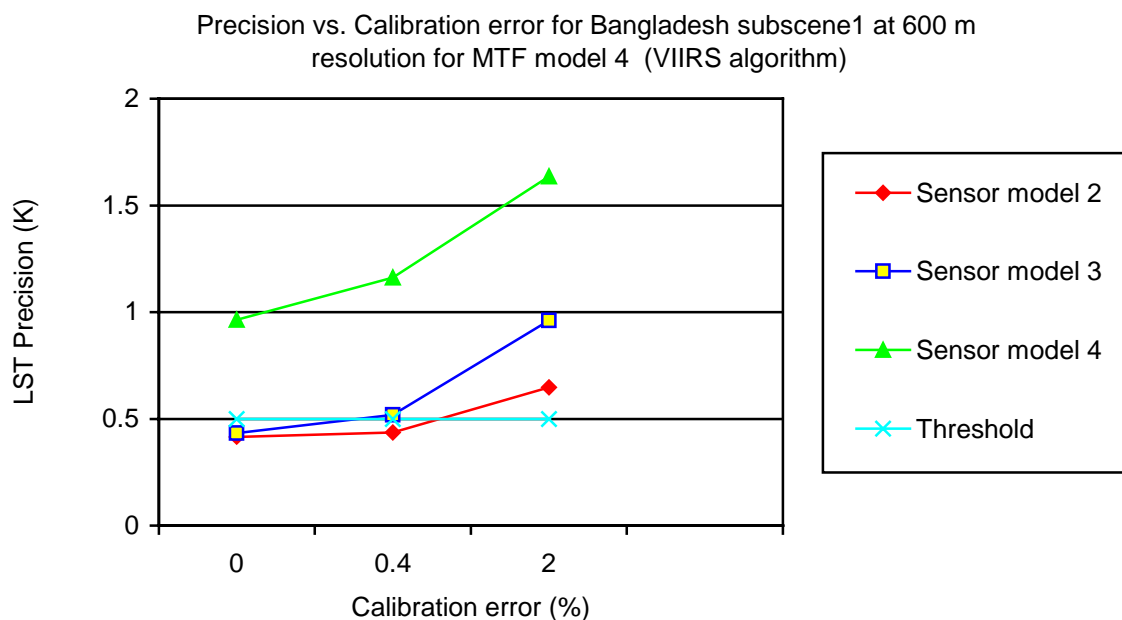


Figure 42. (a) Retrieved LST precision vs. sensor noise model and calibration error without removing clouds. (b) Same as (a), but clouds was partly removed.

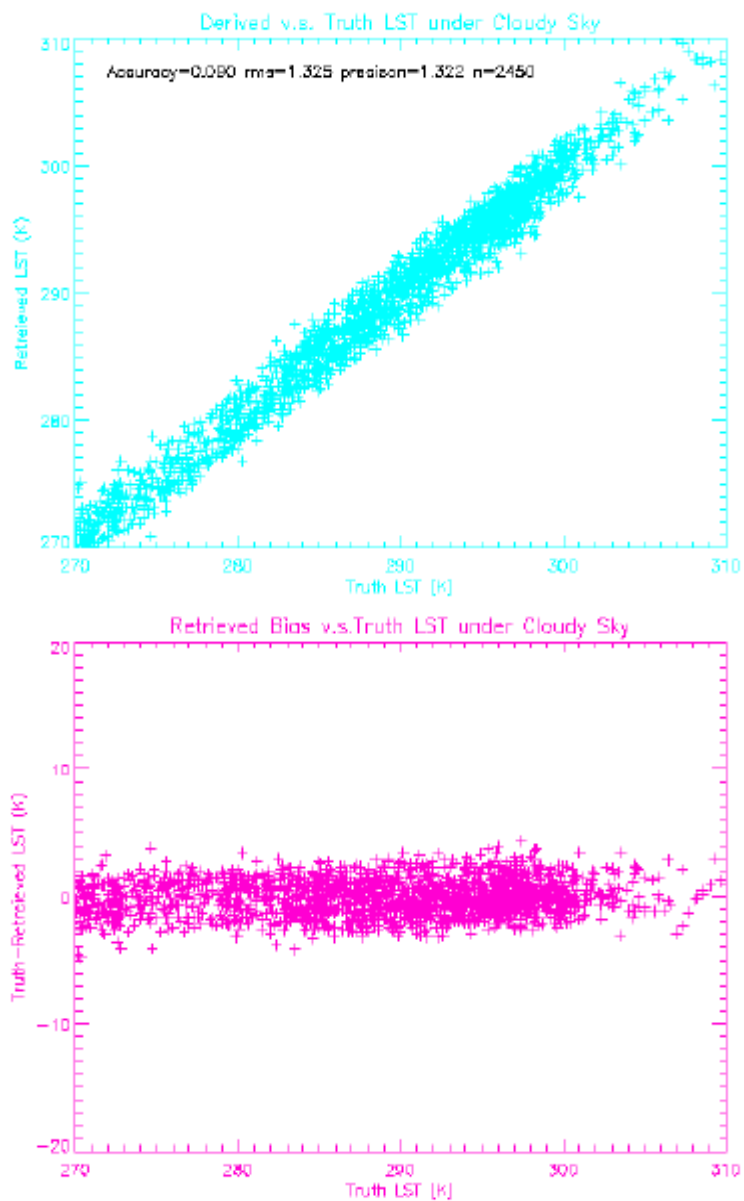


Figure 43. Physical retrieval to the IPO 2450 profiles under cloudy condition. (a) Retrieved LST vs. truth LST scatter plot. (b) Bias vs. truth LST scatter plot.

3.3.9 Validation problem

All of the tests above were performed based on simulation data, i.e., the truth LST was supposed to be known. For real-time data, the validation of global LST retrievals from satellite measurements is problematic since satellites measure skin temperature while ground truths provided by the global observational system are shelter temperatures. Although skin LSTs from a few field sites – such as the First International Satellite Land Surface Climatology Project (ISLSCP) Field Experiment (FIFE) – are now available (Prata, 1994; Wan and Snyder, 1996), they are not globally representative. Prata (1994) and many others have addressed the difficulty of obtaining ground truth LST. *In situ* LSTs can be measured with contact thermometers, as well as thermal infrared spectrometers. The contact thermometers measure an LST at a point, while the satellites measure the mean LST over a pixel area. The LST may vary significantly within a pixel area, and therefore, a single pixel area may require the use of a number of thermometers.

In reality, both spatial and time variability of land surface temperatures is greater than that of sea surface temperature. This made the validation of LST retrieval from satellite data more difficult than with SST validation. The only ground truth we can use is the shelter temperature. Fuzhong Weng and Norman C. Grody (Weng and Grody, 1998) tried to use shelter temperature in the early morning to validate LST retrieval from satellite SSM/I data. They found that the difference between surface skin temperature and shelter temperature is lowest at early morning. This validation, however, is limited to early morning. From their experiment, we determined that, if we can find a relationship between surface skin temperature and the shelter temperature, we can convert the shelter temperature to surface skin temperature to validate LST retrieval from satellite, thus permitting us to take advantage of the global observation system of shelter temperature. To facilitate the process, a land surface model SSIB (Simplified Simple Biosphere) was coupled to a regional ETA model, which was then used to derive skin temperature from the shelter air temperature.

One experiment was performed to retrieve LST from the NOAA/NASA pathfinder AVHRR global land data set at 8-km resolution from 10 to 20 of July 1992. This data set contains a 10-day composite of AVHRR channels 1, 2, 4, and 5 and the Normalized Difference Vegetation Index at 8-km resolution under clear conditions. Currently, it covers the period from 1982 to 1994. To get the surface emissivity information, land type data from the University of Maryland in July 1992 1 km land cover data, aggregated to 8 km resolution by VIIRS simulation team, was used to obtain the surface emissivities from our spectral database. Figure 24 shows this global land cover map. The surface type indexes are as follows: (1) Evergreen needle forest; (2) Evergreen broadleaf forest; (3) Deciduous needle forest; (4) Deciduous broadleaf forest; (5) Mixed forest; (6) Woody savannas; (7) Savannas; (8) Grasslands; (9) Closed shrub lands; (10) Open shrub lands; (11) Swamp; (12) Marsh/Bog; (13) Tundra; (14) Croplands; (15) Urban; (16) Bare; (17) Permanent snow and ice; (18) Water; and (19) Islands. The retrieved global LST at 8 km resolution (Figure 25), is a data set that only had two thermal window channels (10.8 and 12 μm as channel 4 and 5), and a split window algorithm was employed here. The split window algorithm coefficients came from the MODTRAN simulation of the NCEP global data set at 2.5X2.5° resolution. The retrieved LST shows the surface properties' basic feature. However, the retrieval validation is difficult because the only available *in situ* observation data are shelter temperatures. The shelter temperature over the United States during July 10 through 20, 1992

was obtained from the NCAR. The validation test was performed over the U.S. However, the difference between the surface skin temperature and shelter can be from -4 K to 16 K during daytime and -16 K to 4 K during nighttime (Wan and Snyder, 1996). The mean difference between the retrieved LST and the observed shelter temperature in this experiment is 4.0 K. In order to find the relationship between the surface air temperature and skin LST, a land/atmosphere-coupled model (ETA/Sib) was used. The ETA coupled Sib model system, adopted from the NCEP operational ETA weather forecast model, has four layers from the surface through a soil layer 1 m deep and 50 layers in the atmosphere (Ji and Veneker, 1997). The model includes a complete radiation transfer model and a simplified biosphere model. Figure 26 exhibits the simulated difference between skin LST and surface air temperature. The skin LST is warmer than surface air temperatures during daytime and colder than air temperatures during nighttime for most land types. The difference between T_s and T_{air} from model calculation ranges from -2 K to 20 K at daytime and -10 K to 4 K at nighttime for various land surface types over North America. The daytime mean difference between T_s and T_{air} is 3.9 K. These results are slightly different from those described by Wan and Snyder (1996). The relationship between T_s and T_{air} was established by a linear regression between input T_{air} , AVHRR channel 4 emissivity $em4$ and channel 5's emissivity $em5$ and model generated T_s as:

$$T_s = b_0 + b_1 T_{air} \quad (37)$$

The model error is estimated about $1\sim 2$ K. The mean difference between the retrieved skin LST and the model generated skin LST is only 0.31 K. This indicates the model-generated LST is reliable and more realistic.

Another validation problem is the time. The global pathfinder land data is a 10-day composite. The number of *in situ* observations that match the satellite measurement in both time and space is only two. The *in situ* LST was not observed at the exact time when the satellite passed. Figure 27 shows the LST scatter plot with a one-hour time difference. The RMS error is 3.99 K. In this figure the difference between times when data were collected and when the satellite passed is less than one hour.

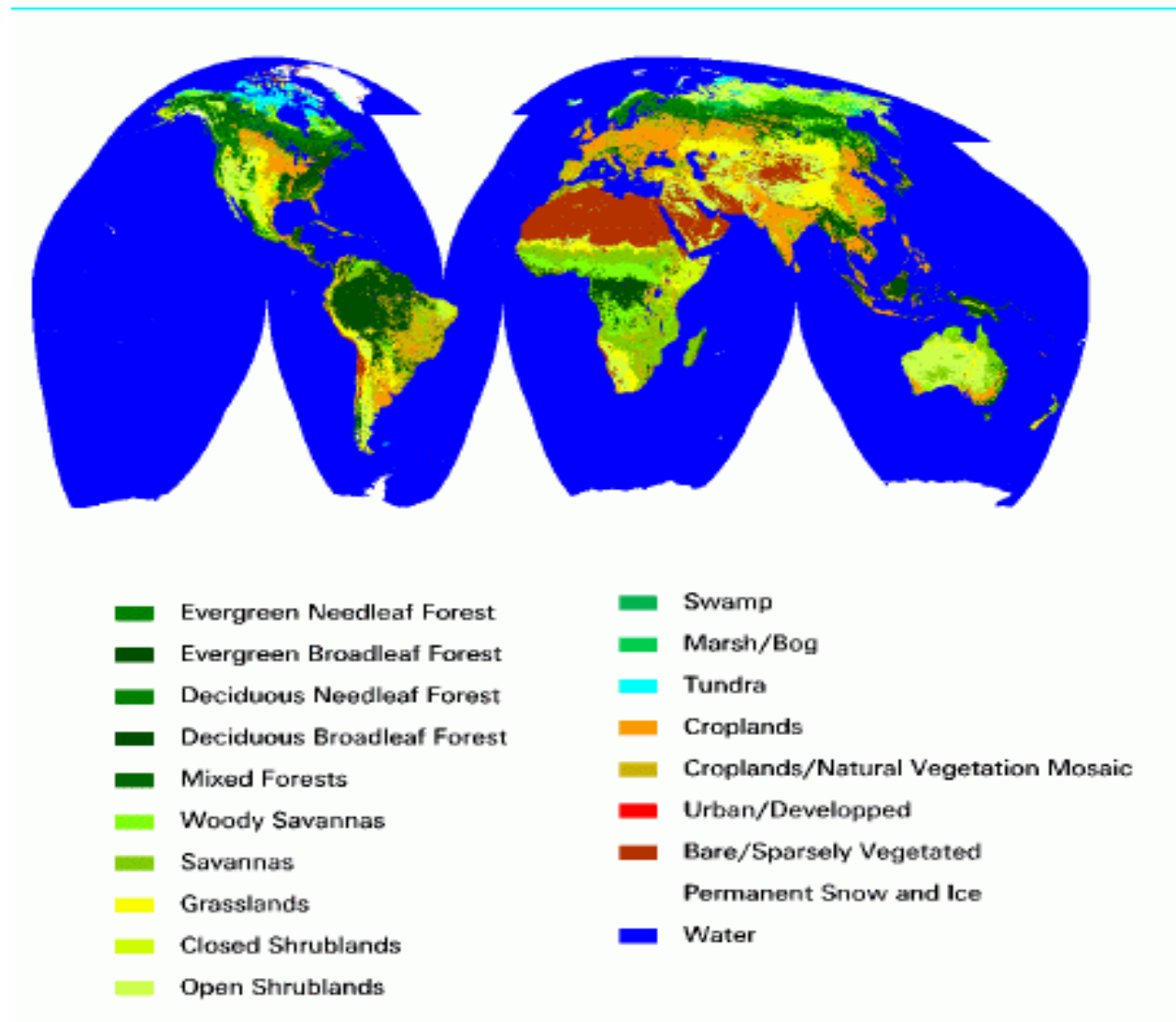


Figure 44. Global land covers at 8-km resolution during July 1992.

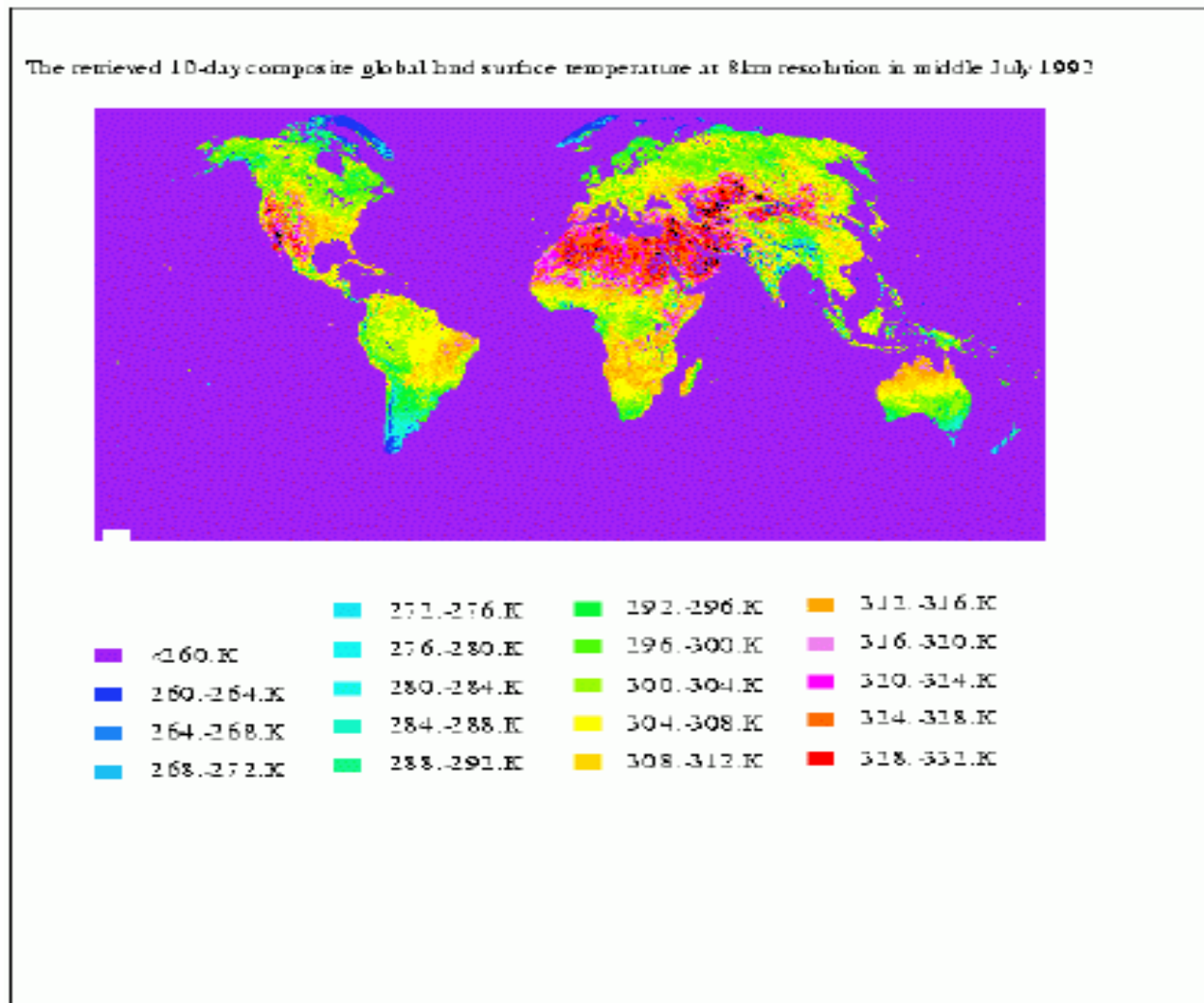


Figure 45. Global LST retrieval at 8-km resolution during July 1992.

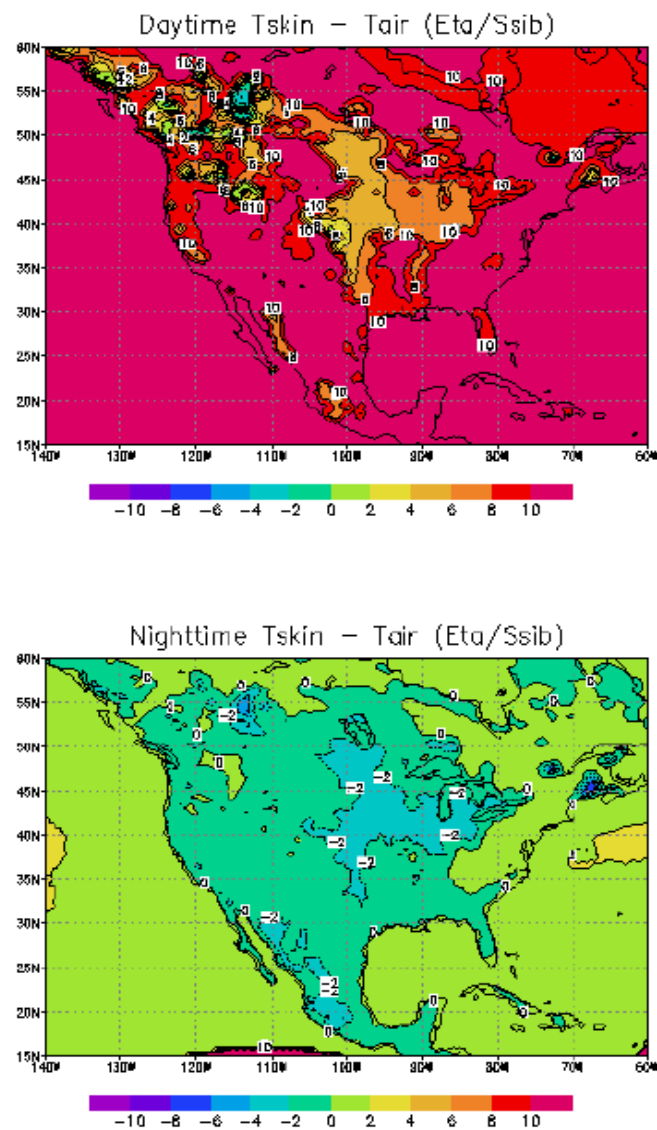


Figure 46. Difference between skin LST and surface air temperature from the model simulation. Upper panel: During daytime period. Lower panel: During nighttime period.

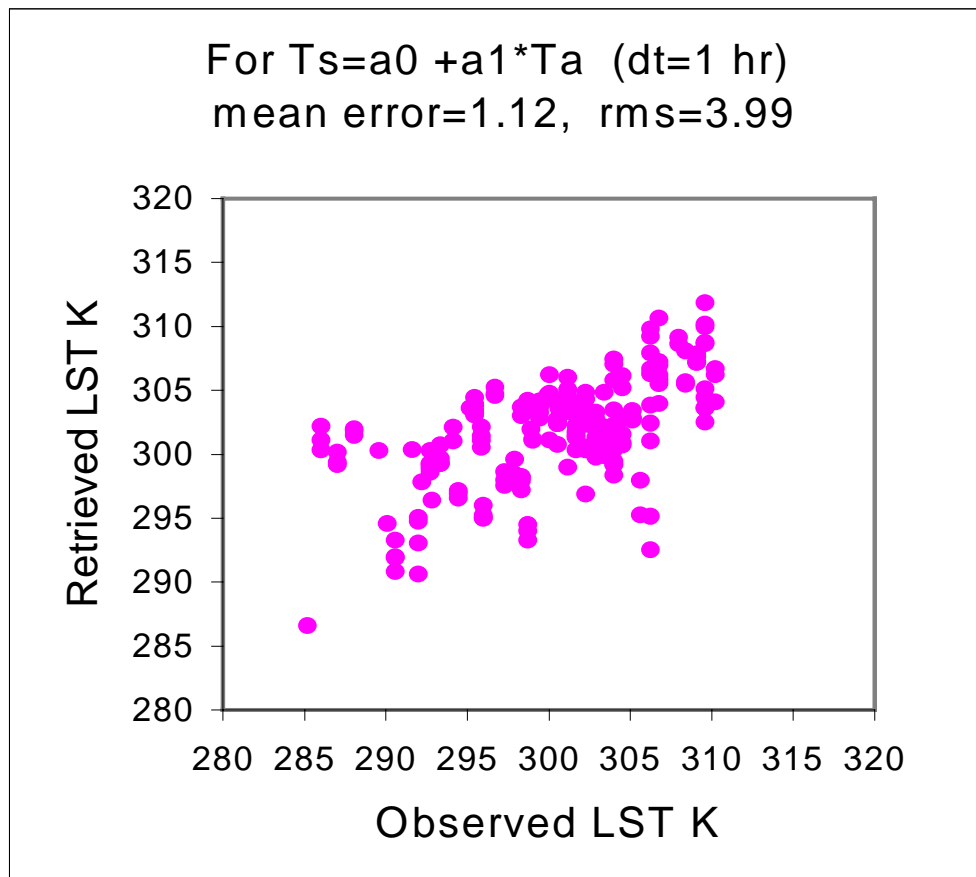


Figure 47. Scatter plot of LST values. The time difference between the satellite pass and the ground measurement is less than one hour.

3.4 ALGORITHM SENSITIVITY STUDIES

3.4.1 Calibration Errors

In order to investigate the algorithm accuracy requirement relevant to the mean radiometric error in the sensor, we added the mean of errors to the simulated radiance and performed retrievals. Figure 28 shows the accuracy change with the mean error added to the radiance for each band. The data is a global observation. To be accurate at 2.5 K, the calibration error for the 11 and 12-micrometer bands needs to be less than 1 percent. However, due to the nature of the statistical regression method, the absolute calibration error (about 1 percent) may be eliminated by post-launch validation processes.

Split Window LST Accuracy vs. Calibration Errors

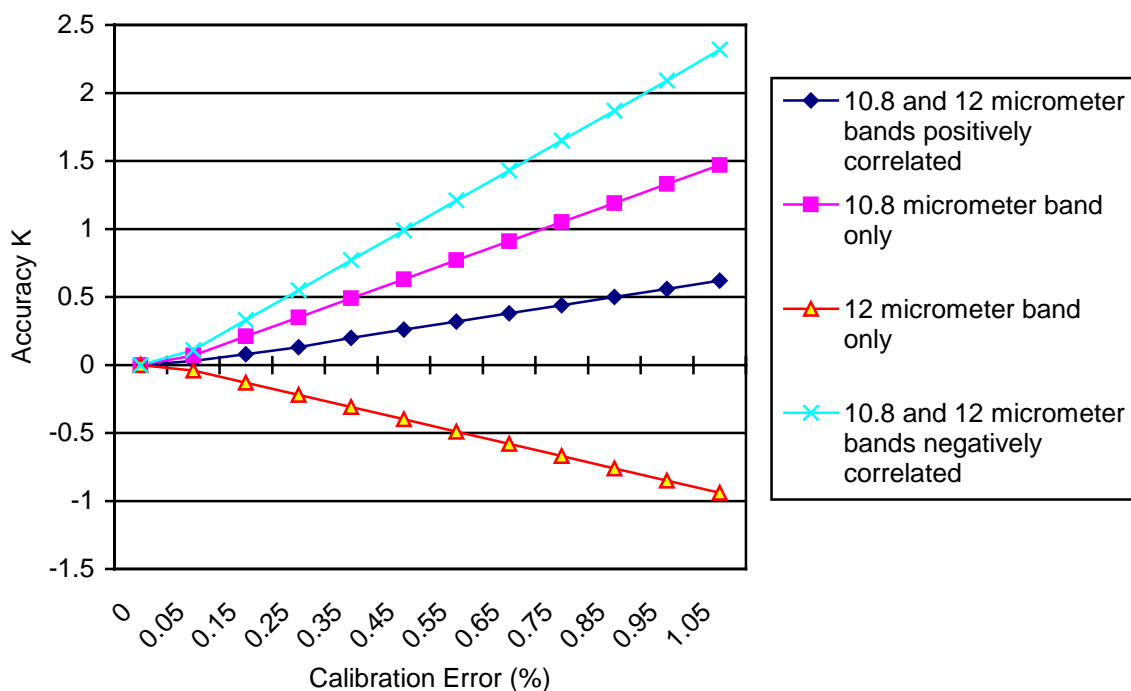


Figure 48. Split window LST accuracy relevant to calibration error.

Calibration error has no effect to LST precision, as shown in Figure 29. LST precision does not change with the calibration error. VIIRS new algorithm gave the best precision, while Price's algorithm showed the worst precision. LST accuracy from VIIRS algorithms increased significantly with the calibration error (Figure 29). To meet the threshold, the calibration error required should be less than 2%.

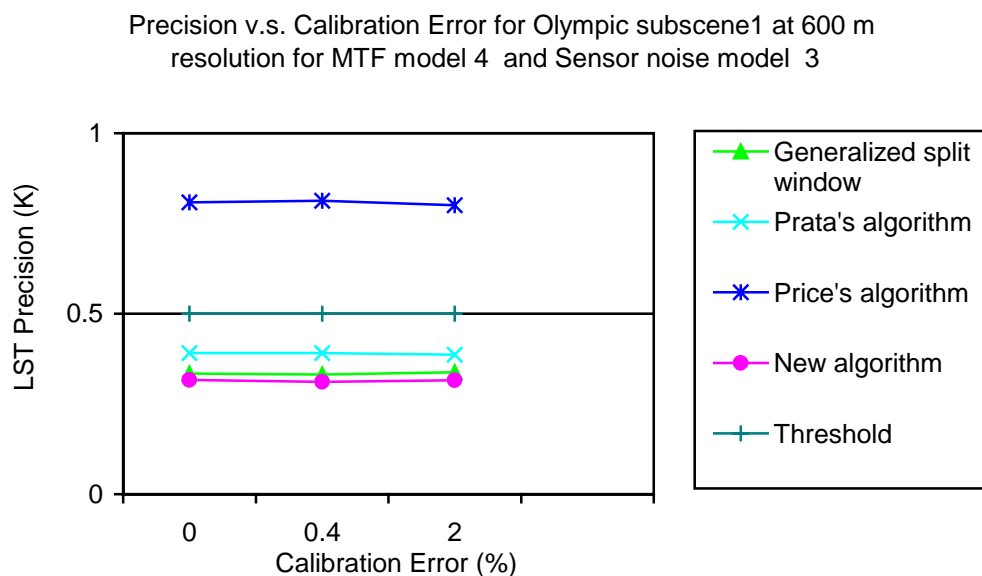


Figure 49a. LST precision vs. Calibration error for different algorithms.

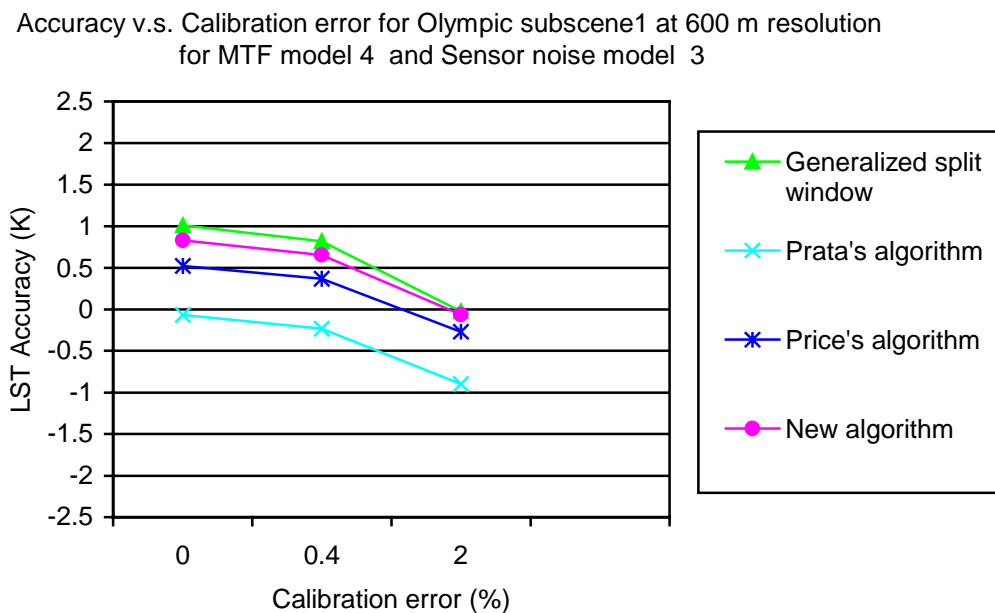
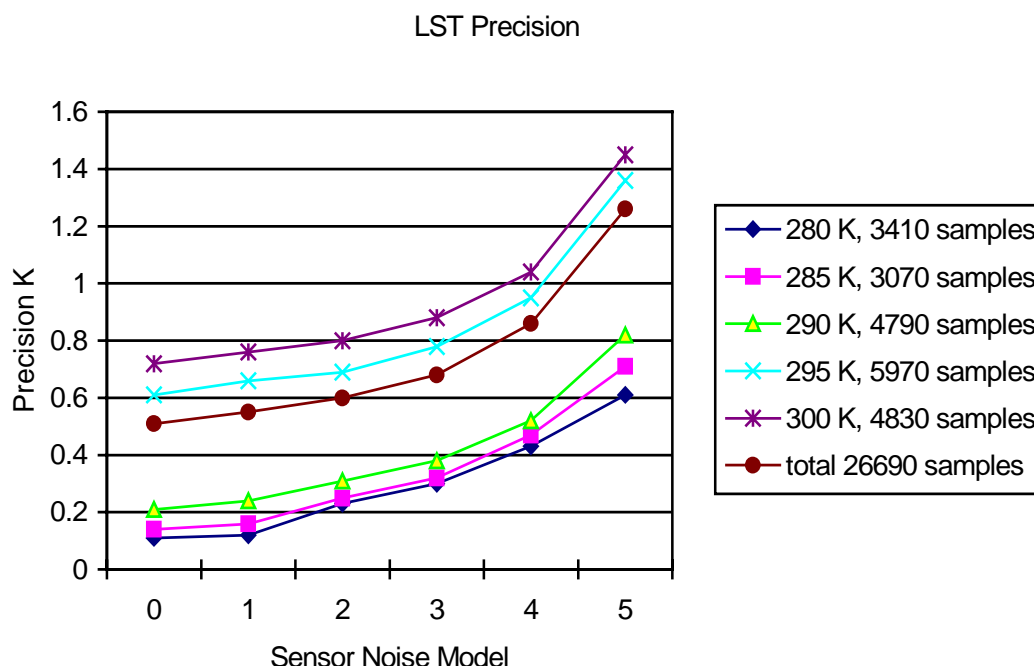


Figure 49b. LST accuracy vs. calibration error for different algorithms.

3.4.2 Instrument Noise

Figure 30 shows the precision changes with the sensor noise model when the data are stratified by 5 K intervals for the NCEP global data set by using split window algorithm. The results show that the precision changes are similar for all categories except within the 300 K category. In the split-window algorithm, the precision error is less than 0.5 K only for categories with temperatures less than 290 K and for sensor noise model 3. For warmer temperature above 290K, the precision cannot meet the threshold 0.5K. The total precision cannot meet the threshold after sensor model 3. Three error sources contribute to the algorithm precision. They are surface emissivity, atmospheric correction, and sensor performance. The error due to atmospheric correction is about 0.4 K due to emissivity, which is about 0.5 K. The error due to sensor noise is about 0.15 K at sensor model 3, and about 0.2 K at model 4. Assuming that the total error is the Root Sum Square (RSS) of the three, the total precision will be the error that is dominated by the emissivity contribution and the atmospheric correction for sensor noise model 1-4 in the split-window algorithm.



**Figure 50. LST precision at eight categories from split window.
The temperature interval is 5K.**

Figure 31 is similar to Figure 30, but for accuracy only. It is clear that the mean error for the whole data set does not have statistical meaning if there is no calibration error added. However, when the data are stratified into small categories, the mean error becomes much larger for some categories as the sensor noise increases. As we can see, below 290 K, the split window overestimated LST, while for warmer temperature above 290 K, the split window underestimated LST. But the total accuracy can meet the threshold for all sensor noise models. In this case, all sensor noise models can meet the accuracy threshold requirement (2.5 K).

In this simulation, the error in surface emissivity has not been considered. The accuracy may be significantly influenced by the error in surface emissivity.

Figure 32 shows the precision from triple window calculations. The third band is a suggested band centered at 8.55 micrometer. The NEDT for this band is 0.05 K. It shows that the precision is improved for all categories, especially those having warmer temperatures. It seems that this band has a large influence in decreasing the error in the emissivity correction.

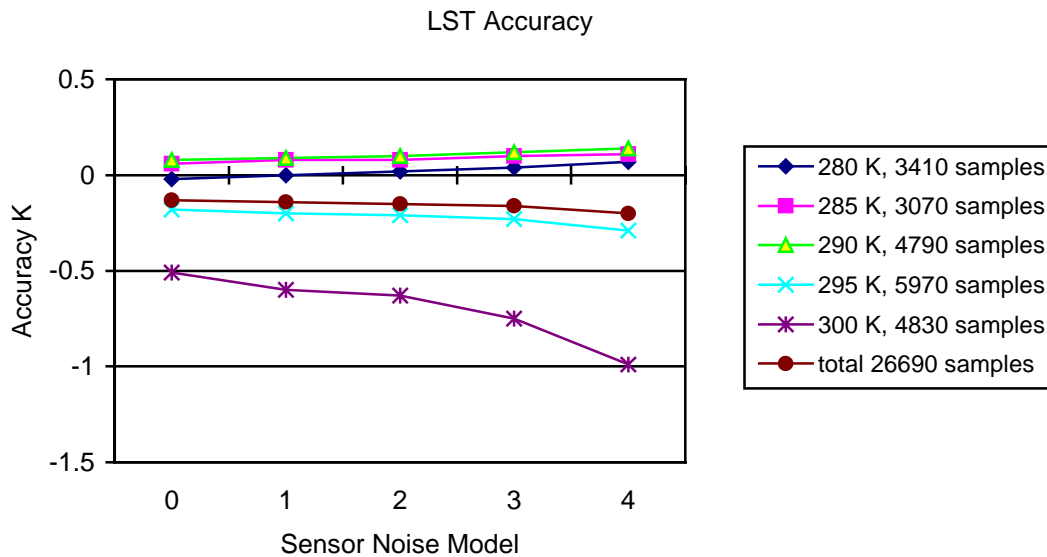


Figure 51. LST accuracy vs. Sensor Noise Model from split window.

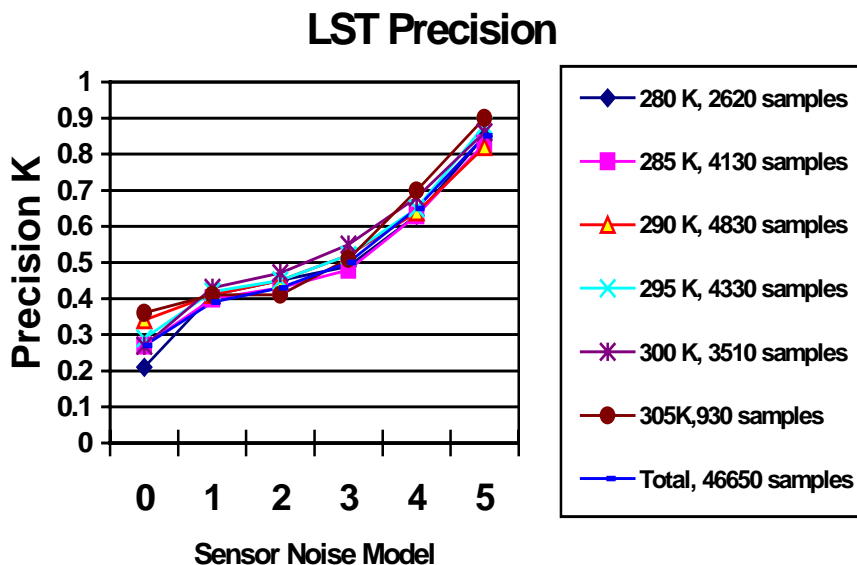


Figure 52. LST precision from VIIRS-4 band (3.75, 4.005, 10.8, and 12 μm) day/night algorithm.

3.4.3 Band-to-Band Registration

LST precision is related to band-to-band registration, as shown in Figure 33, with the NCEP global data set by shifting 12- μm band and using split window algorithm. A misregistration of 20 percent may introduce an error of about 0.3 K in the noise-free case, and 0.2 K for noise model 3. This suggests that band registration error have a larger influence on noise-free data than on noisy data. Because the total precision requirement is 0.5 K, it is recommended that the misregistration between two bands be less than 20 percent.

Figure 33 shows the influence of band-to-band registration to the algorithm's precision. The misregistration has significant impact on the retrieval precision when the noise level is lower. When the sensor noise becomes larger, the influence of band-to-band registration becomes less important.

Figure 34 shows another example of tests band-to-band registration's effect to LST precision. It works with the IPO Olympic scene. As shown in Figure 17, the temperature values for this scene are below 294 K, split window algorithms can also get good results. So, for simplification, split window algorithm was used to test LST precision sensitivity to band-to-band registration error. By shifting 11 μm and 12 μm respectively and then the total precision is calculated due to the misregistration error. The result is shown as Figure 34, the LST precision (error) increases with the band-to-band misregistration error. In order to meet the threshold requirement 0.5K, the misregistration error should be less than 20%.

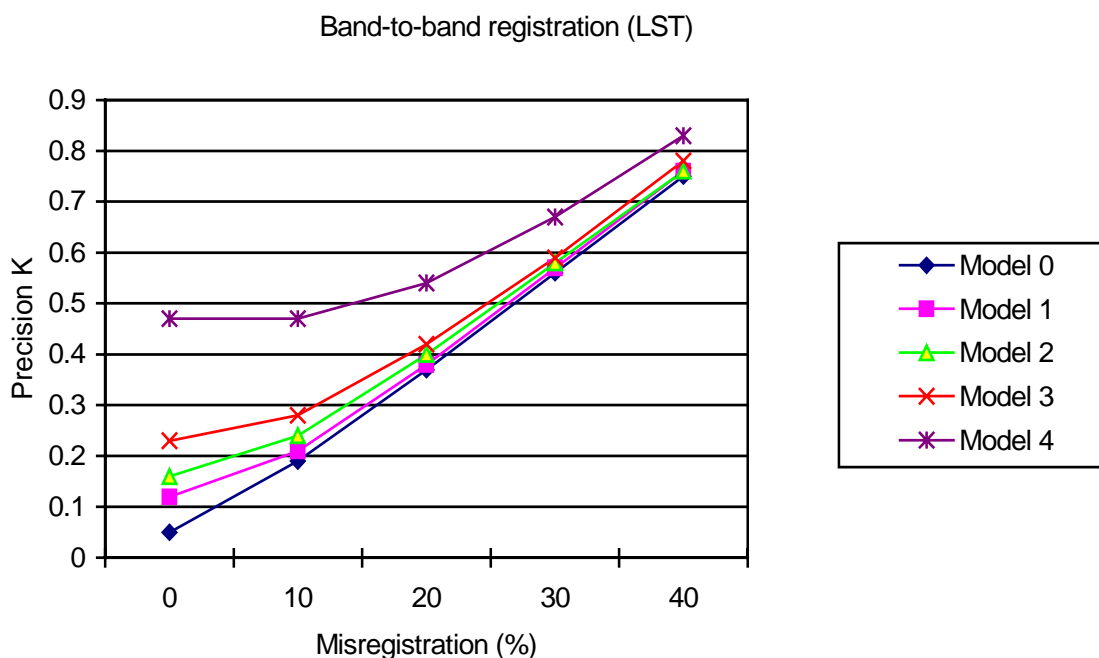


Figure 53. The influence of band-to-band registration on LST retrieval precision.

LST precision vs. Band-to-band misregistration

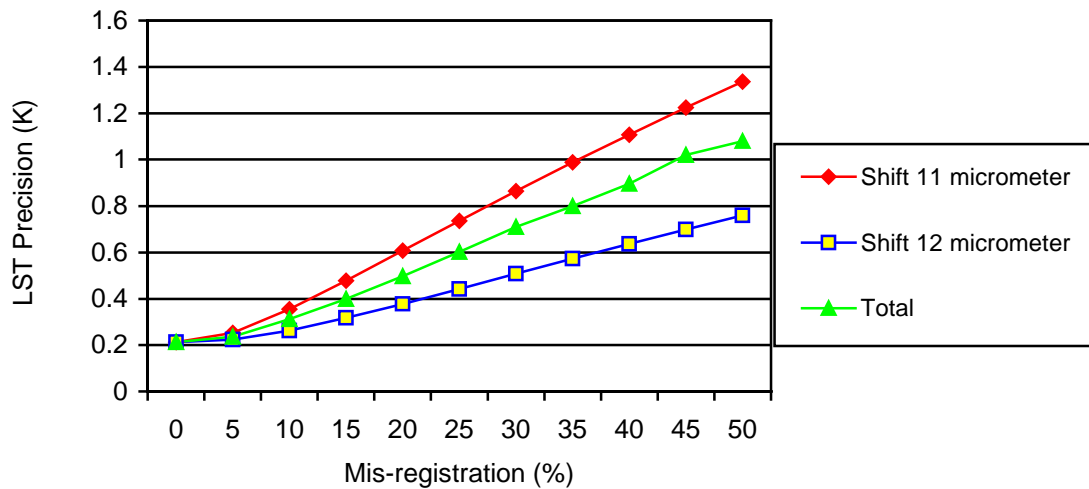


Figure 54. LST precision vs. band-to-band registration error for IPO 50m Olympic land scene with no sensor noise, no calibration error and no MTF effect aggregated to 1km and compared with the ground truth LST by using split window algorithm.

3.4.4 Geolocation error or mapping uncertainty

LST precision vs. geolocation error

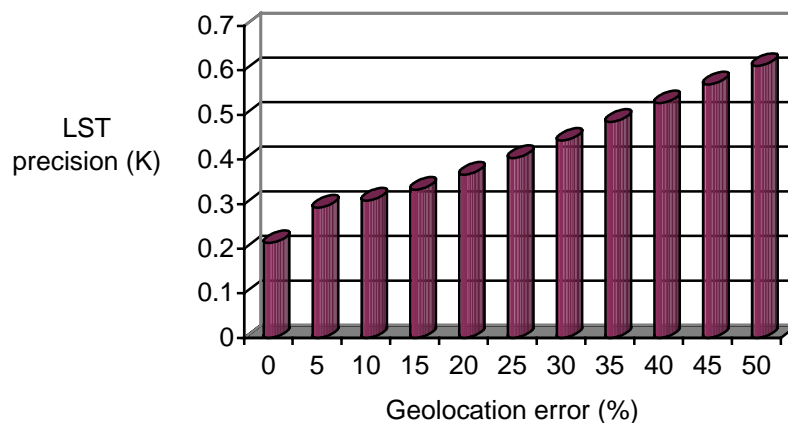


Figure 55. LST precision vs. geolocation error

LST precision changes with the geolocation error see Figure 35. LST precision increases with the geolocation error, in order to meet the precision threshold requirement 0.5K; geolocation error should be less than 40%.

Geolocation error has no effect on the LST accuracy.

3.4.5 MTF effect

Modulation Transfer Function (MTF) is a very important concept with satellite remote sensing. A pixel with Ground Sampling Distance (GSD) may consist of many footprints or Geometric Instantaneous Field of View (GIOV). Spatial Response Function (PSF) is used as a kind of weighting function to aggregate GIOV to GSD. Different PSF forms can be used with requirements to satisfy that it should be equal 1 when the distance between the center of a pixel and footprint is zero and then it decreases with this distance. 7 MTF models with MTF values of 0.7 to 0.1 at Nyquist to control the rate of PSF decrease with the distance between the footprint and the pixel center.

LST retrieval precision vs. GSD and MTF model 4 and 7, shown as Figure 36. We can see the LST precision increase with GSD increase. MTF model 4 can achieve better precision than MTF model 7. To meet the LST retrieval precision threshold 0.5 K, MTF model should be better than model 7.

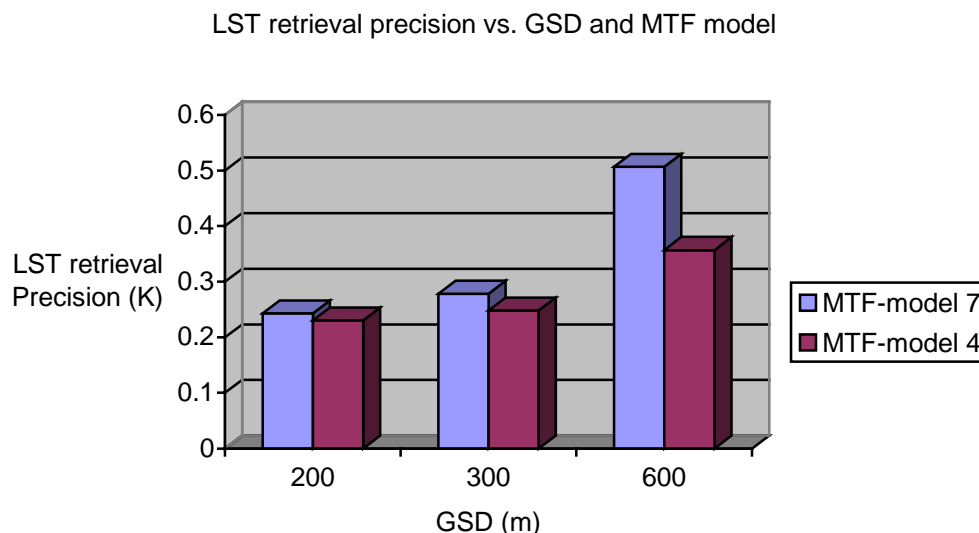


Figure 56. LST retrieval precision vs. GSD for MTF model 4 and 7.

3.4.6 Emissivity

Errors in emissivity have a strong effect on the LST retrieval by using those algorithms that depend on surface emissivity. Figure 37 shows the LST precision error vs. temperature distribution for generalized split window and new VIIRS-3 bands algorithm with 0.005-emissivity error.

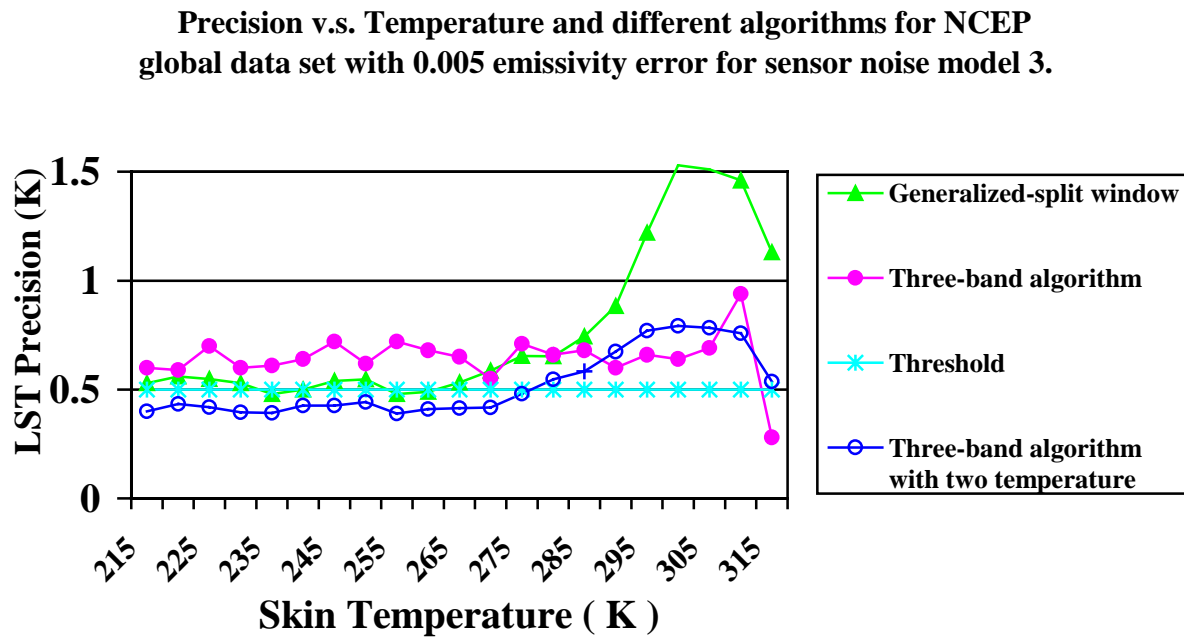


Figure 57. LST precisions vs. skin LST with 0.005 emissivity error.

As we can see from figure 37, for those algorithms which depend on surface emissivity, such as generalized split window and new VIIRS- 3 bands algorithm, even with 0.005 emissivity error, the LST retrieval precision can't meet the threshold for almost all temperature range, especially for warmer temperature.

3.4.7 Land Cover

Our baseline algorithm VIIRS-4 band algorithm depends on land surface types. The VIIRS vegetation index EDR accuracy requirement is 70%. But, usually, above 80% accuracy can be achieved by using neural networks or decision tree algorithms. When we did an experiment with a 20% land cover classification error, the LST retrieval process is a little bit worse, but it can still meet the threshold of 0.5 K for most temperature ranges. This is because land cover classifications by using neural networks or decision trees misclassify to a similar surface type that still has similar characteristics. For instance, broadleaf forests may be misclassifying as pine forests, pine brush as broadleaf brush, or wet soil as scrub soil. Grass, however, cannot be classified as rock or sand. So this is why an algorithm based on surface types may not cause great errors, even with a 20% land cover classification error.

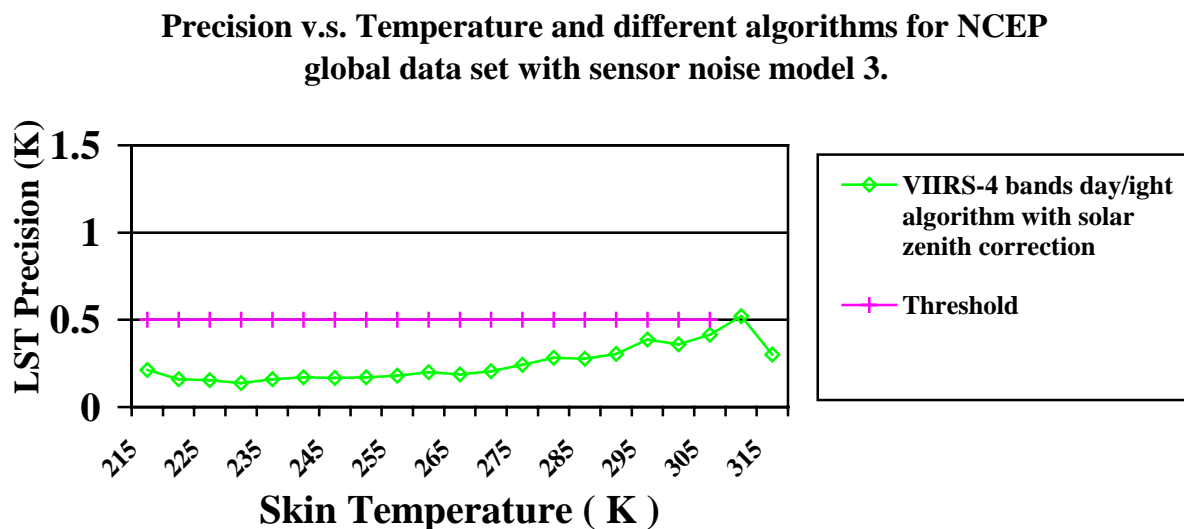


Figure 58. LST precision vs. temperature by using VIIRS –4 bands day/night algorithm with 20% land cover classification error.

3.5 PRACTICAL CONSIDERATIONS

3.5.1 Numerical Computation Consideration

In order to stay current, an average processing of 10,000 pixels per second must be performed. Specific aspects of the implementation include calculation of the blackbody temperature. A database from accurate radiative transfer simulations needs to be established, and a look-up table and interpolation scheme should be developed to speed the process. The physical retrieval must run a radiative transfer model. Current computers may only process a few pixels per second. Therefore, the implementation of the physical retrieval will depend on the speed of the computers used.

3.5.2 Programming and Procedural Considerations

Look-up tables will be used to increase the computational efficiency. Registration and re-sampling into horizontal cell size will be made after the level-2 LST processing. Parallel processing is allowed for the LST retrieval.

All procedures will be automatic.

3.5.3 Configuration of Retrievals

An LST retrieval configuration is used to establish the numerical values of adjustable parameters that are used in the retrievals, eliminating the need to hard-wire specific values into the software.

3.5.4 Quality Assessment and Diagnostics

A number of parameters and indicators will be reported in the LST product as retrieval diagnostics. LST maps and statistical information will be reviewed for quality assessment.

Quality flags that indicate the confidence in LST processing will be provided. They will be determined by comparing LST values from different algorithms (e.g., regression and physical retrievals, or different regression methods).

3.5.5 Exception Handling

Cloud pixels identified by the cloud mask will be skipped. Pixels with bad data will also be skipped and flagged.

3.6 ALGORITHM VALIDATION

3.6.1 Pre-Launch Validation

The atmospheric correction algorithm will be derived pre-launch by radiative transfer modeling to simulate the VIIRS infrared channel measurements. Selected radiosondes from the operational network stations or field campaigns will be used in VIIRS simulations for the development of the atmospheric correction algorithm. Measurements from the portable radiometers and a TIR spectrometer will be used to characterize the surface temperature fields and validate the atmospheric correction algorithms. The assimilated meteorological fields provided by NCEP and ECMWF provide a valuable description of surface temperature over land. These fields will be used in conjunction with radiative transfer modeling to simulate the VIIRS measurements, validate the radiosonde data, and provide direct input to the radiative transfer modeling process.

Measurements from AVHRR, the Along Track Scanning Radiometer (ATSR), and MODIS will be used in the pre-launch phase to study the error characteristics of the LST retrieval.

3.6.2 Post-Launch Validation

The infrared channels of VIIRS are calibrated by using measurements of cold space and on-board blackbody targets, producing radiance in the spectral intervals defined by the system response functions of each channel. This calibrated radiance can be converted to brightness temperatures at TOA. To derive LST from the calibrated radiance at satellite level, it is necessary to correct for the effects of the intervening atmosphere.

The post-launch validation activities are designed primarily to test the LST retrieval algorithm. Several fundamentally different data sets are needed to provide an adequate sampling of the atmospheric conditions and LST to validate the VIIRS IR radiance and retrieved LST fields. Highly focused field experiments are necessary to understand the atmospheric processes that limit the accuracy of the retrieved LST. Sites will be selected globally to validate VIIRS LST retrieval. (MODIS LST ATBD, version 3.2). Relatively flat areas of highly unmixed surface type will yield the highest quality measurements for validation. Portable radiometers and a TIR spectrometer will be calibrated with the same blackbody radiation source. Long-term global data sets are necessary to provide a monitoring capability that would reveal calibration drift and the consequences of extreme atmospheric events. Validation is required over the lifetime of the NPOESS missions.

4.0 ASSUMPTIONS AND LIMITATIONS

A major limitation of the VIIRS LST retrieval is that it can only be done under clear sky conditions. The algorithm is based on this basic assumption.

5.0 REFERENCES

- Becker, F. (1987): The impact of spectral emissivity on the measurement of land surface temperature from a satellite. *Int. J. Remote Sens.* 11: 369-394.
- Becker, F., and Z. L. Li (1990). Toward a local split window method over land surface. *Int. J. Remote Sens.* 11, 369-393.
- Becker, F., and Li, Z. -L. (1995) Surface temperature and emissivity at various scales: definition, measurement and related problems. *Remote Sens. Rev.* 12:225-253.
- Berk, A., L. S. Bernstein, and D. C. Robertson (1987). MODTRAN: A moderate resolution model for LOWTRAN. Rep. GLTR-89-0122, Burlington, MA: Spectral Sciences, Inc.
- Camillo, P. J., 1991: "Using one- or two-layer models for evaporation estimation with remotely sensed data" in Land Surface Evaporation: Measurements and Parameterization, ed. T. J. Schmugge and J. C. Andre, New York: Springer-Verlag.
- Caselles, V., E. Valor, C. Coll, and E. Rubio (1997). Thermal band selection for the PRISM instrument 1. Analysis of emissivity-temperature separation algorithms. *J. Geophys. Res.*, 102, 11145-11164.
- Coll, C., and Caselles, V. (1997), A split-window algorithm for land surfaces temperature from Advanced Very High-Resolution Radiometer data: Validation and algorithm comparison. *J. Geophys. Res.* 102: 16,697-16,713.
- Coll, C., Caselles, V., Sobrino, J.A., and Valor, E. (1994), On the atmospheric dependence of the split-window equation for land surface temperature. *Int. J. remote Sens.* 15 (1): 105-122.
- Cornette, W. M., P. K. Acharya, D. C. Robertson, and G. P. Anderson (1994). Moderate spectral atmospheric radiance and transmittance code (MOSART). Rep. R-057-94(11-30), La Jolla, CA: Photon Research Associates, Inc.
- Crag, R., M. Sugita, and W. Brutsaert, 1995: Satellite-derived surface temperature with boundary layer temperatures and geostrophic winds to estimate surface energy fluxes, *J. Geophys. Res.*, vol. 100, no. D12, 25447-25451.
- Diak, G. R. and M. S. Whipple, 1993: Improvements to models and methods for evaluating the land-surface energy balance and effective roughness using radiosonde reports and satellite-measured skin temperature data, *Agricul. and Forest Meteorol.*, vol. 63, no. 3-4, 189-218.
- Dozier, J., and Z. Wan (1994). Development of practical multiband algorithm for estimating land surface temperature from EOS/MODIS data. *Adv. Space Res.*, 13, 81-90.
- Harris, A.R., and I.M. Mason (1992). An extension to the split-window technique giving improved atmospheric correction and total water vapor. Vol. 13, no. 5, 881-892.

- Jackson, R. D., R. J. Reginato, and S. B. Idso, 1977: Wheat Canopy temperature: a practical tool for evaluating water requirements, *Water Resour. Res.*, vol. 13, 651-656.
- Kimura, F. and A. P. Shimiru, 1994: Estimation of sensible and latent heat fluxes from soil surface temperature using a linear air land heat transfer model, *J. Appl. Meteorol.*, vol. 33, no. 4, 477-489.
- Kealy, P. S., and S. J. Hook (1993). Separating temperature and emissivity in thermal infrared multispectral scanner data: Implications for recovering land surface temperature. *IEEE Trans. Geosci. Remote Sens.*, 31, 1155-1164.
- Kneizys, F. X., E. P. Shettle, L. W. Abreu, J. H. Chetwynd, G. P. Anderson, W. O. Gallery, J. E. A. Selby, and S. A. Clough (1988). Users guide to LOWTRAN7. Rep. AFGL-TR-88-0177, Bedford, MA: Air Force Geophys. Lab.
- Konzemann, T., 1994. Radiation conditions on the Greenland ice sheet. *Zurcher Geographische Schriften. Geographical Institute ETH* 56, 124.
- Li, Z. L., and F. Becker (1993). Feasibility of land surface temperature and emissivity determination from AVHRR data. *Remote Sens. Environ.*, 43, 67-85.
- Mannstein, H. (1987). Surface energy budget, surface temperature and thermal inertia in Remote Sensing Applications. In *Meteorology and Climatology*, ed. R.A. Vaughan and D. Reidel. I, NATO ASI Ser. C: Math. Phys. Sci. Vol 201, pp. 391-410, Dordrecht Netherlands: A Reidel Publishing Co.
- Meehl, G. A., Influence of the land surface in the Asian summer monsoon: external conditions versus internal feedbacks, *J. Climate*, vol. 7, 1033-1049.
- Prata, A. J. (1993). Land surface temperature derived from the Advanced Very High Resolution Radiometer and the Along-Track Scanning Radiometer I. Theory. *J. Geophys. Res.*, 98, 16689-16702.
- Price, J. C. (1984), Land surface temperature measurements from the split window channels of the NOAA-7/AVHRR. *J. Geophys. Res.* 89: 7231-7237.
- Running, S. W., 1991: Computer simulation of regional evapotranspiration by integrating landscape biophysical attributes with satellite data, in *Land Surface Evaporation: Measurements and Parameterization*, ed. T. J. Schmugge and J. C. Andre, New York: Springer-Verlag.
- Running, S. W., C. Justice, V. Salomonson, D. Hall, J. Barker, Y. Kaufman, A. Strahler, A. Huete, J.-P. Muller, V. Vanderbilt, Z. Wan, and P. Teillet, 1994: Terrestrial remote sensing science and algorithms planned for EOS/MODIS, *Int. J. Remote Sens.*, vol. 15, no. 17, 3587-3620.

- Sellers, P.J., F.G. Hall, G. Asrar, D.E. Strebel, and R.E. Murphy (1998). The first ISLSEP Field, Experiment (FIFE). *Bull. Amer. Meteorol. Soc.*, Vol. 69, no. 1, 22-27, 1988.
- Schmugge, T. J. and F. Becker, 1991: "Remote sensing observations for the monitoring of land surface fluxes and water budgets," in *Land Surface Evaporation: Measurements and Parameterization*, ed. T. J. Schmugge and J. C. Andre, New York: Springer-Verlag.
- Vidal, R. C. and B. L. Blad, 1991: Atmospheric and emissivity correction of land surface temperature measured from satellite using ground measurements or satellite data, *Int. J. Remote Sens.*, vol. 12, no. 12, 2449-2460.
- Vining, R. C. and B. L. Blad, 1992: Estimation of sensible heat flux from remotely sensed canopy temperatures, *J. Geophys. Res.*, vol. 97, no. D17, 18951-18954.
- Wan, Z., and J. Dozier (1996). A generalized split-window algorithm for retrieving land-surface temperature from space. *IEEE Trans. Geosci. Remote Sens.*, 34, 892-905.
- Wan, Z., and W. Snyder (1996). MODIS Land-Surface temperature algorithm theoretical basis document. MODIS ATBD
- Watson, K. (1992). Two temperature method for measuring emissivity. *Remote Sens. Environ.*, 42, 117-121.
- Weng, F., and N. Grody (1998), Physical Retrieval of land surface temperature using the special sensor microwave imager. *J. Geophys. Res.*, 103: 8839-8848.
- Yu, Y. D. , A. Rothrock, and R. W. Lindsay, 1995: Accuracy of sea ice temperature derived from the advanced very high resolution radiometer, *J. Geophys. Res.*, vol. 100, no. C3, 4525-4532.
- Zhang, L., Lemeur, and J. P. Goutorbe, 1995: A one-layer resistance model for estimating regional evapotranspiration using remote sensing data, in *Agricul. and Forest Meteorol.*, vol. 77, 241-261.